Study of driftwood dynamics in rivers for hazard assessment

Hossein Ghaffarian Roohparvar

To cite this version:

Hossein Ghaffarian Roohparvar. Study of driftwood dynamics in rivers for hazard assessment. Fluids mechanics [physics.class-ph]. Université de Lyon, 2019. English. NNT : 2019LYSEI094 . tel-03012242

HAL Id: tel-03012242
https://theses.hal.science/tel-03012242

Submitted on 18 Nov 2020

N°d'ordre NNT : 2019LYSEI094

THESE de DOCTORAT DE L'UNIVERSITE DE LYON
opérée au sein de
INSA LYON

Ecole Doctorale N° 162
Mécanique, Énergétique, Génie civil et Acoustique

Discipline de doctorat :
Mécanique des fluides

Soutenue publiquement le 15/11/2019, par :
Hossein GHAFFARIAN ROOHPARVAR

Study of driftwood dynamics in rivers for hazard assessment

Dynamique du bois flottant dans les rivières pour l'estimation de l'aléa

---

Devant le jury composé de :

LENZI, Mario Aristide	Professeur	Univ. degli Studi di Padova	Rapporteur
RICKENMANN, Dieter	Senior scientist	Swiss Fed. Res. Inst. WSL	Rapporteur
BERGOUGNOUX, Laurence	Maitre de conférences	Aix Marseille Université	Examinatrice
DUCHESNE, Laurence	Ingénieur	CNR	Examinatrice
MATAS, Jean-Philippe	Professeur	Univ. Claude Bernard Lyon 1	Examinateur
RIVIERE, Nicolas	Professeur	INSA Lyon	Directeur de thèse
LOPEZ, Diego	Maitre de conférence	INSA Lyon	Co-directeur de thèse
PIEGAY, Hervé	Directeur de Recherche	CNRS	Co-directeur de thèse

Département FEDORA – INSA Lyon - Ecoles Doctorales – Quinquennal 2016-2020

SIGLE	ECOLE DOCTORALE	NOM ET COORDONNEES DU RESPONSABLE
CHIMIE	**CHIMIE DE LYON** **http://www.edchimie-lyon.fr** Sec. : Renée EL MELHEM Bât. Blaise PASCAL, 3e étage **secretariat@edchimie-lyon.fr** INSA : R. GOURDON	M. Stéphane DANIELE Institut de recherches sur la catalyse et l'environnement de Lyon IRCELYON-UMR 5256 Équipe CDFA 2 Avenue Albert EINSTEIN 69 626 Villeurbanne CEDEX **directeur@edchimie-lyon.fr**
E.E.A.	**ÉLECTRONIQUE, ÉLECTROTECHNIQUE, AUTOMATIQUE** **http://edeea.ec-lyon.fr** Sec. : M.C. HAVGOUDOUKIAN **ecole-doctorale.eea@ec-lyon.fr**	M. Gérard SCORLETTI École Centrale de Lyon 36 Avenue Guy DE COLLONGUE 69 134 Écully Tél : 04.72.18.60.97 Fax 04.78.43.37.17 **gerard.scorletti@ec-lyon.fr**
E2M2	**ÉVOLUTION, ÉCOSYSTÈME, MICROBIOLOGIE, MODÉLISATION** **http://e2m2.universite-lyon.fr** Sec. : Sylvie ROBERJOT Bât. Atrium, UCB Lyon 1 Tél : 04.72.44.83.62 INSA : H. CHARLES **secretariat.e2m2@univ-lyon1.fr**	M. Philippe NORMAND UMR 5557 Lab. d'Ecologie Microbienne Université Claude Bernard Lyon 1 Bâtiment Mendel 43, boulevard du 11 Novembre 1918 69 622 Villeurbanne CEDEX **philippe.normand@univ-lyon1.fr**
EDISS	**INTERDISCIPLINAIRE SCIENCES-SANTÉ** **http://www.ediss-lyon.fr** Sec. : Sylvie ROBERJOT Bât. Atrium, UCB Lyon 1 Tél : 04.72.44.83.62 INSA : M. LAGARDE **secretariat.ediss@univ-lyon1.fr**	Mme Emmanuelle CANET-SOULAS INSERM U1060, CarMeN lab, Univ. Lyon 1 Bâtiment IMBL 11 Avenue Jean CAPELLE INSA de Lyon 69 621 Villeurbanne Tél : 04.72.68.49.09 Fax : 04.72.68.49.16 **emmanuelle.canet@univ-lyon1.fr**
INFOMATHS	**INFORMATIQUE ET MATHÉMATIQUES** **http://edinfomaths.universite-lyon.fr** Sec. : Renée EL MELHEM Bât. Blaise PASCAL, 3e étage Tél : 04.72.43.80.46 **infomaths@univ-lyon1.fr**	M. Luca ZAMBONI Bât. Braconnier 43 Boulevard du 11 novembre 1918 69 622 Villeurbanne CEDEX Tél : 04.26.23.45.52 **zamboni@maths.univ-lyon1.fr**
Matériaux	**MATÉRIAUX DE LYON** **http://ed34.universite-lyon.fr** Sec. : Stéphanie CAUVIN Tél : 04.72.43.71.70 Bât. Direction **ed.materiaux@insa-lyon.fr**	M. Jean-Yves BUFFIÈRE INSA de Lyon MATEIS - Bât. Saint-Exupéry 7 Avenue Jean CAPELLE 69 621 Villeurbanne CEDEX Tél : 04.72.43.71.70 Fax : 04.72.43.85.28 **jean-yves.buffiere@insa-lyon.fr**
MEGA	**MÉCANIQUE, ÉNERGÉTIQUE, GÉNIE CIVIL, ACOUSTIQUE** **http://edmega.universite-lyon.fr** Sec. : Stéphanie CAUVIN Tél : 04.72.43.71.70 Bât. Direction **mega@insa-lyon.fr**	M. Jocelyn BONJOUR INSA de Lyon Laboratoire CETHIL Bâtiment Sadi-Carnot 9, rue de la Physique 69 621 Villeurbanne CEDEX **jocelyn.bonjour@insa-lyon.fr**
ScSo	**ScSo*** **http://ed483.univ-lyon2.fr** Sec. : Véronique GUICHARD INSA : J.Y. TOUSSAINT Tél : 04.78.69.72.76 **veronique.cervantes@univ-lyon2.fr**	M. Christian MONTES Université Lyon 2 86 Rue Pasteur 69 365 Lyon CEDEX 07 **christian.montes@univ-lyon2.fr**

*ScSo : Histoire, Géographie, Aménagement, Urbanisme, Archéologie, Science politique, Sociologie, Anthropologie

Acknowledgements

This work was performed within the framework and with the support of the EUR H2O'Lyon (ANR-17-EURE-0018), PEPS (RiskBof Project – 2016) and LABEX IMU (ANR-10-LABX-0088) of Université de Lyon, within the program "Investissements d'Avenir" (ANR-11-IDEX-0007) operated by the French National Research Agency (ANR).

This thesis would not have been possible without the inspiration and support of a number of wonderful individuals - my thanks and appreciation to all of them for being part of this journey and making this thesis possible. I owe my deepest gratitude to my supervisors Dr. Diego LOPEZ, Dr. Emmanuel MIGNOT, Prof. Hervé PIEGAY and Prof. Nicolas RIVIERE for inspiring my interest and for their guidance through each stage of the process. Without their enthusiasm, encouragement, support and continuous optimism this thesis would hardly have been completed.

I would also like to show my gratitude to Prof. Mario Aristide LENZI and Dr. Dieter RICKENMANN as the reviewers and Prof. Jean-Philippe MATAS, Dr. Laurence BERGOUGNOUX and Mme. Laurence DUCHESNE as the examiners of this thesis for their comments and sharing their insights with me.

I am forever thankful to my colleagues at the LMFA and EVS of Lyon for their friendship and support, and for creating a cordial working environment. I thankfully acknowledge the contributions of Dr. Bruce MACVICAR and Dr. Virginia RUIZ-VILLANUEVA, for their insight into addressing some problems discussed in this thesis. I would like to thank Prof. Eric BARTHELEMY and Prof. philippe BELLEUDY for organizing required resources and liaising with industry partners. I acknowledge the contributions from the LTHE of Lyon and TENEVIA Co. for providing field data on the River. I would like to show my appreciation to all our project partners for sharing their expertise and experiences, and for providing valuable feedback throughout this research.

Finally, my deep and sincere gratitude to my family for their continuous and unparalleled love, help and support. I am grateful to my wife ELNAZ for her unconditional love and support throughout my educational career. She supported me without any complaint or regret that enabled me to complete my Ph.D thesis. I am forever indebted to my parents JAVAD and TAHEREH for giving me the opportunities and experiences that have made me who I am. They selflessly encouraged me to explore new directions in life and seek my own destiny. My thesis acknowledgement would be incomplete without thanking my baby-son, SINA, whose smiling face always made me happy and inspired me. This journey would not have been possible if not for them, and I dedicate this milestone to them.

Abstract

Driftwood is an integral part of river corridors where it plays an important role both in river ecology and morphology. During the last decades, the amount of large wood transported in some of the European rivers has increased, notably due to modifications in the human pressure and management of riparian forest buffers along rivers. This causes an increase of potential hazards for hydraulic structures and urban areas. In this context, the aim of this thesis is to study the driftwood dynamics in rivers in order to provide elements for hazard assessment. This is carried out in two ways: (i) using in-situ streamside videography to measure the amount of wood transported by the river during floods and (ii) analyzing the dynamics of individual pieces of wood both on the field and in a well-controlled experimental environment combined with theoretical models. The present work provides several scientific and technical contributions. First by studying the link between wood discharge and flood characteristics, such as flood magnitude, hydrograph and inter-flood time, we consolidate and extend the present knowledge about the link between flow and wood discharges. Second, our studies show that when a piece of wood is recruited into the river, it is accelerated on a limited distance, which scales as the wood length in the flow direction. Once the wood piece reaches the flow velocity, it behaves as a flow tracer. In terms of technical contributions, by comparing the video monitoring technique in two different sites, we provide some recommendations that are useful for practitioners for installing new monitoring stations. This work will be part of the driftwood hazard and risk assessments, for which accurate wood dynamics quantities are required.

Résumé

Le bois flottant fait partie intégrante des systèmes fluviaux et joue un rôle important dans l'écologie et la morphologie des rivières. Au cours des dernières décennies, la quantité de bois transportée dans certaines rivières d'Europe a augmenté, notamment en raison de modifications de l'occupation et de la gestion des zones boisées le long des rivières, entraînant une augmentation des aléas pour les ouvrages hydrauliques et les zones urbaines. Dans ce contexte, l'objectif de cette thèse est d'étudier la dynamique du bois flottant dans les rivières afin de fournir des éléments pour l'estimation des risques. Cela a été effectué de deux manières: (i) en utilisant la vidéographie in situ au bord d'un cours d'eau pour mesurer la quantité de bois transporté lors d'une crue et (ii) en analysant la dynamique de morceaux de bois isolés, à la fois sur le terrain et par une étude expérimentale de laboratoire complétée par des modèles théoriques. Ce travail présente plusieurs contributions scientifiques et techniques. Tout d'abord, en étudiant le lien entre le débit de bois et les caractéristiques de crue, telles que son amplitude, son hydrogramme et le délai entre deux crues, nous renforçons et élargissons les connaissances actuelles sur le lien entre les débits de crue et de bois. Ensuite, nos études montrent que lorsqu'un tronc est pris dans la rivière, il est accéléré sur une distance limitée, d'ordre de grandeur donné par la longueur du bois dans la direction de l'écoulement. Une fois la vitesse d'écoulement atteinte, le bois se comporte comme un traceur de l'écoulement. En termes de contributions techniques, se basant sur deux sites différents, nous fournissons des recommandations utiles aux praticiens pour l'installation de nouvelles stations de surveillance. Ces travaux s'intègrent dans le cadre de l'évaluation des aléas et des risques liés au bois flottant, pour lesquelles des quantités précises de la dynamique du bois sont nécessaires.

Contents

List of Figures

List of Tables

Index of notations

Dimensionless parameters

Symbol	Description	unit
$\star$	Normalization based on flow length scale (L_0)	[-]
$\sim$	Normalization based on object response distance (λ)	[-]
C_A	Added mass coefficient	[-]
C_D	Drag coefficient	[-]
C_L	Lift coefficient	[-]
Fr_f	Flow Froude number	[-]
Fr_p	Particle Froude number	[-]
N_D	Number of consecutive frames for detecting a single object	[-]
Re_f	Flow Reynolds number	[-]
Re_p	Particulate Reynolds number	[-]
St	Stokes number	[-]

Dimensional parameters

Greek

Symbol	Description	unit
δt	Uncertainty on the time	[s]
δl	Uncertainty on the distance	[m]
δv	Uncertainty on the velocity	[m.s^{-1}]
δa	Uncertainty on the acceleration	[m.s^{-2}]
Δt	Time interval	[s]
Δl	Distance interval	[m]
θ_0	Initial orientation	[degree]
λ	Particle characteristic response distance	[m]
λ_{trunk}	Particle characteristic response distance for logs without root	[m]
ρ_f	Fluid density	[kg.m^{-3}]
ρ_p	Particle density	[kg.m^{-3}]

Latin

Symbol	Description	unit
d_y	Distance between trajectory and corresponding streamline	[m]
D	Object diameter	[m]
$\frac{D}{Dt}$	Convective derivative	[s^{-1}]
F	Wood fluxes	[number.s^{-1}]
F_D	Drag force	[N]
F_L	Lift force	[N]
i	Horizontal direction on a figure	[pixel]
j	Vertical direction on a figure	[pixel]
L	Object length	[m]
L_0	Flow length scale	[m]
L_{50}	Length so that 50% of objects are smaller	[m]
L_{75}	Length so that 75% of objects are smaller	[m]
L_{99}	Length so that 99% of objects are smaller	[m]
L_R	Length of roots	[m]
L_x	Object dimension in flow direction	[m]
m	Object mass	[kg]
m m_f	Displaced fluid mass	[kg]
m_p	Particle mass	[kg]
N_{BP}	Number of blurry pixels	[pixel]
Q_{10}	10 years return period flood	[$m^3.s^{-1}$]
Q_{bf}	Bankfull discharge	[$m^3.s^{-1}$]
Q_f	Flow discharge	[$m^3.s^{-1}$]
Q_{max}	Maximum flood discharge	[$m^3.s^{-1}$]
Q_w	Wood discharge	[$m^3.s^{-1}$]
S	Particle submerged frontal area	[m^2]
S_{root}	Root frontal area	[m^2]

S_{trunk}	Simple log frontal area	[m^2]
t	Time	[s]
T_0	Flow time scale	[s]
T_p	Object viscous response time	[s]
U_0	Flow surface velocity	[m.s^{-1}]
$\mathbf{u}$	Flow velocity vector	[m.s^{-1}]
$\mathbf{v}$	Particle velocity vector	[m.s^{-1}]
v	Streamwise particle velocity	[m.s^{-1}]
v_0	Initial streamwise particle velocity	[m.s^{-1}]
V	Particle volume	[m^3]
V_f	Displaced fluid volume	[m^3]
X	Streamwise direction	[m]
y_0	Initial lateral distance from obstacle centerline	[m]
y_c	Critical lateral distance from obstacle centerline	[m]
y_{max}	Ultimate lateral distance from obstacle centerline for impact	[m]
Y	Lateral direction	[m]
Z	Vertical direction	[m]

Chapter I

Introduction

I.1 Context

In the natural cycle, rivers play an important role in natural biodiversity, material conveyance, and morphodynamics of the earth. Transportation is one of these roles that can be done either actively, like sailing activities or fish migration, or passively like transportation of sediments, waste and plastic patches or pieces of wood. Among different materials that are transported by a river, the motion of large pieces of wood LW in a river is important in term of carbon content or hydraulic of the flow due to their size compare to the river width and flow depth. Large pieces of wood can modify the river characteristics both ecologically and morphologically, which is a beneficial factor in context of natural cycle.

During recent decades human has significantly intervenes in the natural cycle, in limited scales like morphological changes (*e.g.* extension or contraction of river cross-section, embankment of river walls, modifying the slope of the river or construction inside or along the river), in global scale throughout the planet like climate change that exacerbates natural disasters such as heavy rainfall and high return period floods, or sometimes also regionally with deforestation or even afforestation, such as in European regions with progressive depopulation and rural abandonment These human activities, change the natural patterns in rivers and increase the points where large wood pieces negatively affect the surrounding environment precisely in urban environment with a high degree of morphological changes.

These changes have lead to large wood being considered as a potential hazard in rivers and many efforts have been made to study the effects of presence of large pieces of wood in rivers. In this context, the aim of this thesis is to quantify the potential hazards related to the large wood pieces in two ways: by measuring the amount of wood pieces in a river and by analyzing the dynamics of each individual piece of wood on the field and in a well controlled experimental environment.

I.2 Wood in rivers

I.2.1 The benefits of wood

Instream wood (also called driftwood) is an integral part of river corridors where it plays an important role in both river ecology and morphology (Montgomery *et al.*, 2003).

Instream wood enhances the biodiversity along the river because of its effects on habitat diversification and its contribution to the food web (Wohl & Scott, 2017). Wood is stored within the floodplain, sometimes for decades or centuries, which increases the residence time of organic carbon (Gonor *et al.*, 1988; Everett & Ruiz, 1993; Naiman *et al.*, 2002; Gregory *et al.*, 2003; Gurnell *et al.*, 2005; Battin *et al.*, 2008; Skalak & Pizzuto, 2010).

Wood also has direct effects on the river's morphology by increasing the flow resistance and by reducing sediment transport capacity. Wood can affect cross-sectional area and water slope, by increasing the range of grain size patches. It can also change the forces on river banks, sometimes resulting in increased rates of bank retreat and floodplain morphology modifications (Wohl, 2013; Rickenmann, 2012). Therefore, protecting and re-introducing wood into the river can be used as a restoration technique on rivers both ecologically (Wohl & Scott, 2017) and morphologically (Piton & Recking, 2015).

I.2.2 Potential hazard associated with large pieces of wood in rivers

During the base-flow normally there is almost no wood in movement in the river. Wood discharge increases significantly during flood events (MacVicar & Piégay, 2012; Kramer & Wohl, 2014). In a flood, the stored wood in river and in the riparian area is recruited to the river and is transferred into the mainstream and downstream with the flow (Ruiz-Villanueva *et al.*, 2013). Additional green wood pieces are introduced within the river through active physical processes such as bank erosion or mass-wasting and landsliding (Keller & Swanson, 1979; Benda *et al.*, 2003).

Floating pieces of wood, notably large trunks, can be responsible for damaging hydraulic structures and increasing flood risks due to wood accumulation around bridge piers (Bocchiola *et al.*, 2008; Cicco *et al.*, 2018). Wood around bridge piers, leads to the creation of natural obstacle that reduces the conveyance of the mainstream, which can result in more frequent and severe overbank flows or scouring along the river (Abbe & Montgomery, 1996) or near the bridge piers (Lagasse, 2010). Flood events in 1987 and 2005 in Switzerland or in 1997 in Venero Claro (Central Spain) are well known examples that caused significant economic losses (Rickenmann & Zimmermann, 1993; Ruiz-Villanueva *et al.*, 2013; Schmocker & Hager, 2011). Figures I.1(a),(b) show two examples of the wood accumulation around bridge piers during these two floods.

The risk associated to driftwood can be discussed more specifically in urban areas. The increase of the flood hazard described above is associated there with a high degree of vulnerability due to the presence of infrastructures, networks and people. Increasing wood pieces number and size is expected to increase hazard and, for a given urban environment, risk.

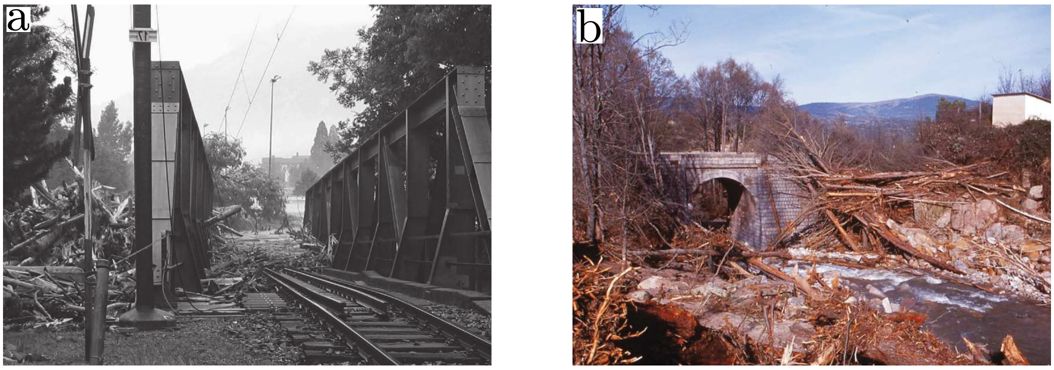

Figure I.1: Wood accumulations near a bridge (a) in Sarnen, Switzerland, during 2005 flood (Schmocker & Hager, 2011) and (b) in Venero Claro, Spain during 1997 flood (Ruiz-Villanueva *et al.*, 2013) both caused significant economic losses.

To assess the potential costs due to logjam in river Lassettre & Kondolf (2012) compared three scenarios, by comparing the ratio between piece length and the width of infrastructure (bridges and culverts), for Soquel Creek, in California, USA; (i) historical (current culvert sizes and partial-spanning bridges), (ii) current (current culvert sizes and full-spanning bridges) and (iii) LW-passing approach whereby infrastructure is enlarged to accommodate LW passage downstream. They show that over longer time periods (more than 50 years), the savings and potential benefits of the LW-passing approach increases. Therefore, passing large woods can decrease the risks in a vulnerable area like the urban environment by decreasing the potential hazard due to logjam.

In continue, to better understand the risks associated with wood transport and deposition in streams Ruiz-Villanueva *et al.* (2014*b*) applied a scenario-based flood model coupled with wood budget to simulate wood transport and deposition in the eastern massif of the Sierra de Gredos, Spain, as a vulnerable area. They identify the main infrastructures sensitive to the passing of large wood and simulate the consequences of their blockage due to wood. This work shows that wood transport and deposition during flooding may increase potential damage at critical stream configurations (bridges) by up to 50% and the number of potentially exposed people nearby these areas by up to 35% (Ruiz-Villanueva *et al.*, 2014*b*).

Based on the mentioned studies, logjam near instream infrastructure (bridges and culverts) is a potential hazard. in this context Schalko (2017); Schalko *et al.* (2019) showed the concurrent effect of flow, bridge and wood characteristics on the bridge clogging. Regarding the bridge and flow characteristics, De Cicco *et al.* (2015, 2016) showed that the shape of a bridge pier and the flow froude number can change the probability of impact. Moreover, about the bridges without pier, Schmocker & Hager (2010, 2011); Schmocker & Weitbrecht (2013) studied the effect of free board, flow Froude number and the bridge shape on bridge clogging. However, there is the remaining question one step before logjam, about the parameters driving impact between wood and bridge pier.

Therefore, different researches show that different parameters such as river morphology (Gurnell *et al.*, 2002), flow characteristics Lyn *et al.* (2003), bridge characteristics (De Cicco *et al.*, 2015, 2016; Gschnitzer *et al.*, 2017) and wood geometry (Schmocker & Hager, 2010; Comiti *et al.*, 2008) can control wood interaction with instream hydraulic structures, exacerbate wood accumulation and increase the potential hazards related to LW in rivers. These studies have crucial role on predicting possible hazards and reducing the maintenance cost of instream hydraulic structures and other infrastructure near a river.

I.3 Wood fluxes

As mentioned, during recent decades LW in rivers is considered as a potential hazard. This potential hazard strongly depends on the amount of wood within a river and on whether a large volume of the wood remains stationary or becomes mobile during floods (Wohl *et al.*, 2016). Therefore, to be able to quantify the hazards associated with LW, it is necessary to quantify the amount of wood pieces in rivers. In this section after introducing some fundamental definitions used in our work and the parameters driving wood in rivers, different strategies to monitor the amount of wood in a river are considered and finally the link between flood discharge and the amount of instream wood is discussed.

I.3.1 Definitions

In this part, some fundamental definitions are introduced in order to follow the same concepts throughout the thesis.

The first fundamental issue about pieces of wood in riverine environments is to define a criterion to distinguish large woods (LW) from coarse woods (CW). One of the widely used criterion among the literature is selecting a truncation length or a truncation diameter. For example the range of 0.3 m to 5 m has been used as truncation length, and the truncation diameter between 5 cm to 30 cm has been used in different studies (Comiti *et al.*, 2006; R.A. *et al.*, 2004). However, as a global criterion, in most of studies, the minimum diameter of 5 cm and minimum length of 1 m have been used to define large wood (Wohl *et al.*, 2010). Here to follow this global criterion, 1 m truncation length is used as it is consistent with other similar works (MacVicar *et al.*, 2009; MacVicar & Piégay, 2012) and it fits well with our equipment.

The other key parameters are wood flux and wood discharge that are used to quantify the amount of instream wood. Wood flux F, (also known as wood frequency) is the number of wood pieces that are transported through a given cross-section per unit time. Wood discharge Q_w, defined similarly as water discharge, is the volume of transported wood per unit time. Both these terms are identified in high temporal resolution (*e.g.* 1 day, 1 hour, 1 minute or 1 second). The contrast between wood flux and discharge is that for wood flux only the number of wood pieces are taken into account while, for

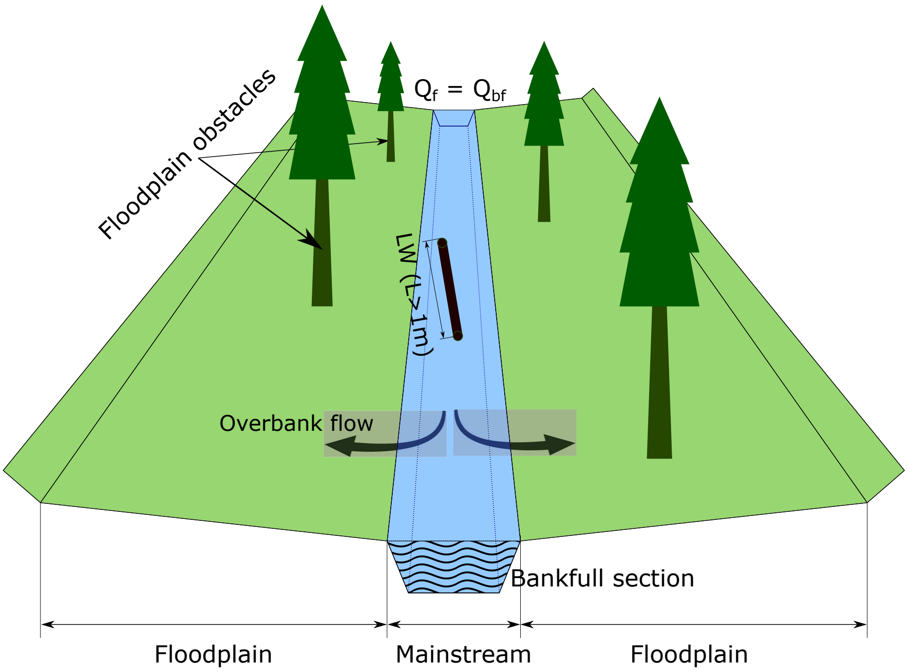

Figure I.2: Schematic view of some definitions used in this study.

Table I.1: Units used for different definitions

Definition	LW	F	Q_w	Q_{bf}
unit	m (>1m)	number/s	m^3/s	m^3/s

wood discharge the volume of wood pieces have to be measured and for volume the piece size is required. Therefore based on wood discharge it is possible to say if the size of wood pieces are typically large or small.

Bankfull discharge Q_{bf} is an important morphological parameter and is characterized as the flow discharge when the river is just about to spill onto its floodplain. The general range of one to two years flood events approximate bankfull discharge (Castro & Jackson, 2001; Dury *et al.*, 1963; Leopold, 1994; Hickin, 1968; Dunne & Leopold, 1978; Williams, 1978; Kramer & Wohl, 2014). Castro & Jackson (2001) show that 1.5 year return period flood would be a good approximation for bankfull discharge.

The other morphological parameter that has a significant role on wood motion in a river is the presence of obstacles in the floodplain which can be considered as a roughness element on wood motion. Wohl & AG (2018); Pickett & White (1985) describe this roughness element as the floodplain disturbance. For example standing trees along the floodplain are the factors that disrupt wood movement.

Figure I.2 shows schematically these definitions. In this figure flow discharge Q_f is at Q_{bf}, the bankfull section is totally full. Thus, by increasing the flow discharge overbank flooding starts and river flows into the floodplain. At this stage, when $Q_f > Q_{bf}$ the standing trees are considered as obstacles that disturb the motion of wood in floodplain. Table I.1 shows the units used for some of the definitions described here.

I.3.2 Parameters driving instream wood

Wood is recruited into rivers by different processes, such as bank erosion, mass wasting, decay, collapse of trees due to ice loading, episodic forest growth and death, chronic mortality and stream transport (Keller & Swanson, 1979; Benda *et al.*, 2003). These processes are highly affected by the region where wood is recruited to the stream. This means that on the upland with confined channels, along the midlands in piedmont rivers and in lowlands and coastal basins, different processes have the leading role in wood recruitment processes (Gurnell, 2013; Wohl & Scott, 2017).

On the upland rivers, where the river is draining steep hill-slopes, in more than 50%, the source of recruitment is slope instability (May & Gresswell, 2003; Rickli *et al.*, 2018). However, individual tree mortality, mass movements, and avalanches also play a role in low-order, confined rivers (Wohl *et al.*, 2019). Along the midlands, in piedmont rivers, the dominant recruitment process from the local riparian area are bank erosion (Lassettre *et al.*, 2008; Bertoldi *et al.*, 2013; Piégay *et al.*, 2017) and wind-throw (May & Gresswell, 2003). In lowlands and coastal basins, low volumes of large woods are consistent with the relatively young riparian stands and wood recruitment, and distribution are dominated by local factors such as individual tree mortality, coupled with local bank failure (Magilligan *et al.*, 2008; Golladay *et al.*, 2007; Piégay *et al.*, 2017) with high residence times up to 240 years (Webb & Erskine, 2003). Rickli *et al.* (2018) show a correlation between mean channel width, catchment area and instream wood in mountain streams. In any cases, especially at piedmont rivers, overbank flow in floodplain and bank erosion play a significant role in the recruitment of the wood.

While lateral outputs to the floodplain can only occur when flood levels are sufficiently high, lateral inputs include terms that are not only dependent on discharge, such as toppling from ice, wind and fire, but sufficient water depth is needed to mobilize instream wood and transport it through a reach (Braudrick & Grant, 2001; Bocchiola *et al.*, 2006). These lateral inputs from the riparian zone into the river can facilitate formation of channel-spanning logjams that limit subsequent wood transport (Oswald & Wohl, 2008). These channel-spanning logjams can create higher wood loads than single dispersed pieces, and spatial density of the logjams regulates the efficiency of a reach at trapping wood in transport (Scott & Wohl, 2018). In this process, presence of leaf on new recruited green trees can exacerbate flow resistance near these logjams (Jalonen & Järvelä, 2013, 2014). By comparing different plant species, Västilä & Järvelä (2014) show that the foliated twigs drag is strongly governed by the ratio between leaf and stem area. However, due to low sampling densities, a limited range of discharge, and a lack of verification data to check wood transport estimates, information on the wood flux during overbank floods is limited and the link between water discharge and the fluvial transport of the wood remains poorly understood (MacVicar & Piégay, 2012).

I.3.3 Existing techniques to quantify wood fluxes

Monitoring wood is challenging due to difficulties such as accessibility to site, connectivity to remote devices and financial limitations. In many cases, especially during large floods, access to the river is too laborious or dangerous for both operators and equipment. In such cases tagging, or repeat surveys, are impossible or ineffective (Lyn *et al.*, 2003; Moulin & Piegay, 2004; Muste *et al.*, 2008). In remote sensing techniques, the connectivity is quite important. However, there are often data gaps when equipment is not working or not installed correctly (Carbonneau & Piégay, 2012). The financial limits are another problem in many cases. For different equipments trade-off is necessary between quality of acquired data, speed of data transmission, required storage, and cost (Carbonneau & Piégay, 2012).

Consequently, quantifying wood fluxes is a research topic that has been explored in different ways based on the needed data and practical limitations. Different strategies for monitoring wood along a river highlight variety of temporal and spatial resolutions at different scales. Therefore, in this section after talking about study of wood at different temporal and spatial scales, some of the methods to quantify the amount of wood in a river are presented.

I.3.3.1 Temporal and spatial scales to quantify wood fluxes

The presence of wood in riverine environment can be studied at different spatial scales using different monitoring techniques. Therefore, it is important to know different scales for studying the amount of wood and the function of wood at different scales. A single piece of large wood in a large channel, for example, will likely have only local effects, whereas a large jam that spans a channel can influence processes and forms along an entire stream reach (Gurnell *et al.*, 2002; Wohl, 2011). Therefore, the effects of variation of pieces of wood along a river can be studied at large spatial scale ($10^3 - 10^5$ m), known as the segment scale (Fausch *et al.*, 2002), at medium spatial scale ($10^1 - 10^3$ m) known as the reach scale and at low spatial scale ($10^0 - 10^1$ m) known as the river unit scale (Wohl *et al.*, 2016).

At large spatial scale *i.e.* the segment scale, the effects of the wood strongly depend on valley geometry and location within a drainage basin. In confined, steep headwater valleys, large wood primarily affects river processes and forms. In lowland rivers with floodplains, large wood within river also affects floodplain processes and forms. At medium spatial scale along the stream lengths of tens to thousands of meters, large wood can strongly influence river plan-form and morphology (Wohl *et al.*, 2016). At low spatial in stream lengths of a meter to tens of meters, individual pieces of the wood or logjams create overhead cover, velocity refuges, and visual isolation, all of which are important to fish (Fausch, 1993) and invertebrates (Wohl *et al.*, 2016).

Often, there is a trade-off between the temporal and spatial resolution for measuring the amount of wood fluxes at different scales. Therefore, it is important to know which kind of data are needed, to find the best way for sampling. For example studying long term variation of wood pieces along a river should be monitored in large spatial and temporal scale while, monitoring the biodiversity of micro habitats is done in a short spatial and temporal scale. There are different strategies for monitoring wood along river reaches, such as tagging, ground or aerial photography, multi-spectral and hyper-spectral imaging, Lidar and video-monitoring (Carbonneau & Piégay, 2012). Each of these strategies are powerful to detect some characteristics of wood in river in a certain temporal resolution. In the following, by categorizing these strategies in low and high temporal resolution, we introduce briefly each of these strategies to see which ones are compatible with our goals, *i.e.* quantifying the wood in river during a flood event.

I.3.3.2 Quantifying wood fluxes in low temporal resolution

Among different strategies to monitor the wood fluxes and discharge in river, most of them can monitor the instream wood with a low temporal resolution (*e.g.* 1 month, 1 year or 1 decade). In the field, there are many different parameters both in rivers (Turowski *et al.*, 2013) and reservoirs (Seo *et al.*, 2008; Ruiz-Villanueva *et al.*, 2014*c*) that can be quantified in order to clarify the consequences of the presence of wood in river *e.g.* density, dimensions, age, and so on. Wohl *et al.* (2010) summarize and define the most important features to be considered. Here some of the most commonly used methods are introduced.

Tagging is a technique for tracking the movement of wood pieces along river reaches to understand the dynamics of erosion and wood transport. Tagging technique includes painting preassigned colors at each class (Lenzi, 2004), inserting traceable plastic or metal plates (Warren & Kraft, 2008) passive or active radio frequency identification (RFID) (MacVicar *et al.*, 2009) or GPS devices (Ravazzolo *et al.*, 2013) into the wood. Comparison between active and passive RFIDs and GPS trackers show that passive RFID tags can be only detected at close distances from the operator (0.30 m) but they are reliable in long time uses (more than 5 years), active RFID tags are more convenient in larger range of detection by a portable antenna (10 to 300 m) and therefore, are more effective to recover the woods after floods and in inaccessible places but with a shorter life (less than 4 years). GPS trackers are costly but can identify the instantaneous trajectory of the wood pieces in order to calculate their trajectory as well as their velocity during a flood event (MacVicar *et al.*, 2009; Ravazzolo *et al.*, 2013). According to the number of wood pieces that are tagged, always finite number of wood pieces can be monitored in these methods. After the pieces of wood are tagged by RFID, they are tracked after a big flood. Therefore the time and spatial resolution are limited to two points, start and end of motion. But the trajectory of wood pieces can cover a long distance. The positive point of GPS is, when a piece of wood is tagged by GPS it can be tracked in high time and spatial resolution and at large spatial scale along the river.

Thanks to new platforms such as kites, microlights, drones and satellites which are becoming widely used in riverine sciences (Lejot *et al.*, 2007), remote sensing, using aerial techniques is also widely used to monitor amount of wood along the rivers. These techniques are especially effective for remote areas where access, travel costs or project costs are limited (Carbonneau & Piégay, 2012). Both multispectral and hyperspectral cameras mounted on an airborne device are widely used on rivers. The main difference between multispectral and hyperspectral is the number of bands and how narrow the bands are. Wood has a clear spectral signal and is distinguishable even with a fraction of a pixel of a spectral image (Marcus *et al.*, 2003). Therefore, airborne and space-borne multispectral and hyperspectral imaging systems are useful to evaluate spatial and temporal distribution of woods at network scale (Marcus *et al.*, 2002) as well as detecting individual pieces of wood and piles of large woods along the river (Leckie *et al.*, 2005). Light detection and ranging (Lidar), mounted on an airborne device or in terrestrial form, also have been widely used to detect large woods and logjam as well as to provide information about wood characteristics along the river, such as orientation and shape (Fleece, 2002; Boivin & Buffin-Bélanger, 2010). These aerial and terrestrial platforms are usable up to a few times a day. Therefore, their time resolution is in hour to days or even more. Depend on using terrestrial or aerial platforms and also depend on the characteristic of the aerial platform *i.e.* at high elevation like satellite or at low elevation like a drone their spatial scale is different. Additionally the amount of monitored wood fluxes is highly depend on the elevation of monitoring and the spatial scale that the camera is covered.

I.3.3.3 Quantifying wood fluxes in high temporal resolution

Among studies on wood mobility usually expressed in meters per year or per flood events, works are also done on wood discharge, then expressed in m^3 per second or per hour. Videography is a technique that can be used to present data per second or per hour. Streamside videography refers to the capture of a series of images. It provides high temporal-resolution data useful for computing rates of transport and fine-scale relationships between wood and water discharges using a camera which is located at a safe position from the flood on a river bank. Lyn *et al.* (2003) used ground cameras to study wood delivery to a deflector upstream from a bridge pier that was sensitive to wood trapping in order to assess its efficiency. MacVicar *et al.* (2009); MacVicar & Piégay (2012) use a stream-side video camera to detect wood passage and to measure wood discharge in the Ain River (France) over three floods within 1 to 2 year return period. They show the feasibility of this technique to measure wood discharge, velocity, length distribution and orientation of the woods as well as the link between wood and water discharge. Because camera is located in a fixed position with permanent connection, and data are recorded continuously, videography technique can monitor unlimited amount of wood during unlimited time. A fixed camera covers a limited spatial scale. But using a high resolution camera data can be acquired with high spatial and temporal resolution.

Measuring the transport of the wood using video cameras has significant advantages. The wood is easily visible by the camera on river surface due to the buoyancy. The recording of images is continuous, so it is possible to record the trajectory of wood. Video installations can be placed where they are most useful for wood transport calculations, such as the beginning and end of a reach where they can monitor the input and output

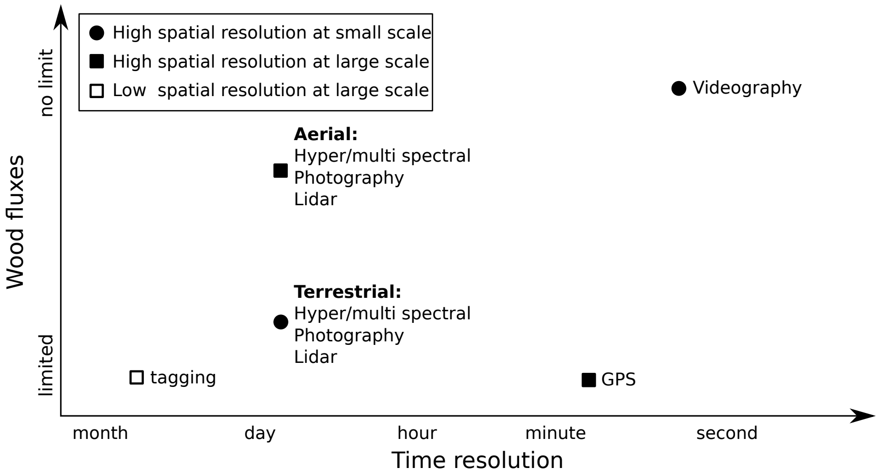

Figure I.3: Efficiency of different monitoring techniques to monitor wood fluxes in a river.

of floating wood. Camera can be connected to network and images are transmitted to a central location for storage and analysis. Measurements are possible during floods. Digital cameras are relatively inexpensive, and their proliferation has driven down both the cost of video monitoring systems and of the technical expertise required for their installation and operation (Muste *et al.*, 2008; MacVicar *et al.*, 2009; Carbonneau & Piégay, 2012). However lack of contrast between flow and floats, due to the lack of illumination, reduces the detectability of the wood in a river. This is mostly due to weather condition such as cloudiness, fog, rain and snow which can reduce the visibility of the surface. Therefore, detecting wood automatically by this approach is a difficult task. However, recently there are some efforts to detect the floating pieces of wood in rivers (Ali & Tougne, 2009; Ali *et al.*, 2011, 2012, 2014). But the results are not applicable in different rivers.

Figure I.3 summarizes different monitoring techniques based on the amount of wood each method can monitor and the typical time resolution in each method. Additionally the spatial resolution and spatial scale that each method is applicable is presented by the markers. Note that the difference between fixed streamside videography with other terrestrial techniques is that normally in different terrestrial techniques, the devise is fixed on the terrain temporarily while in fixed streamside videography technique as the camera is not so expensive, it is possible to use camera permanently. Therefore, using the fixed streamside videography technique it is possible to monitor unlimited amount of wood with high time resolution.

I.3.4 Wood discharge during a flood

Flood discharge plays a significant role on bank erosion, mass wasting events such as landslides and debris flows, and extraction of buried wood (MacVicar & Piégay, 2012).

Wood discharge increases significantly during flood events, and many studies show that, during a flood, Q_{bf} plays a crucial role on the relation between wood fluxes and flood discharge (Wohl *et al.*, 2018; Oswald & Wohl, 2008; Wohl *et al.*, 2019; MacVicar & Piégay, 2012; Ruiz-Villanueva *et al.*, 2016).

For the discharges less than Q_{bf}, increasing flow discharge increases the water depth, the wet area and the mean velocity of the channel. MacVicar & Piégay (2012) show that increasing water level causes the volume of floating wood increase and river banks are progressively inundated. At this stage, bank erosion is minimal and it is expected that the majority of the wood results from the mobilization of storage within river, where wood is available on the bars due to deposition during the previous flood and tree mortality in the inter-flood period.

While for debris flows and coarse wood pieces there is a direct relation between Q_f and float discharge (Lenzi *et al.*, 2011; Turowski *et al.*, 2013), for large wood pieces by exceeding flood discharge from Q_{bf}, wood can flow through the floodplain. This results in a nonlinearity on mobilization and storage of the wood fluxes (Wohl *et al.*, 2018; Oswald & Wohl, 2008; Wohl *et al.*, 2019). Ruiz-Villanueva *et al.* (2016) show that the ratio between wood pieces transported downstream the studied reach and total inlet logs increases with discharge until it reaches an upper threshold equal to bankfull discharge, and then decreases or increases much more slowly. This stage of wood motion is important because storage and blockage are more likely during the movement of numerous wood pieces together, named as congested motion of wood (Braudrick *et al.*, 1997; Ruiz-Villanueva *et al.*, 2019). When sufficient pieces of wood are moving simultaneously, individual pieces interfere with the transport of adjacent pieces (Wohl, 2013).

Wohl *et al.* (2018) show that floodplain obstacles referred as river disturbance intensifies the wood storage from the river towards the floodplain, resulting in longitudinal nonuniformity of the wood distribution. Figure I.4 is an example of the effect of obstacles due to the presence of standing trees on the floodplain jams. In this figure it is seen that by increasing flood discharge into the floodplain in the high-magnitude disturbance sites, the distribution of floodplain wood jams corresponds to the presence of standing trees on the floodplain. High quantities of wood pieces in the floodplain can be buried in alluvial deposits and so are available for remobilization by bank erosion and lateral migration of river channels during the next floods (Nanson *et al.*, 1995; Brooks & Brierley, 2002). The effect of standing trees in floodplain has been also studied experimentally by Bocchiola *et al.* (2006) using vertical rigid obstacles in a flume show the same results in term of local logjams around the standing trees. However, it is difficult to precisely predict the size and residence time of individual jams (Wohl *et al.*, 2019). In the low-magnitude disturbance sites however, the wood load and the number of jams are much greater in the channel than on the floodplain (Wohl *et al.*, 2018).

Fig. I.5(a) compares the effect of increasing the flow discharge on two different kinds of woody materials carried by rivers in a schematic view based on Turowski *et al.* (2013) (for coarse wood CW) and MacVicar & Piégay (2012) (for large wood LW). As it is seen in this figure, the discharge of CW is always increased by increasing flow discharge. Turowski *et al.* (2013) proposed a rating curve of the form $Q_w = aQ_f^b$, with

Figure I.4: Example of floodplain jams pinned by living vegetation along (from Wohl *et al.* (2018)). Flow is from left to right, as indicated by white arrow; channel is at rear of photo, and person for scale is within white oval at right of upstream-most jam.

$a = 4.42 \times 10^{-15}$ and $b = 4.47$ for coarse wood (schematized by a dashed line in Fig. I.5(a)).

While in the case of coarse wood Q_w has a direct relation with Q_f, for the large woods MacVicar & Piégay (2012) found a big non-monotonic behavior at Q_{bf} for large wood discharge. They used a three stage model with RMS error of 16% compared to the field data on the Ain River (solid line in Fig. I.5(a)), to illustrate this behavior. As it is seen in this figure they proposed two thresholds for the relation between Q_w and Q_f, the first one for the start of wood motion and the second one for the maximum value of wood discharge. In this model wood mobilization occurs at 0.67 bankfull discharge Q_{bf}. Then the wood discharge increases with a linear positive trend until Q_{bf} beyond that wood transport rates are considered to be insensitive to flow discharge. In the third stage during the falling limb of the hydrograph, wood discharge has a constant value, much smaller than the rising limb (Fig. I.5(a)). By presenting the proportion of mobilized wood as a function of the flow discharge, Kramer & Wohl (2017) show almost the same pattern for the probability of wood mobilization (Fig. I.5(b)) with a sudden increase at bankfull discharge from 30% to 80% (Fig. I.5(b)). Note that MacVicar & Piégay (2012) (Fig. I.5(a)) measured instantaneous discharge of newly recruited wood on an actively eroding meander bend while Kramer & Wohl (2017)(Fig. I.5(b)) measure the ratio between mobilized wood and total stored woods. Kramer & Wohl (2014) reported 0.8 bankfull discharge for the inception of a significant wood mobilization.

In addition to some key discharges *e.g.* 0.67 Q_{bf}, Q_{bf} and Q_{max}, the temporal vari-

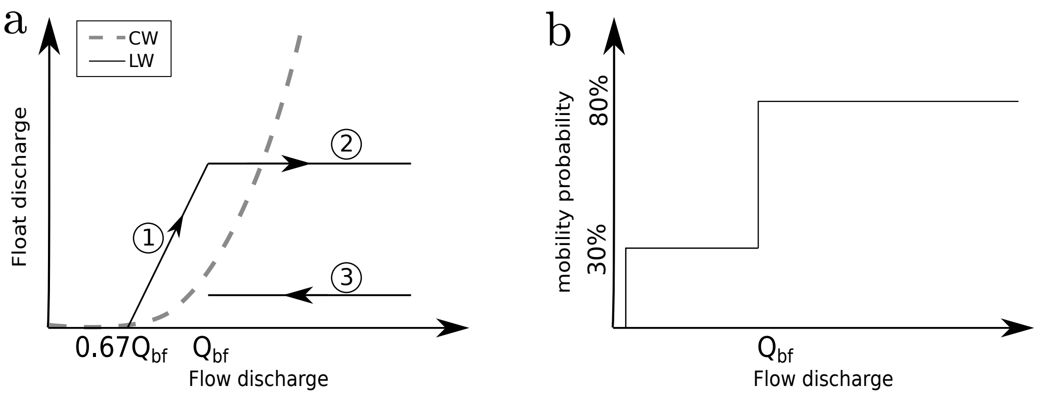

Figure I.5: Effect of the flow discharge on wood mobility. a) Comparison between wood and flow discharges for two different kinds of woody materials carried by rivers: (i) large wood *LW* based on bankfull discharge Q_{bf} as reference value, adapted from MacVicar & Piégay (2012)(solid line) and (ii) coarse wood *CW* adapted from Turowski *et al.* (2013) (dashed line). b) Possible mobility thresholds outlining a mobility envelope based on (Kramer & Wohl, 2017). Note that both figures are schematic and the values are not at scale

ation of flood, known as the flood hydrograph, is another effective parameter on the nonlinear relation between wood fluxes and flow discharge so that at similar discharges, larger wood is transported during the rising limb (first and second stage on Fig. I.5) than during the falling limb (third stage on Fig. I.5) (MacVicar & Piégay, 2012; Kramer & Wohl, 2014; Ruiz-Villanueva *et al.*, 2019). MacVicar & Piégay (2012) describe this effect as a hysteresis effect and show that due to this phenomenon wood transport during the falling limb is about one quarter of the rate during the rising limb (Fig. I.6). For further discussion, we can add, the wood may deposit in some locations such as the channel margins during the falling limb, but the increasing depth of water means that they are likely to be remobilized during the next flood event (Wohl *et al.*, 2018). Therefore, if flood occurs in areas such as outer banks, rising water levels cause the wood to be mobilized more than falling water level.

I.4 Dynamics of a single piece of wood

In the previous section, it is showed that nowadays wood fluxes are considered as a potential hazard in rivers and it is seen that flood discharge is the main factor, governing the wood fluxes in rivers. Once large wood mobilized, hazard is dependent on the individual motion of wood pieces. The dynamics of an individual piece of wood is important because modeling the motion of the wood is a useful tool for deciphering complex morphological processes related to the large woods, and knowing the dynamics of a single piece of wood help us to better understand the interaction between wood and instream hydraulic structures, *e.g.* bridge piers or retention structures.

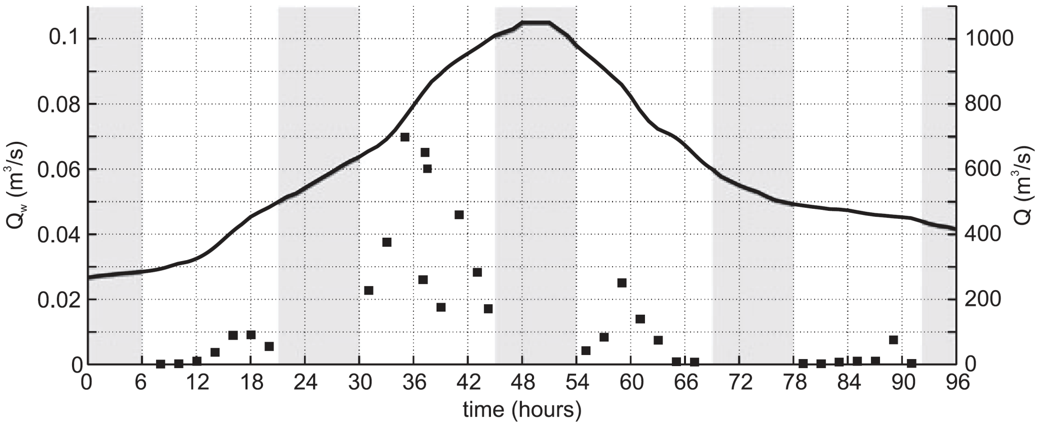

Figure I.6: Comparison between flood discharge (line) and wood discharge (squares) show that there is more wood during the rising limb than the falling limb (MacVicar & Piégay, 2012). The grey areas are the night time when wood detection is not possible

The motion of floating wood at the flow surface can be predicted by two different approaches: (i) a "kinematic" approach considering that the object acts as tracers following the flow and (ii) a "dynamic" approach based on the forces acting on the object. In the following both approaches are reviewed.

I.4.1 Kinematic approach

In the kinematic approach, it is assumed that the piece of wood moves like a passive tracer in a river with the same velocity as the surrounding flow and the wood's trajectory is identical with the river streamlines. In particular due to its small computational costs, this approach has been used in different fields to model the motion of a solid particle in a fluid environment. For example, in oceanography, the kinematic approach has been applied to simulate transport and accumulation of marine debris, providing consistent results with data extracted from different cleaning operations as benchmarks (Hainbucher *et al.*, 1987; Mansui *et al.*, 2015). This approach has also been tested in a recent study of wood motion in rivers (Ruiz-Villanueva *et al.*, 2014*a*). In this study, the authors use a "semi-tracer" model assuming that the floating pieces of wood have a velocity slightly lower than that of the flow. This model provides a good agreement with experiments, showing that this approach is able to predict and simulate the deposition locations of the wood along the river and to reproduce the interaction between wood and infrastructures.

Additionally, there are some evidences on the field that confirm this approach. MacVicar & Piégay (2012) compare the wood and flow velocity across the river and show that the wood pieces across the river have the same velocity as the flow. Figure I.7 is an example that confirms the agreement between flow surface velocity measured by

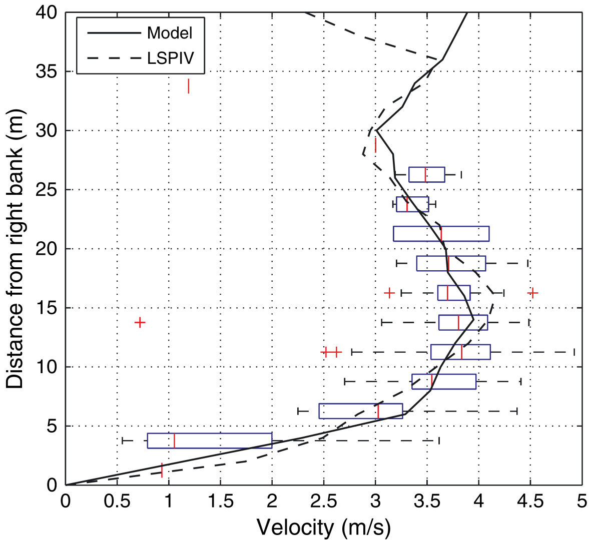

Figure I.7: Boxplot of velocity of the wood pieces at discharges between 800 and 1000 m^3/s compared with velocity measures by Large-Scale Particle Image Velocimetry (LSPIV) measurements at discharge equal to 895 m^3/s and by 2D hydraulic modeling on the Ain River (MacVicar & Piégay, 2012).

Large-Scale Particle Image Velocimetry (LSPIV) and wood velocities (Boxplots) even near the right bank where the velocity gradients are visible. One can note that using passive surface tracers is commonly used as a proxy for measuring surface velocities in laboratory experiments (Meselhe *et al.*, 2004; Bieri *et al.*, 2009) or in the field (Fujita *et al.*, 1998).

I.4.2 Dynamic approach

On the other hand the dynamic approach is based on Newton's second law and requires to compute the forces exerted by the fluid on the object. Such an approach is widely used for describing the motion of particles fully immersed in turbulent flows (Toschi & Bodenschatz, 2009; Balachandar & Eaton, 2010), and relies in the general case on the Basset-Boussinesq-Oseen (BBO) equation, describing the advection of a solid spherical particle in an unstationary and nonuniform flow (Maxey & Riley, 1983).

The BBO equation is valid for small particles compared to the flow scales, and was initially derived at zero particulate Reynolds number so that $Re_p = |\mathbf{v} - \mathbf{u}|D/\nu$, where D is the diameter of the object and ν is water kinematic viscosity. This equation is validated experimentally for the Re_p up to 1 for a solid spherical particle by Bergougnoux *et al.* (2014). This study showed that for low particulate Reynolds numbers, the experimental trajectories agree well with the BBO equation.

This equation has been extended for nonspherical objects and for moderate to large

Re_p (Magnaudet, 1997; Yin *et al.*, 2003; Mandø *et al.*, 2007; Mandø & Rosendahl, 2010; Benitz *et al.*, 2016). Results show that by some modifications such as using quadratic drag force or adding the lift force to general equation, this model works well for large Reynolds nonspherical objects. At larger values of the Re_p (up to 10^3), quadratic expressions for the drag and lift forces provide accurate results (Howe, 1995; Magnaudet & Eames, 2000). These results are not restricted to spherical objects, and several studies have shown that the BBO model equation is indeed valid also for rod- and disk-like particles (Voth & Soldati, 2017; Yin *et al.*, 2003; Mandø & Rosendahl, 2010). Whereas most studies based on this dynamic approach consider immersed particles (neutrally buoyant or not), only a few use this approach to the case of objects floating at a free surface. Recently, Persi *et al.* (2018*a*,*b*) showed that a surface version of the BBO equation provides accurate modeling of the same experimental trajectories in a meandering channel flow as those of Ruiz-Villanueva *et al.* (2014*a*).

I.4.3 Effective parameters on impact process

In front of an obstacle in addition to the interaction between flow and piece of wood which can be modeled either by kinematic or dynamic approaches, the additional complexity due to the interaction between obstacle and wood piece should be taken into account.

The effect of the characteristics of bridge structures with or without pier on the process of impact has been studied, and it is shown that the shape of baffle on a bridge and the geometry of the bridge pier both play role on the impact process (Schmocker & Hager, 2011; Lagasse, 2010; Cicco *et al.*, 2018).

Wood geometry in the field is associated with complexities and irregularities such as roots or branches. Increasing the irregularity of log shape is also likely to increase probability of impact (Schmocker & Hager, 2010; Cicco *et al.*, 2018). Presence of root or branches increase the stability of the wood in river (Braudrick & Grant, 2000; Comiti *et al.*, 2008). Moreover, Braudrick & Grant (2000) studied the effect of log orientation and show that pieces oriented parallel to flow are more stable than pieces perpendicular to the flow. In summary it seems that in addition to the wood dynamics in the river, both wood and bridge characteristics play role in the process of impact.

I.5 Objectives

Based on the aforementioned statements, to be able to quantify the potential hazards associated with large wood in a river, it is important to study the amount of wood pieces in a river as well as the motion of each single piece of wood. Therefore, here we follow two main objectives:

1- Correlation between driftwood discharge and flood characteristics.

For quantifying the amount of wood, the wood fluxes should be monitored in the river. Therefore, the chapter II of this thesis is dedicated to quantify the amount of wood in a river using streamside video monitoring technique on the field, in order to validate or modify the existing pattern between Q_w and Q_f (Fig. I.5(a) on the Ain

River) by measuring the wood discharge during two floods with discharges more than Q_{bf}, on the Isère River (France). The other objective of this chapter is to find a link between some easy access parameters like flow discharge, wood fluxes and the inter-flood time and the wood discharge as a more complex parameter.

2- Motion of an individual piece of wood in a river.

It is also mentioned that it is necessary to study the dynamics of each individual piece of wood in order to be able to analyze the behavior of wood fluxes in a river . Therefore, the chapter III of the thesis is a combination of field work, experimental measurement and numerical model in order to study the dynamics of an individual piece of wood in river. For modeling the motion of a floating wood in river, comparison between kinematic model and dynamic model raises the question of finding a criterion for the validity of the kinematic approach as using this approach is much simpler and faster for calculating wood transport in a river. Therefore, our main dedication at this part is to analyze the validity of both approaches in order to provide conditions under which a piece of wood would behave as a flow tracer. Additionally, as the second goal of this chapter, the effect of wood dynamics and geometry complexities are considered experimentally as the effective parameters on impact process.

Chapter II

Correlation between driftwood discharge and flood characteristics

This chapter aims at assessing a method for estimating some wood characteristics such as log length, wood fluxes and discharge during flood events to be able to connect them to the river flow characteristics. Since the significant wood recruitment and transport are mainly related to flood events, it is worth searching for a method to assess wood flux in a safe way and far from the river. In the present work, we decided to focus on a video surveillance technique from the river banks. To do so, we provide data from a new camera located on the Isère River, near Grenoble.

The chapter is organized as follow. The first section presents the study site on the Isère River parallel to a site previously studied by (MacVicar & Piégay, 2012) in order to test the generality of the method. Second section is thus devoted to the measurement techniques *e.g.* principle, new incomes compared to previous studies, image processing, correction methods and uncertainties. The third section exposes the results concerning wood size, wood fluxes and finally the wood discharge. Fourth section discusses physical aspects, notably the link between wood, flood discharge and inter-flood time; it also explores the possibility to obtain the wood discharge using simpler direct measurements, as the wood flux.

II.1 Study sites

II.1.1 Ain River site

Before introducing the new field experimental site, we remind here the site previously used by the team (EVS) on the Ain River, France (Fig. II.1). The Ain River is a piedmont river with a drainage area of 3630 km^2 at the gauging station of Chazey-sur-Ain, with an active channel width of 65 m, a mean slope of 0.15%, and has a mean annual discharges of 120 m^3/s. The lower Ain river is characterized by an active channel shifting within a forested floodplain (Lassettre *et al.*, 2008). Based on MacVicar & Piégay (2012), the bankfull discharge at the local scale on study site is 530 m^3/s. Here,

Table II.1: Conditions at a local level

River	**Coordinates (m)**		**Watershed**	**Mean slope**	**Sinuosity**	**Flow discharge** Q_f **(m^3/sec)**					
	East	**North**	**Area (km^2)**	**(m/km)**		Q_{Annual}	Q_1	Q_{bf}	Q_2	Q_5	Q_{10}
Isère	717482	5008613	5720	1	1.1	179	475	550	590	770	900
Ain	673226	5086106	3630	1.5	1.5	120	715	840	900	1200	1400

Table II.2: Brief report of five monitored floods

River	**Date**	**Flow discharge** Q_f		**Max daylight** Q_f		**analyzed**	**Color**	**Symbol**
		m^3/sec	**year**	m^3/sec	**year**	**video**		
Isère	03 to 06/01/2018	808	6.5	670	2.6	40 hr	dark blue	I-JAN18$_1$
	20 to 23/01/2018	563	1.5	563	1.5	40 hr	light blue	I-JAN18$_2$
Ain	22 to 24/11/2007	578	0.6	578	0.6	6 hr 15 min	yellow	A-NOV07
	10 to 12/12/2007	616	0.7	616	0.7	3 hr 45 min	orange	A-DEC07
	10 to 13/04/2008	1050	3	1006	2.3	7 hr 45 min	red	A-APR08

to have a same criterion on both rivers, the 1.5 year flood is used as an approximation for the bankfull discharge all along the river. For the Ain River, 1.5 year flood is 840 m^3/s. The survey period on this river was from February 2007 to June 2008. During this period, three floods were studied, including two slightly lower than the bankfull flood in November and December of 2007 (A-NOV07, A-DEC07) and a third flood in April 2008 (A-DEC08) with a 3 year return period (MacVicar & Piégay, 2012). All the monitoring data on the Ain, used in this thesis, were collected from MacVicar & Piégay (2012). Table II.1 provides a summary of hydrological information and local conditions on both studied rivers, based on 60 years data. Table II.2 provides a brief report of monitoring wood flux during 5 floods on both rivers.

II.1.2 Isère River site

The study site is located on the Isère River at Grenoble, France. With a snowy-rainy regime, the Isère River is one of the main tributaries of the Rhone basin. The Isère River flows from the western parts of the Alps through a mountainous and steep valley to Albertville, after which it flows south for 90 km through a wide alluvial plain until Grenoble. In the alluvial plain, river has been embanked, affected by intensive gravel mining in the bed, and vegetation encroachment (Jourdain *et al.*, 2017; Serlet, 2018; Serlet *et al.*, 2018). Upstream from Grenoble, the Isère River is composed of two main tributaries, the Arly and Arc Rivers (Fig. II.2). The length of the river to the studied area is 150 km and the catchment area is 5720 km^2 (www.hydro.eaufrance.fr). The 1.5 year flood, as an approximation for bankfull discharge for the Isère River, is 550 m^3/s. The river has a steep slope of about 5% upstream of Albertville, and then with a mild slope about 0.1% goes to the Rhone River. The average total annual rainfall in this basin is about 986 mm. The monthly discharge of the river in a period of 60 years in

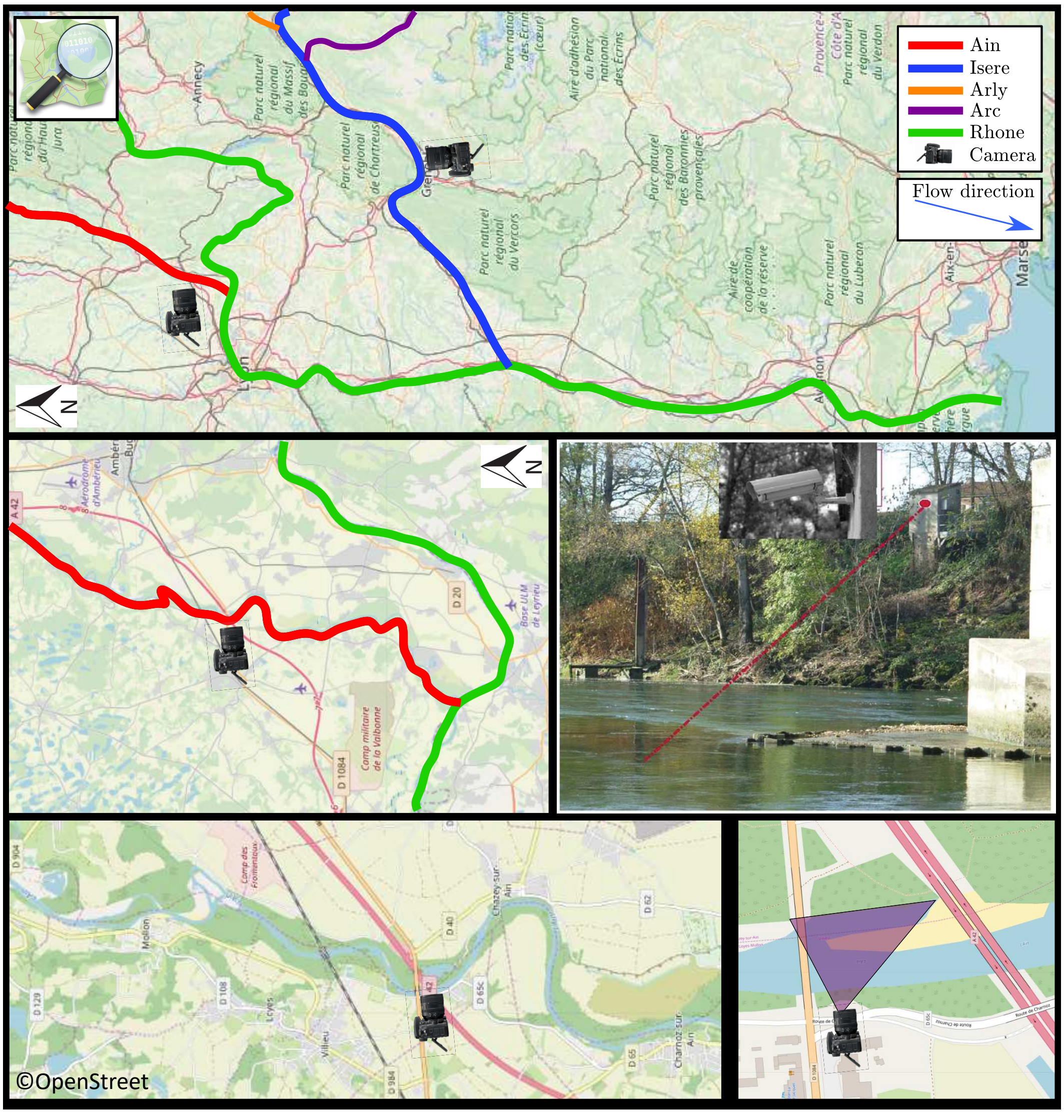

Figure II.1: Previous study site, located on the Ain River at Chazey sur Ain. Camera is installed on the station and its view angle is presented by the purple triangle. The maps are taken from (www.openstreetmap.org) website.

Table II.3: Surface velocity measurement on the Isère River

Date	Flow discharge m3/s		Surface velocity m/s		River
	mean daily	max	surface average	max	width m
15/11/2017	100	166	1.09	1.41	54.50
05/01/2018	678	808	2.00	2.65	75.64
23/01/2018	500	555	2.00	2.56	71.38
24/04/2018	350	434	1.81	2.26	69.08

Grenoble is 179 m^3/s and the annual volume of the river discharge is 5.6 km^3 (Table II.1).

A hydrology station is placed on left bank of the river in Grenoble, Campus of University Grenoble Alpes. The station is located along a mild meander with sinuosity of 1.1. The data at the gauge near the station is used to estimate the rating curve (Fig. II.3(a)). Streamwise surface velocity is measured at four discharges using Large-Scale Particle Image Velocimetry (LSPIV) and bathymetry was obtained from the simultaneous Acoustic Doppler Current Profiler (ADCP) measurements by a private company (TENEVIA. Co) (Fig. II.3(b)). Table II.3 shows a brief summary of surface velocity measurement on the Isère River.

Continuous water level information has been recorded at the station from 1980 and then it is converted to discharge available on (www.hydrobanque.com) website using the rating curve of station(Fig. II.3(a)). As it can be seen in Fig. II.4 during this period the maximum flood happened on 2/5/2015 with $Q_{max} = 966$ m^3/s and mean daily discharge of 863 m^3/s. In total, 8 events with $Q_{max} > 800$ m^3/s have been recorded. The study period on January 2018 contains two flood events. The first event from 3 to 6 Jan 2018 with Q_{max} =808 m^3/s and a second event from 20 to 23 Jan 2018 with Q_{max}=563 m^3/s. The studied periods are indicated on Fig. II.4.

Isère River is a watercourse that has potential of wood recruitment and transportation. The main source of this instream wood on the Isère River is bank erosion (Le Lay & Moulin, 2007; Piégay *et al.*, 2017). Based on this study, fresh trees with attached leaves are not frequent in this river. On the Isère River, in many cases, the wood is deposited near its recruitment point, so that half of the observed woods by Piégay *et al.* (2017) are trapped after 15 km from the recruitment point and 80% of them after 35 km. In this basin the characteristics of instream deposited woods do not change significantly, but there is high variation in temporal mobilization and deposition in term of species and size (Piégay *et al.*, 2017). Additionally, recruitment process is strongly influenced by the channel size, and active bank erosion, as the main mechanism of production of instream wood on this study area, occurs during frequent floods ($Q_{max} < Q_{10}$) where Q_{max} is the maximum flow discharge and Q_{10} is the 10 years return period flood (Piégay *et al.*, 2017). As a consequence, there is a potential hazard in term of wood pieces dur-

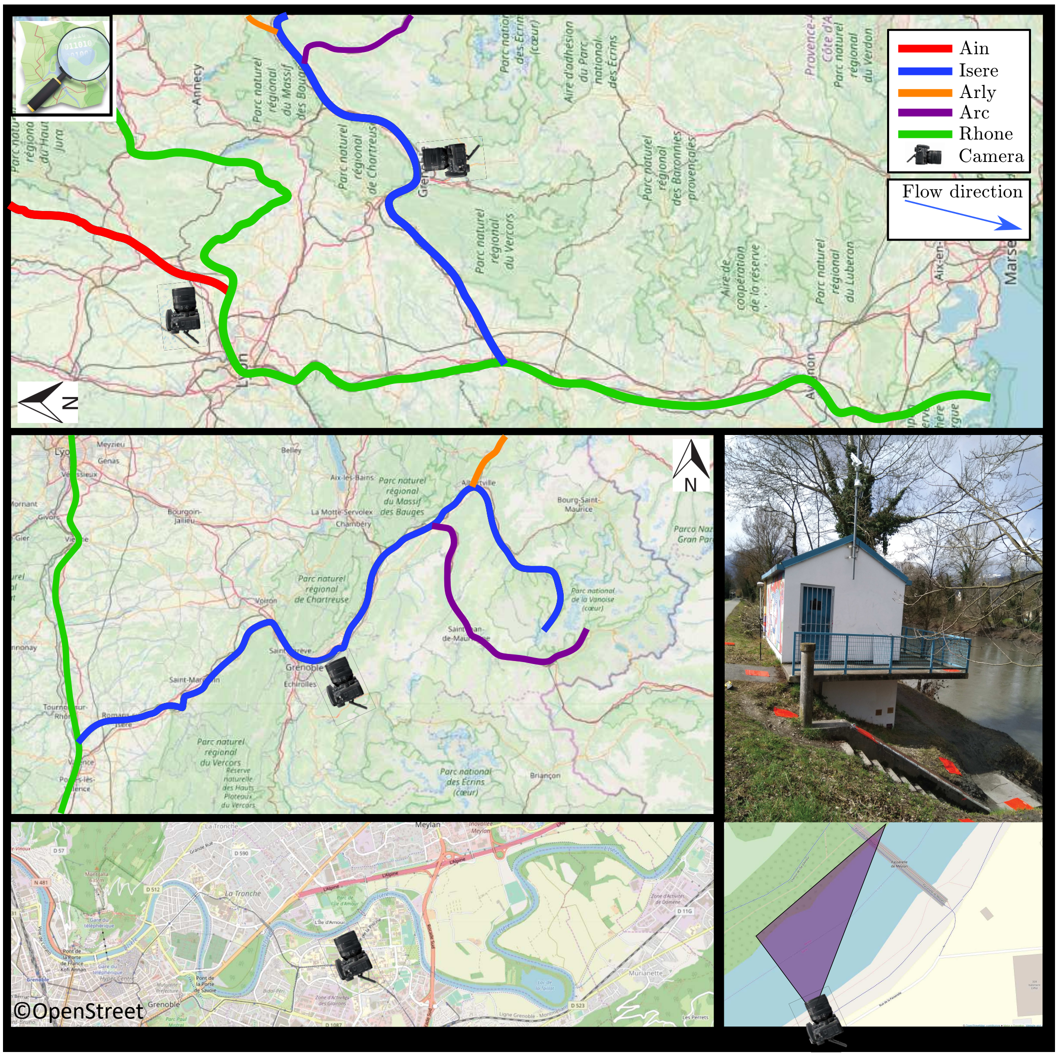

Figure II.2: Study site, located on the Isère River at Grenoble, the campus of University Grenoble Alp. Camera is installed on the station and its view angle is presented by purple triangle. The maps are taken from (www.openstreetmap.org) website.

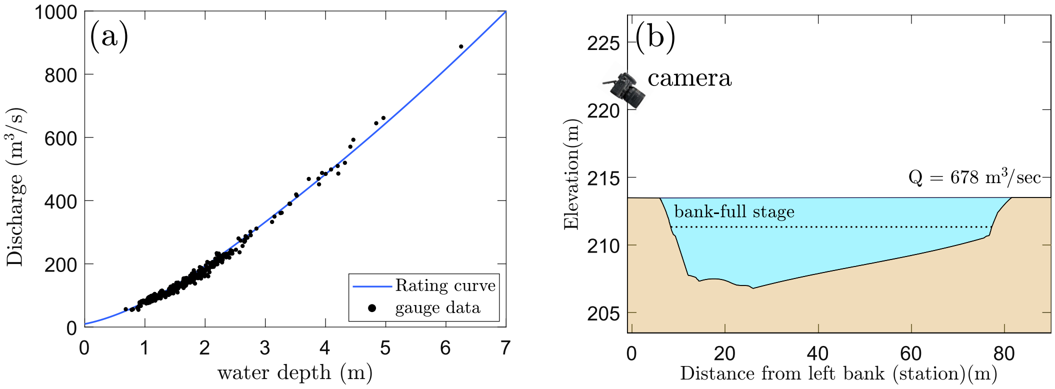

Figure II.3: (a)Rating curve based on the recorded data on the gauging station and (b) river bathymetry at gauging station based on field measurement by TENEVIA Co..

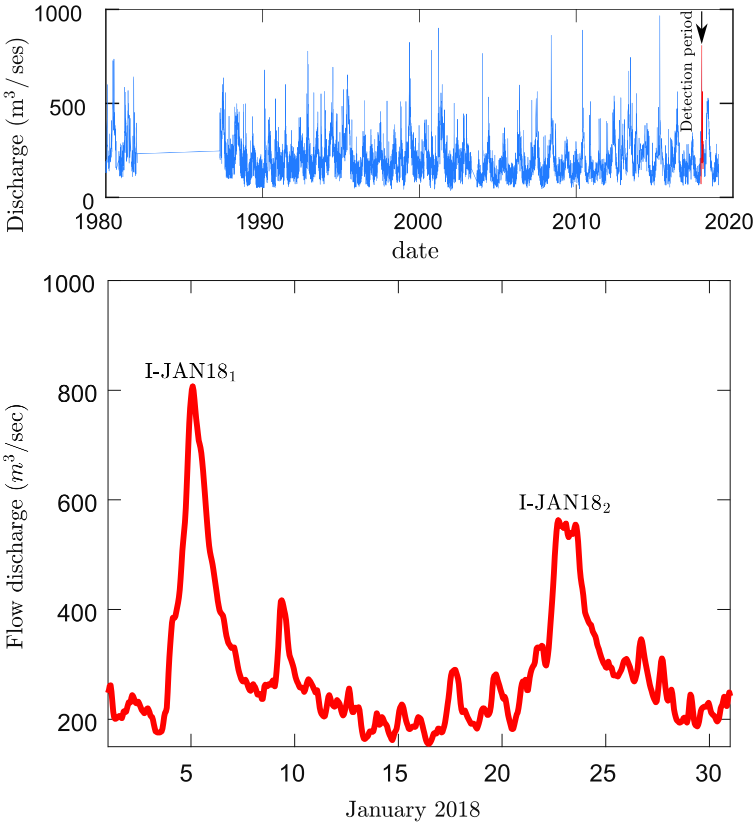

Figure II.4: Recorded daily discharges on the Isère River (www.hydrobanque.com).

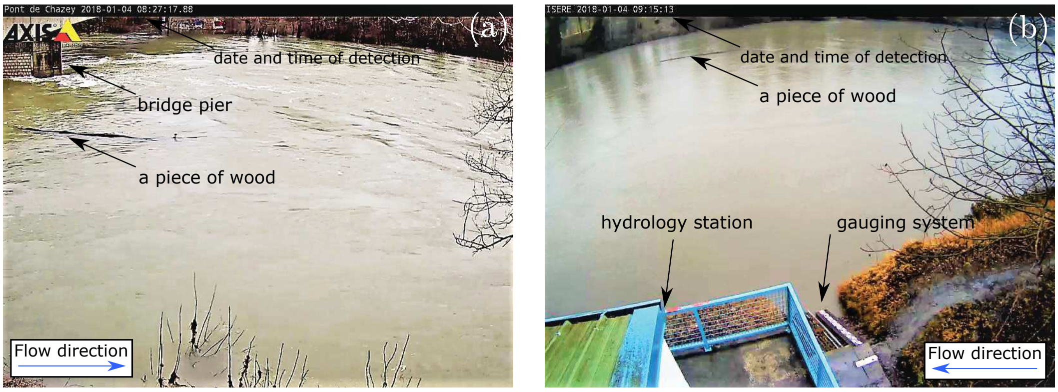

Figure II.5: Example of the field of view of the camera on the Ain River (a) and on the Isère River (b).

ing different flood events on the Isère River, which makes it necessary to monitor it and quantify the amount of wood in this river.

II.2 Material and Methods

As it is mentioned in the introduction, different observations in the river show that during the base-flow in a river wood discharge is negligible (MacVicar & Piégay, 2012; Kramer & Wohl, 2014). Wood discharge increases significantly during flood events and decreases very fast by decreasing flood discharge. Therefore, to study the wood mobilization in river, it is more efficient to monitor the pieces of wood during flood events. That's why here a flood event is selected as temporal framework to monitor wood discharge. To be able to capture this temporal framework, the temporal resolution of minutes to hours is needed. Therefore, monitoring pieces of wood at the surface by video monitoring technique would be the best strategy in this work. In the present section the material and methods to assess wood fluxes on the river by this method are described.

II.2.1 Camera

The camera used on the Ain River, was an AXIS221 Day/Night^{TM} with the resolution of 800 × 600 and at a maximum frequency of 5 Hz. The camera is located on the side of the river closest to the thalweg and the height of the camera is 9.8 m above the base flow, at Easting of 673226 m and Northing of 5086106 m. There is a bridge pier in the middle of the river upstream of the field of view, which is supposed to affect the motion of the wood. Figure II.5(a) is an example of the field of view of camera on the Ain River. On this figure, the date and time of detection, the upstream bridge pier and a piece of wood are presented.

The new camera, used in present study, is an AXISP3346 camera, installed at the gauging station on the Isère River(Fig. II.5(b)). This camera has a resolution of 800

× 600 and is set to record the water surface at a frame rate of 5 Hz. The camera is located at an elevation of 220.6 m above sea level, which is 8 m above water level at bankfull discharge, at Easting of 717482 m and Northing of 5008613 m. The camera is on the outside of a bend among a meander with a radius of 0.75 km, and looks out across the river. The location was chosen because a gauging station is already operating and equipped with internet access. In addition, the site is located on a high embankment on the outside of a bend. The station is located 150 m downstream of a bridge without middle pier, which is expected to have little effect on the flow patterns. This camera which is operated by laboratory LTHE of Grenoble, was connected to EVS, in Lyon, on December 2018 by an Intranet connection with a live access. Figure II.5(b) shows the position of the gauging system and of the station in a frame from this camera. Next section details how relevant information is obtained from the videos.

II.2.2 Detection process

The first wood characteristic to measure is the so-called "wood fluxes", *i.e.* the number of the wood pieces per unit time. As mentioned in chapter I lack of contrast between flow and floats due to the different factors such as lack of illumination or weather condition make it difficult to detect wood automatically on a river. Though there are some works to detect the floating pieces of wood in rivers the results were not accurate on the Isère River (Ali & Tougne, 2009; Ali *et al.*, 2011, 2012, 2014). With this purpose, a manual algorithm is implemented in Matlab R2017a, reproducing the one used by MacVicar & Piégay (2012), to record wood pieces and their trajectories within the monitored stretch.

In this manual algorithm, video is stopped by the user when a piece of wood is visible. Both ends of the wood piece are recorded using the screen cursor as shown in Fig. II.6. The video is then advanced frame by frame and the endpoints of the wood are relocated using the screen cursor to provide detection at each frame. The object is detected frame by frame because increasing the number of detection reduces the uncertainty of detection (more information in section II.2.4.3). As each object is repeatedly detected, a specific code was assigned to each object to distinguish between different objects. By this method the number of the woods and consequently the wood fluxes are measured for each flood. Note that though camera has 5 Hz frame rate to be able to check long videos, 1 Hz frame rate is used in manual detection.

Because wood sensing has been done by two different observors (B. MacVicar on the Ain, H. Ghaffarian on the Isère River), the observer bias is estimated by comparing the two observers wood detection results on a common set of videos. A comparison of the number of the wood pieces detected by each operator for 12 different 15 minute long videos is shown in Fig. II.7. Based on this figure, the R^2 measured by the 1:1 line is 0.96, which meaning that there is a good agreement between different operators in detecting the woods. However, the operator bias was thought to be less than 10%, which is a source of uncertainty in this study. To conclude, a direct use of the videos provides the number of the wood pieces, and by extension the wood fluxes, with a precision estimated to about 10% due to the operator.

Figure II.6: Wood detection on a field image using the screen cursor.

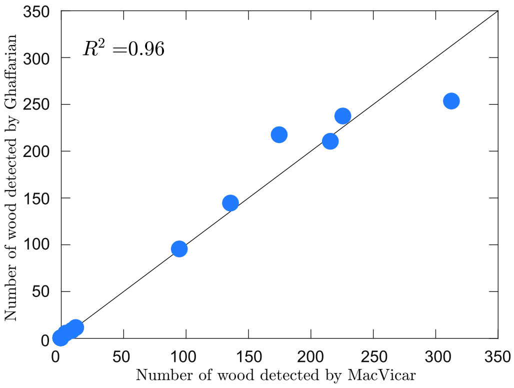

Figure II.7: Bias of observers on wood detection on a set of videos compared with [1:1] black line.

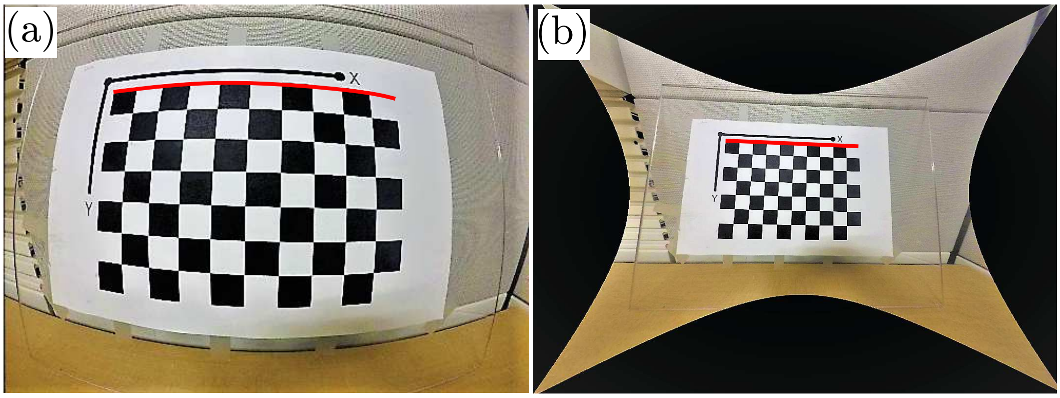

Figure II.8: Basis of fisheye correction on a chessboard in Matlab ComputerVisionToolbox^{TM} toolbox (www.MathWorks.com).

II.2.3 Correcting fisheye lens distortion

After detecting wood on videos, we then correct the fisheye lens distortion. A fisheye lens distortion is a characteristic of the lens that produces visual distortion intended to create a wide panoramic or hemispherical image. This effect has been corrected by a standard Matlab process using the ComputerVisionToolbox^{TM}. To solve fisheye lens distortion by ComputerVisionToolbox^{TM}, some steps have to be followed. First, by moving a chessboard in front of the camera, some frames from different distances and different angles have to be collected. More images with different angles and distances from the camera, reduce the errors. The toolbox loads these frames and detects the chessboard cross-sections automatically. The cross-sections of the chessboard provide a network and the curvature of the image is detectable on each line of the network as it can be seen on Fig. II.8(a). The Matlab toolbox then finds the correction matrix and apply it on the image so that all curved lines become straight as it is shown in Fig. II.8(b). Following correction of curvature of lines on the chessboard, the fisheye effect is removed throughout the figure.

On the field the same process has been implemented. As it is seen on Fig. II.9 a 13 × 10 chessboard with 80 mm squares is used for fisheye correction. An operator moves the chessboard in front of the camera and in total 40 frames were used to correct the fisheye lens distortion.

An example of the image before and after fisheye correction is shown in Fig. II.10. As it can be seen on this image, after correcting the fisheye lens distortion, the curved bank of the river becomes a straight line. Note that as in correcting fisheye effect some parts of the image are stretched, the size of frames increase from 600 × 800 to 810 × 1080. After correcting the fisheye distortion on all frames, in the next step the points on the image are rectified and transformed to real metric coordinates using orthorectification process.

Figure II.9: Using a chessboard on the field to correct the image fisheye distortion on video frames.

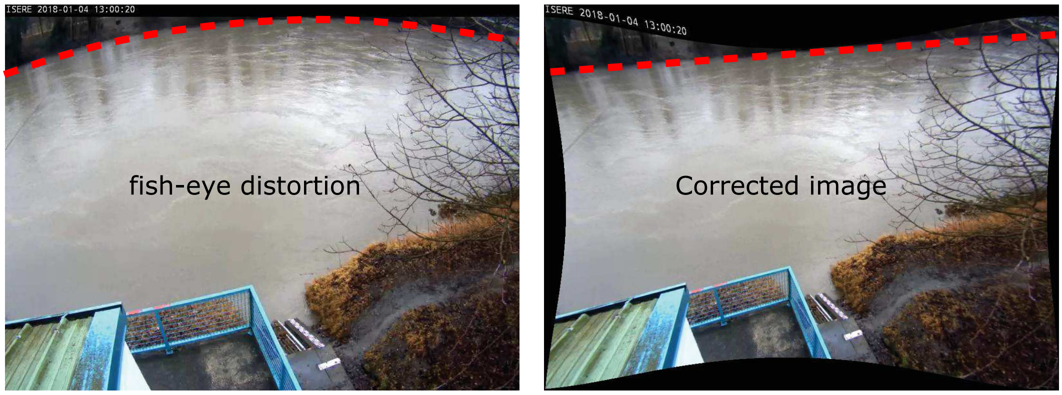

Figure II.10: An example of the video frames on the Isère River before and after correcting fisheye distortion.

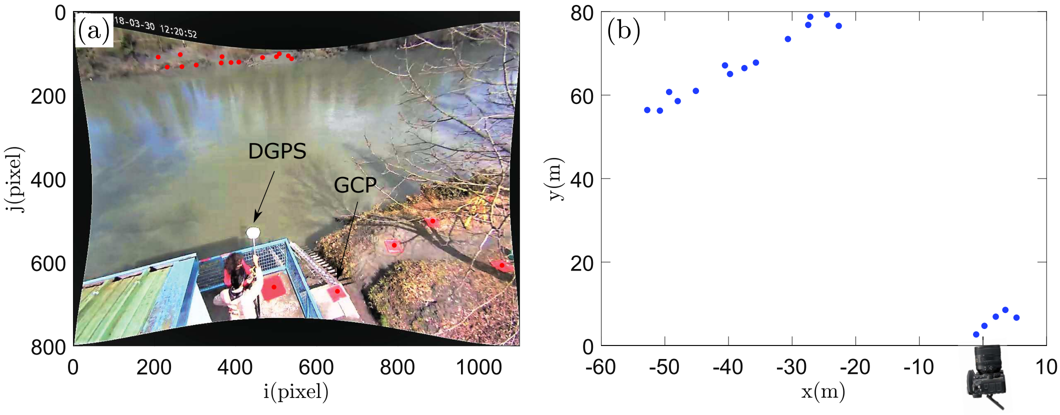

Figure II.11: GCPs measured on both sides of the river (a) in pixel coordinates as it is seen in video and (b) in metric coordinates as it is seen on the field.

II.2.4 Orthorectification

II.2.4.1 Introducing orthorectification

Ground-based cameras have an oblique angle of view, which means that pixel to meter correspondence is variable and images should be orthorectified prior to analysis (Muste *et al.*, 2008). Orthorectification refers to the process by which image distortion is removed and the image scale is adjusted to match the actual scale of the water surface. Orthorectification is accomplished by applying an appropriate image photogrammetric transformation (Mikhail & Ackermann, 1976), using known coordinates of Ground Control Points (GCPs). Ground Control Points (GCPs), also known as Ground Reference Points (GRPs), are defined as points on the surface of the earth of known location used to geo-reference the image. Here, 19 GCPs measured along both sides of the river using a Differential Global Positioning System (DGPS) Trimble RTK 5800 and white square targets that are visible in the image as shown in Fig. II.11 and presented in Table II.4. A DGPS is an enhancement to the Global Positioning System which provides improved location accuracy. On this figure, the GCPs are presented both in pixel coordinates, like what we see in an image (Fig. II.11(a)) and in metric coordinated (Fig. II.11(b)) with respect to the camera position at 0, 0 coordinates.

For orthorectification, two methods were implemented; first, we used the same method as MacVicar & Piégay (2012) based on the transformation matrix proposed by Fujita *et al.* (1998). After rectifying the images, comparison between rectified image and metric points shows a big difference of about 30 m, as shown in Fig. II.12. This difference would be due to some reasons: firstly, in the transformation matrices proposed by Fujita *et al.* (1998) there is not the effect of different elevations. Therefore, all GCPs are assumed to be at the same elevation while in our case GCPs are located at different elevations. Also, on this method, the best configuration of GCPs is when a homogeneous network

Table II.4: GCP coordinates in pixel and metric coordinates

GCP	Detected on image		Transformed from image		Measured by DGPS			Error	
code	i(pixel)	j(pixel)	X(m)	Y(m)	X(m)	Y(m)	Z(m)	X(m)	Y(m)
1	481	668	-3.4	1.8	-1.0	2.6	-4.9	2.4	0.7
2	636	678	-1.3	4.2	0.3	4.6	-7.8	1.6	0.5
3	775	568	1.1	7.1	2.1	6.8	-7.3	1.0	0.3
4	869	510	3.1	9.3	3.6	8.4	-7.2	0.5	0.8
5	1038	616	5.4	6.9	5.3	6.6	-7.0	0.1	0.3
6	220	142	-50.6	56.1	-50.7	56.2	-10.8	0.2	0.0
7	256	141	-47.6	58.2	-47.9	58.5	-10.9	0.3	0.3
8	291	137	-44.9	60.7	-45.1	60.9	-10.8	0.1	0.2
9	352	132	-39.6	64.7	-39.7	65.0	-10.7	0.1	0.3
10	376	131	-37.4	66.3	-37.4	66.4	-10.7	0.0	0.1
11	395	130	-35.6	67.5	-35.6	67.7	-10.8	0.1	0.2
12	453	119	-30.7	73.5	-30.6	73.3	-10.2	0.1	0.2
13	487	117	-27.5	77.0	-27.4	76.7	-10.4	0.1	0.3
14	516	115	-24.7	79.5	-24.5	79.2	-10.4	0.3	0.3
15	198	118	-52.6	56.2	-52.7	56.3	-8.6	0.1	0.1
16	252	112	-48.9	60.3	-49.3	60.6	-8.4	0.4	0.4
17	354	117	-40.3	66.9	-40.5	67.0	-9.5	0.2	0.2
18	494	110	-27.2	78.9	-27.1	78.7	-9.9	0.1	0.2
19	524	122	-23.2	78.6	-22.6	76.5	-11.0	0.6	2.1

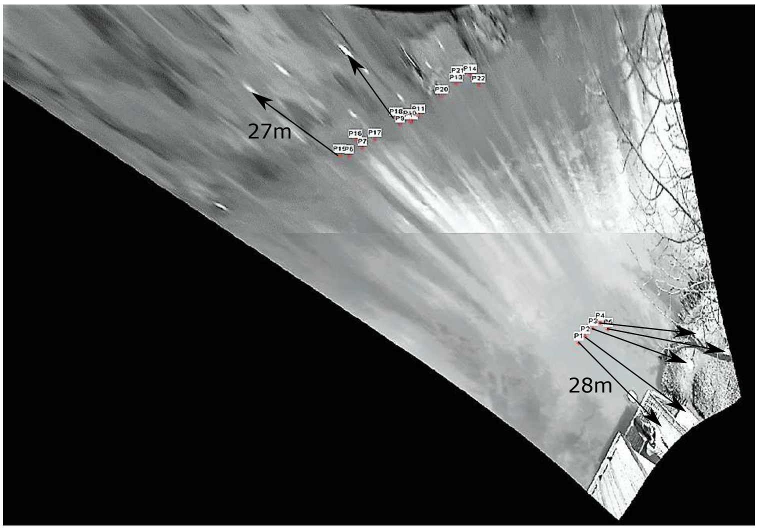

Figure II.12: Orthorectification results based on Fujita *et al.* (1998) transformation matrix using GCPs at different elevations. Arrows indicate the distance between real coordinates of the GCPs and the orthorectifyed data on a frame.

of points spreads throughout the image. In riverine environments, collecting GCPs at the middle of the river requires boat. But stabilizing the boat and collecting a network of GCPs across the river and in different heights is difficult and laborious. Thus we used another method which is explained in the following.

II.2.4.2 Rectifying process

The second method used for rectifying the images is assuming a virtual camera on the image and estimating the position of the camera and of its principal point (center of view). In this approach, there are 6 unknowns on virtual camera positioning: three coordinates (X, Y, Z) and three orientations (roll, pitch and yaw angles) as shown in Fig. II.13.

After collecting GCPs in real coordinates (X, Y, Z), the points are plotted in 3D coordinates (Fig. II.14(a)) with perspective projection. Removing grids from Fig. II.14(a) resulting in a 2D projection of the points on a plane (blue points in Fig. II.14(b)), which can be compared with what can be seen in the field image as GCP (red points in Fig. II.14(b)). By changing the position and angle of the virtual camera on Fig. II.14(a), the best match between 2D projected points and field GCPs is found. The best mach is measured so that on total, the distance between 2D projected points and field GCPs on the image (in pixel) multiple by the distance of the image from the camera (in meter) is minimized. Note that here we did not simply use the least square method because one pixel error on the points far from the camera causes much more error than the points near the camera. Therefore the distance of each point from the camera is used as weight

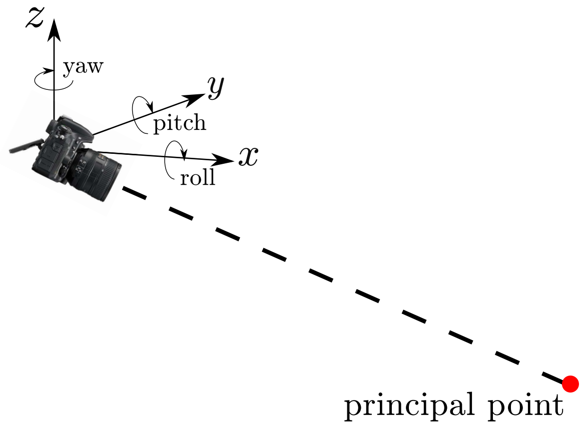

Figure II.13: Six unknowns, three coordinates (X, Y, Z) and three orientations (roll, pitch and yaw angles), on virtual camera.

on measuring error.

After identifying the virtual camera position, knowing the elevation of a point it is possible to transfer projected point anywhere in the field images to real coordinates. Note that the elevation of points in the images are known by transforming flow discharge to water depth using rating curve. The red points on Fig. II.14(c) represent the detected GCPs on video frame in metric coordinated. The precision of the method is evaluated by comparing these points with DGPS points (blue points on Fig. II.14(c)). All GCPs with corresponding error are presented in Table II.4. The average difference between transformed and measured points is 0.4 m with standard deviation of 0.5 m. There are different sources of error cause the difference between transformed coordinates from the image and the measured points by DGPS, such as error on detecting the i, j points on the image, error on DGPS and errors on fisheye correction. Note that some coding optimization in the future could decrease the time to find the virtual camera position, which is about 12hr currently.

The most important benefits of this approach in riverine environments are: The output of this method is a matrix, for all desired elevations (Fig. II.15), that can convert any pixel point in the image to a metric local coordinate. Note that on this image, to be able to present transformation matrices clearly, the Z axis, in vertical direction, is exaggerated, but the water level was typically at Z=-10 m (the first plane on the image). Based on this figure the objects seems bigger for higher water levels. The other positive point of this method is that with this new procedure, an acceptable accuracy can be obtained only with GCPs located on the river banks, without any point across the river width. Nevertheless it is required to have the GCPs well distributed on the river bank. This is a positive point in riverine environment where usually there is no access to the network of GCPs in the middle of the river.

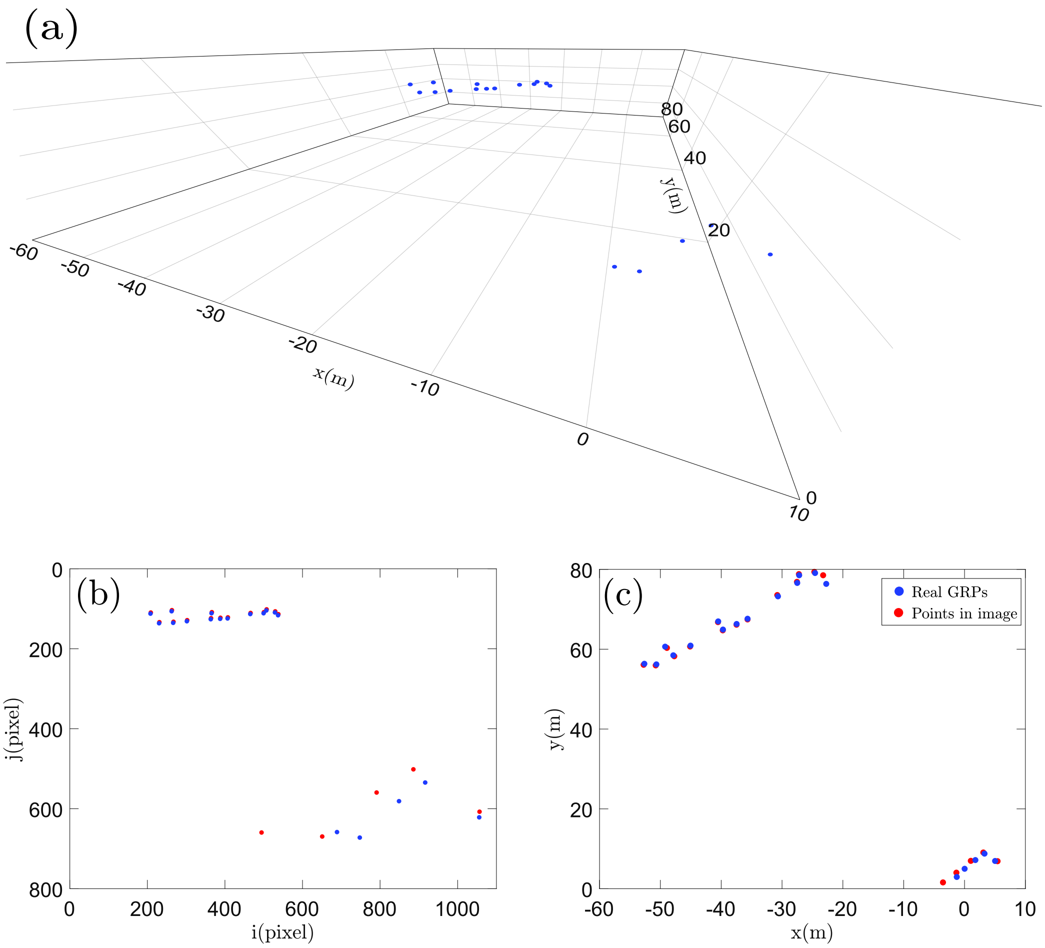

Figure II.14: (a) 3D view of GCPs in metric coordinates. Measured GCPs from the DGPS (blue points) and transformed GCPs from the video (red points) in pixel (b) and in metric (c).

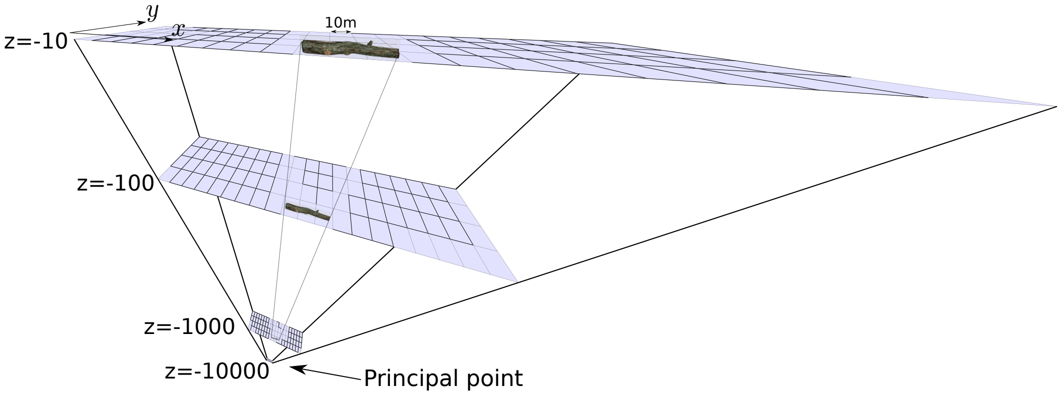

Figure II.15: Effect of different elevations (in Z direction) on rectify matrices.

II.2.4.3 Uncertainty on detection

On the video frames, two parameters cause uncertainty in detecting the exact positions of wood borders. The first one is the buoyancy of the wood, resulting in submerging some parts of the wood, and second one the large size of pixels far from the camera. Figure II.16 is an example for such an uncertainty in detecting the wood dimensions. On this figure, a blurry region around the wood is recognizable, but it is difficult to precisely determine the size of this region in pixel. Totally, based on different detection on different regions of the river, an uncertainty of 3 pixels is considered in each direction.

To measure the uncertainty on the detection of the wood length the following equation is used,

$$dl = \frac{2 \times N_{BP} \times PixelSize}{\sqrt{N_D}} \cong 1.5 \times PixelSize, \tag{II.1}$$

where dl is the uncertainty on detecting the wood length, N_{BP} is the number of blurry pixels on both sides of the wood (the prefactor of 2 is for both sides). The pixel size is then divided by square root of the number of consecutive frames on which one single object is detected N_D (For more information see (Meyer, 2007)). As mentioned N_{BP} is around 3 pixels and on average N_D is around 15 frames for each piece. From the image samples on the Ain River, we know that N_{BP} and N_D are in the same order as the Isère River. As a consequence, the uncertainty on detection of the wood length on both rivers is around 1.5 times the pixel size. The next step is to estimate the pixel size on the frame.

Figure II.17 shows visually the transformation matrix, at the low flow level on the Ain River (Fig. II.17(a)) and the Isère River (Fig. II.17(b)). In both cases, the camera is located around 10 m higher than the flow surface. Knowing the water elevation with respect to the camera position, the corresponding transformation matrix can be performed. Figure II.17(a) shows the horizontal size of pixels on the Ain River based on MacVicar & Piégay (2012). On Fig. II.17(b), coordinates on a frame using the camera

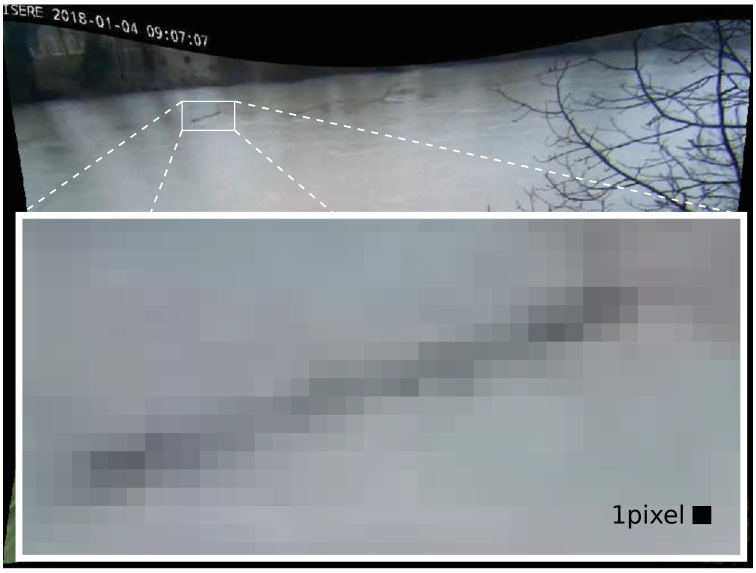

Figure II.16: Uncertainty on detection of the wood length due to the blurry area at the borders of the object.

as the origin is presented in red color, while sizes of pixels on each grid are shown in black. The borders of this figure are curved because the fisheye distortion is corrected on this image; conversely a straight line in reality is presented without any curvature in the image. Remind that both these images provide the pixel size for only one water stage, and by changing water level, this size changes. In addition, based on Fig. II.17(b), the size of pixels is not the same in both directions, meaning that after orthorectification, pixels are not square any more.

On Fig. II.17(a), (b) we can see that the top of the frame near the other river bank appears as the worst position to detect a wood, as the size of pixels are of the order of 1 meter. To show the effect of detection at distances from the camera Fig. II.18 shows the wood length distribution and pixel size across the river on the Isère and Ain. Each boxplot on Figs. II.18(a), (b) represents the length distribution every 5 m interval across the river. Based on these figures, in both rivers, length distribution is much smaller, near the camera. Getting away from the camera the range of detected wood size is larger. One probability is that the natural transverse distribution on length is the same as presented here. The other possibility is, this transverse distribution can be due to the fact that near the camera most of the floating woods can be detected while away from the camera typically larger woods are detected easily but many smaller woods are not detected. Therefore, the boxplots show larger woods far from the camera.

After around 60 m from the camera on both rivers, no wood is detected. This latter zone on the Isère River, which is presented by grey region on Figs. II.18(a), (c), can be considered as a blind zone for the camera, as the pixel size becomes larger than the wood diameter and therefore, wood detection on this region is almost impossible. The

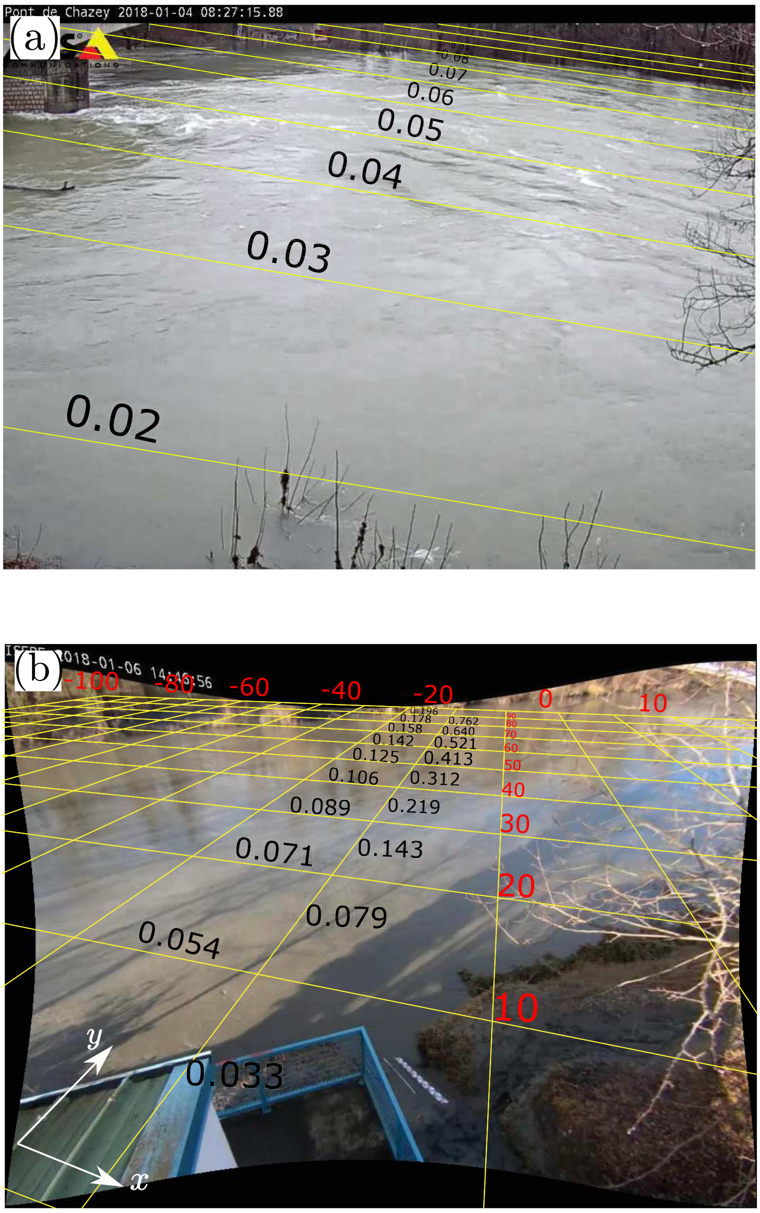

Figure II.17: Rectifying transformation matrix at low flow level (a) on the Ain River (MacVicar & Piégay, 2012) and (b) on the Isère River. Black fonts correspond to the average size of each pixel on the Ain River in meter and vertical and horizontal size of each pixel on the Isère River in meter and red fonts on the Isère River are the coordinates with respect to the position of the camera at (0,0).

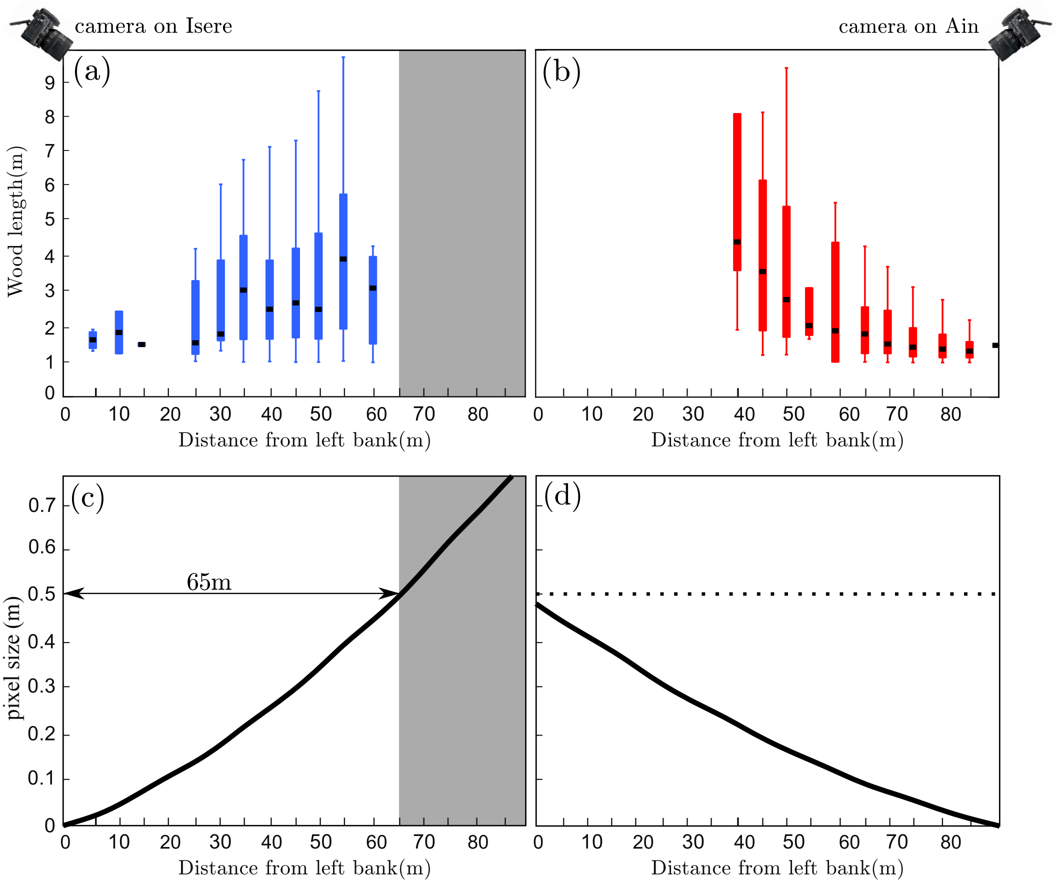

Figure II.18: Distribution of wood length across the river (a) on the Isère River and (b) on the Ain River. And pixel size across the river (c) on the Isère River and (d) on the Ain River. More than 65 m far from the camera on the Isère River no wood is detected, therefore, the gray zone on the Isère River depict the blind area

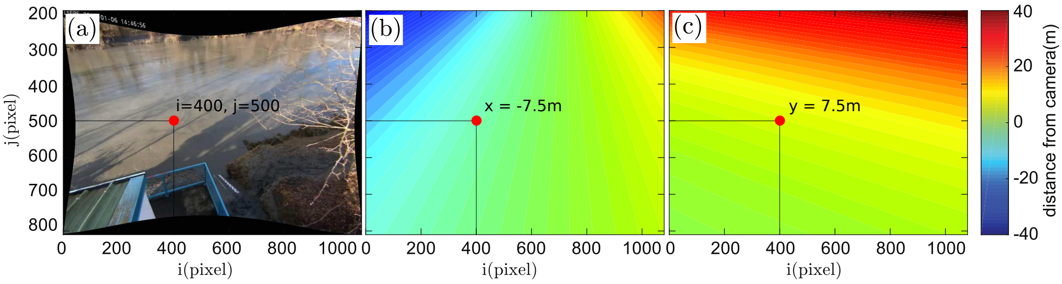

Figure II.19: Transformation matrices. (a) a video frame at bankfull elevation and corresponding transformation matrices on (b) X direction and (c) Y direction.

pixel size in this region is of the order of 0.5 m and detecting wood pieces with diameter less than the pixel size is impossible. From the other hand, the pixel size on the Ain River is limited to 0.5 m far from camera (Fig. II.18(d)). Therefore, it is not clear if detecting no wood after 40 m from the camera is due to the pixel size issue or in reality no wood passes from this region due to river morphology or the upstream bridge pier.

After measuring the pixel size, it is possible to estimate the uncertainty of the wood length. On the Isère River, most of the wood pieces pass between 40 to 50 m far from the camera where the pixel size is around 0.35 m (Fig. II.18(c)). On the Ain River, most of the wood pieces are detected between 10 to 20 m from the camera where the pixel size is around 0.03 m (Fig. II.18(d)). And the uncertainty on detection of the wood length for most of the woods is $1.5 \times 0.35 \cong 0.5$m on the Isère River and $1.5 \times 0.03 \cong 0.05$m on the Ain. Note that the uncertainty which is 1.5 times pixel size (Eq. (II.1)) is limited to 1 m which is always far smaller than the length dispersion. More discussion about transverse distribution of the woods is presented in chapter III. In the next section a practical example of the transformation from pixel to metric coordinates is presented.

II.2.4.4 An example of orthorectification on site

We present here an example of the transformation matrices and orthorectification for a piece of wood crosses along the river. Figure II.19(a) shows a frame corresponding to the flow deviation for the bankfull discharge. Knowing the vertical distance of the flow from the camera, the corresponding transformation matrices on X, Y directions are estimated and shown in Fig. II.19(b) on X direction and in Fig. II.19(c) on Y direction. On these two figures, each point with i, j coordinates is presented by a color which represents the distance from the camera on X, Y coordinates. Thus, knowing the position of a point on the image (*e.g.* i=400, j=500 on Fig. II.19(a)) the distance of this point to the camera can be transformed to X, Y metric coordinates. Note that these transformation matrices are corresponding to the bankfull elevation.

Using the rectifying transformation matrices of Figs. II.19(b), (c), an example of orthorectification on a detected wood piece at the bankfull level is presented in Fig. II.20.

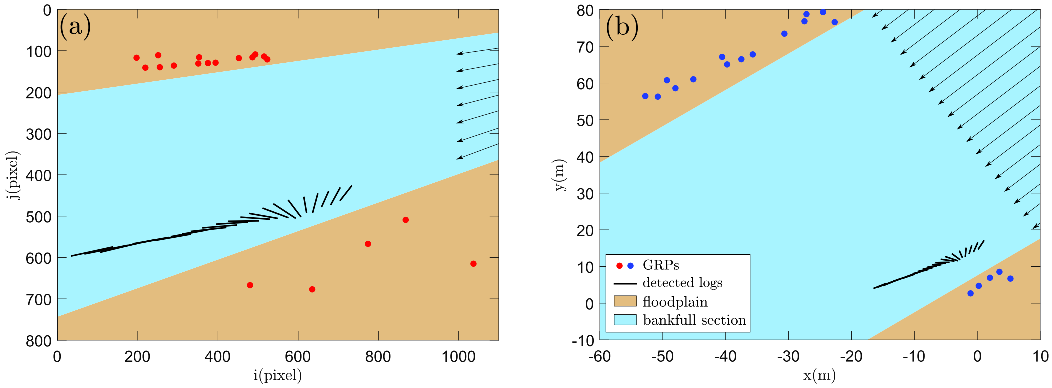

Figure II.20: A practical example of transformation of the coordinates from (i,j) pixel to (x,y) metric coordinates using orthorectification process. Different solid lines represent the successive detection in consecutive frames.

Figure II.20(a) represents the log in pixel and Fig. II.20(b) in metrics. Additionally, the GCPs and the river section at the bankfull stage are presented on both figures. On this figure, the lines are the same piece of wood which is detected on different time steps. Using the transformation matrices the i,j pixel coordinates are transformed to X, Y metric coordinates in Fig. II.20(b). On Fig. II.20(b), the position of the piece of wood is presented in metrics; therefore, knowing that the time difference between each frame is 1 second, the difference between each line (representing the piece of wood) provides the wood velocity in m/s.

II.2.5 sum-up of the technique and associated uncertainties

Direct use of the video, with a manual algorithm, provides the wood fluxes with a precision 90 % due to the operator (10% uncertainty due to the operator bias). In addition to the operator bias, getting away from the camera some smaller woods are not totally detectable by eye. The uncertainty on orthorectification on the Isère River is 0.4 m, which resulted in the uncertainty on the exact position of the wood. A multi-step image processing is necessary to measure wood length with uncertainty of 0.5 m on the Isère River and 0.05 m on the Ain. The other source of uncertainty is the time difference between 2 frames. Based on the field videos, almost in all cases the videos are recorded in 5 Hz, so here we assumed that the uncertainty on time is negligible. Next section is devoted to the results provided by this technique.

II.3 Results

II.3.1 Measured wood fluxes

On the field videos, the first and the most direct characteristic of interest that can be estimated is the number of detected woods and consequently the "wood fluxes" (defined in chapter I.3.1 p. 4). This parameter informs on the occupation of the river surface by wood pieces. Figure II.21 shows the evolution of the wood fluxes defined as the number of detected woods per different time interval (from 15 min on the top to 6 hours on the bottom), during two floods on the Isère River. The gray regions on the figure represent the night time, when there was not any light to detect the wood. The errorbars are the uncertainties of the number of detected woods due to the operator bias, as mentioned in section II.2.5.

As it can be seen on this figure, in both floods, most of the wood is carried by the river during the rising limb of the flood. Moreover, the maximum wood fluxes is observed before the peak of the flood hydrograph. To prepare this graph, we tried to find a tendency between the cumulative wood number and time distance, but due to the high variation of the wood fluxes along time, we did not find any tendency to find the optimum time interval. Plotting the wood fluxes by different time intervals Δt shows that increasing Δt, increases the smoothness of the wood discharge graph. Here, it is seen that for time intervals less than 6 hr, there is always some fluctuations on wood discharge as a function of time, while using the 6 hr time interval, it is possible to detect a nonmonotonic graph with a clean rising and falling limbs. However, large Δt resulted in hiding many fluctuations of the wood fluxes. Note that 2hr is the time interval used the by station to measure water depth and discharge.

As mentioned here, different criteria can be used for selecting the best time interval to measure the wood fluxes. If all fluctuations are needed to be monitored, small time intervals is suggested. Whereas, if the evolution of the wood discharge during a flood is the interested issue, the time interval has to be big enough to show the rising and falling limbs of wood discharge clearly.

II.3.2 Measured wood lengths

Wood length is also of interest as it is linked to the capacity of forming logjams (Yin *et al.* (2003); see also chapter III). Figure II.22 shows the cumulative distribution of the wood lengths on the Isère River (Fig. II.22(a)) during two floods (dark and light blue lines) and the Ain River (Fig. II.22(b)) during the three floods (yellow, orange and red lines). The black dashed line on both figures shows the uncertainty on detected wood length: 0.5 m on the Isère River and 0.05 m on the Ain River (section II.2.5 p. 40). As already mentioned in the introduction, the length between 0.3 to 5 m has been used as length truncation (Comiti *et al.*, 2006; R.A. *et al.*, 2004). Here based on the limitations on detecting wood on the middle of the Isère River and also in order to be able to compare both sites together, 1 m is used as the truncation length, like what has been used in MacVicar & Piégay (2012).

Comparison of length distributions on Figs. II.22(a), (b) shows that while length distribution of the wood is unique in one river for completely different discharges, different distributions are observed in different rivers. In total, the length of the woods observed in the Isère River is higher than in the Ain, so that L_{50} for the Isère and the Ain Rivers are about 2.6 and 1.4 meters respectively, and 99% of the observed lengths in the Isère and the Ain Rivers are less than 14 and 7 meters respectively (See Table

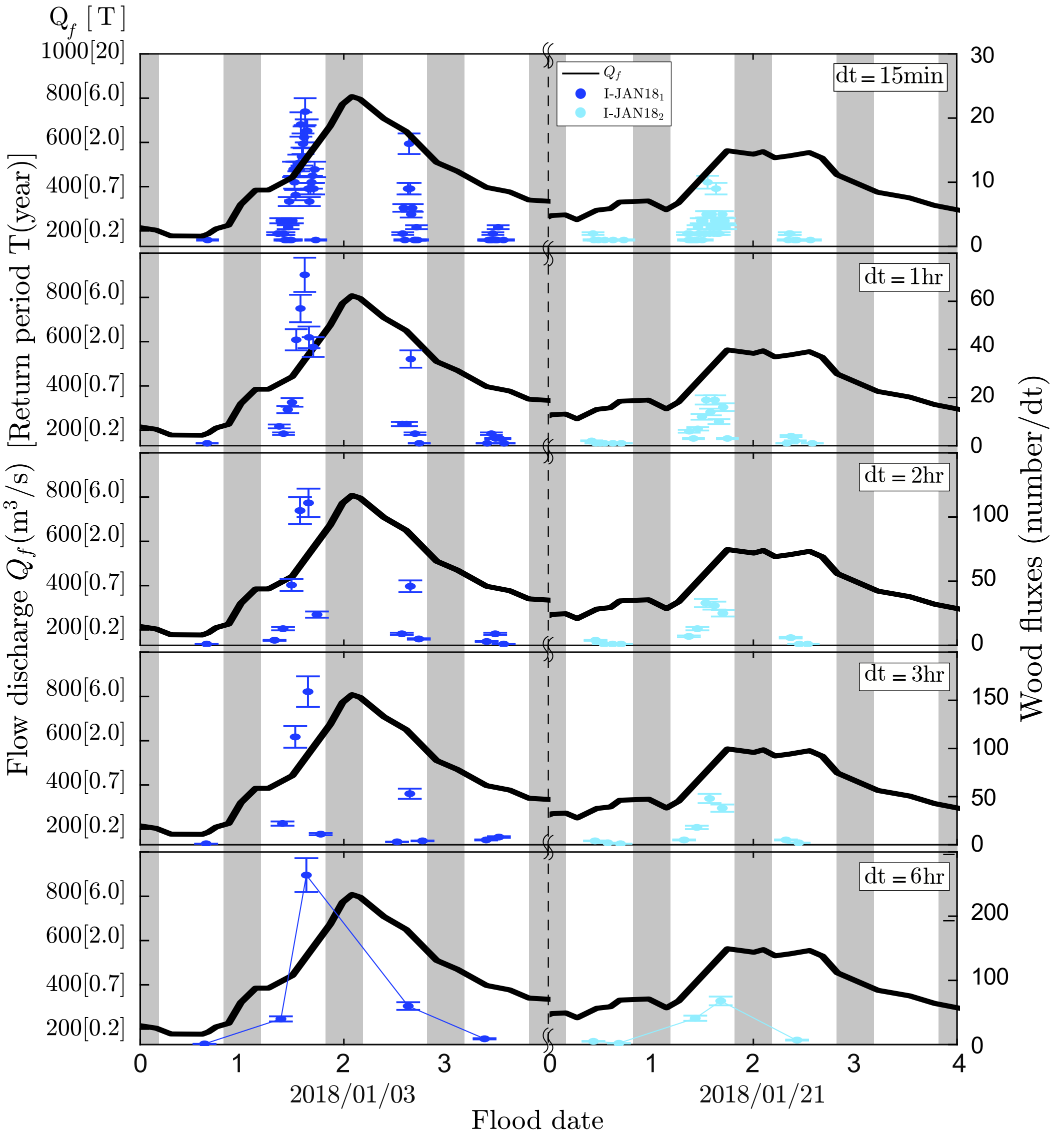

Figure II.21: Evolution of the flow discharge Q_f (m^3/s) (black line) and wood fluxes on the Isère River for two floods, I-JAN18$_1$ (dark blue points) and I-JAN18$_1$ (light blue points) for different time intervals: 15 min, 1hr, 2hr, 3hr and 6hr. The gray regions represent the night time, when there was not any light to detect the wood. Error bars represent the uncertainty due to operator bias on wood detection.

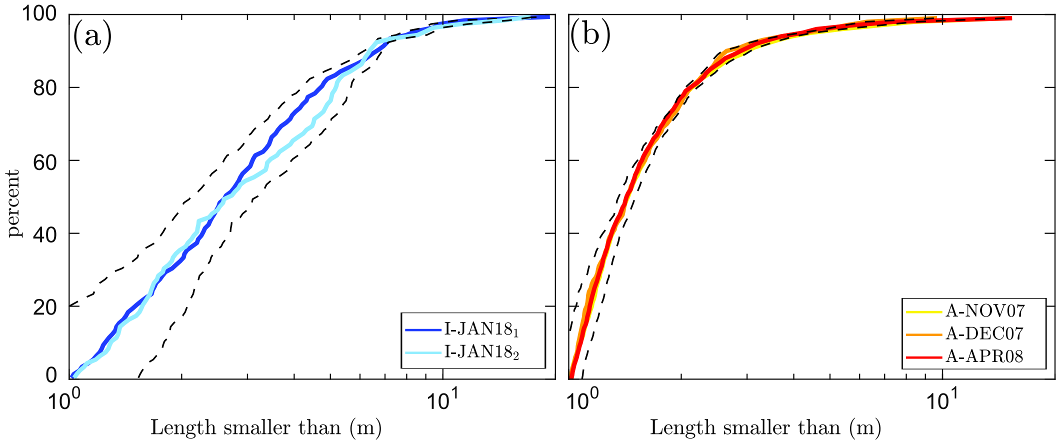

Figure II.22: Distribution of detected wood lengths on (a) the Isère and (b) the Ain Rivers. The black dashed lines represent the range of uncertainty of the wood length.

Table II.5: Typical wood length and volume in five monitored floods

River	**Symbol**	**Number of floats**	**Wood lengths** (m)			**Wood volume** $V(m^3)$		
			L_{50}	L_{75}	L_{99}	**Total**	**rising**	**falling**
Isère	I-JAN18$_1$	380	2.6	4.1	11.4	149	135	14
	I-JAN18$_2$	128	2.6	4.8	14.4	57	56	1
Ain	A-NOV07	671	1.4	1.9	8.3	81	73	7
	A-DEC07	389	1.4	1.9	6.2	31	29	3
	A-APR08	1065	1.4	1.9	7.4	145	130	15

II.5). The fact that woods on the Isère River are typically larger than the Ain River can be due to the natural wood length distribution on the river. The other possibility is related to the transverse position where most of the wood are detected. This position is farer on the Isère River which causes more uncertainty on this river, detecting longer woods there. The perfect superposition of the three flood events on the Ain River rather than some differences on the Isère River is consistent with the fact that on the Ain River the uncertainty on wood length is much smaller than the Isère River and therefore, the detection on the Ain River is more accurate.

In order to estimate the wood length at different flood discharges, the wood distribution at different flood discharges is presented in Fig. II.23(a) on the Isère River and II.23(b) on the Ain River, by 25%, 75% percentile boxplots, for two floods on the Isère River and three floods on the Ain River. For this figure, we use the classical boxplot tool from Matlab. As shown on this figure, the boxplot depicts groups of the wood lengths

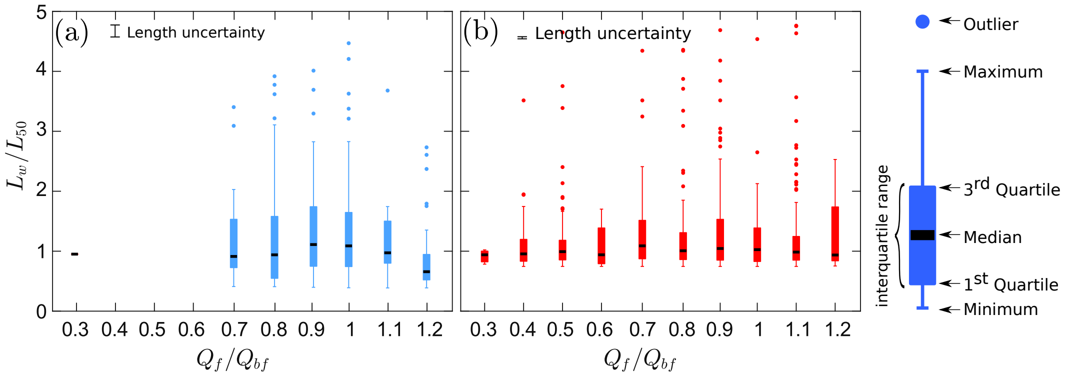

Figure II.23: Length distribution of the wood at different flow discharges (a) on the Isère and (b) on the Ain Rivers. The dimensionless uncertainty on wood length is presented by a black line on top of each figure.

through their quartiles. The interquartile range in the rectangle is the range between first and third quartiles and the black line at the middle is the median of all lengths. Two whiskers with maximum 1.5 interquartile range below and over this rectangles show the statistical minimum and maximums. Points out of the whiskers are thus considered as outliers. In Fig. II.23, a total of 65 outliers are detected, which are only 2% of the data. In order to compare the data in two rivers, with a completely different length distribution, the length of the woods are normalized with the median length in each river ($L_{50} = 2.6m$ for the Isère River and $L_{50} = 1.4m$ for Ain). Additionally, the dimensionless uncertainty on wood length ($0.5/2.6 \cong 0.2$ m on the Isère River and $0.05/1.4 \cong 0.04$ m on the Ain River) is presented by a black line on top of each figure.

It is seen that on both rivers, flood discharge does not affect strongly the wood length distribution, and the distribution of the wood length is almost the same for different flow discharges during one flood. Moreover, there is always the probability to detect a very large woods presented as outlier points here.

As a conclusion, based on Figs. II.22, II.23, the length distribution of the wood during one flood event is totally independent of flood discharge or flood peak value, but is dependent on the river catchment and morphology. The fact that on the Isère River, length distribution for different flood discharges is the same confirmes Piégay *et al.* (2017) results on the Ain River. Though large flood signature can be detected from wood characteristics, on average, wood characteristics do not change much and there is no significant differences between years and tributaries in wood characteristics. Therefore, sampling the distribution of the wood length in one flood can be extrapolated to the other floods, in the bankfull section or overbank floods.

II.3.3 Measuring wood discharge

The most important characteristic of the wood hazard in river is the wood discharge. The wood discharge is estimated by the total volume of wood passing through a certain section during a given time. In the following, first, we describe the relation between wood length and volume that we used to estimate the total volume of the wood. Then, the wood discharge is presented at a flood scale during the rising and falling limbs of the flood hydrograph.

II.3.3.1 Relation between length and volume

Measuring the wood volume is the prerequisite for measuring the wood discharge. The wood volume by itself is a function of the wood geometry (*i.e.* length and diameter and presence of root or branches are needed). The wood length is measured following the orthorectification process. Here we assumed that the wood is a straight cylinder. This assumption is felt to be a reasonable simplification of the wood carried in transport given the dominance of large diameter poplar species in the floodplain, which typically have straight trunks with few large branches (MacVicar & Piégay, 2012). Regarding the diameter, as mentioned in the section II.2.4.2, the uncertainty on wood length on the Ain River is around 10 times smaller than the Isère River. Additionally most of the woods on the Ain River are detected near the camera *i.e.* between 10 to 20 m from the camera. Therefore, it is possible to detect the wood diameter on the Ain River much more accurately.

The total volume of wood is then the sum of the volume of each wood piece, that is

$$V = \pi L \frac{D^2}{4}, \tag{II.2}$$

where L and D are wood length and diameter respectively. This equation requires an accurate measurement of L and D. Figure II.24 shows the relation between wood length and diameter on the Ain River. Note that in the literature, it is common to show the relation between wood length and diameter according to a power law, plotted using logarithmic scale (Niklas, 1995). The red points represent the field observations based on the videos. The black solid line is the power regression which is fitted on the data. The uncertainty due to the pixel size is applied randomly on this data and the power-law is then calculated. Note that the range of 95% confidence bounds on the regression line is very small and it is hardly recognizable in this figure. Moreover, the upper and lower dashed lines represent the range that 75% of all data are located at this range.

After finding the relation between wood length and diameter, the next step is to extract wood volume using Eq. (II.2) based on field detections of L and D.

The total volume which is measured directly from detected lengths and diameters is equal to 282 m^3. The total volume, based on the relation presented on Fig. II.24 is 297 m^3. Therefore, the relation presented here resulted in 5.4 % error on total volume of the wood. Note that as the uncertainty on the Isère River is much larger than on the Ain River and as both rivers are located at the same climatology conditions with same species in riparian zone, we can expect that the relation between wood length and volume is reliable on the Isère River.

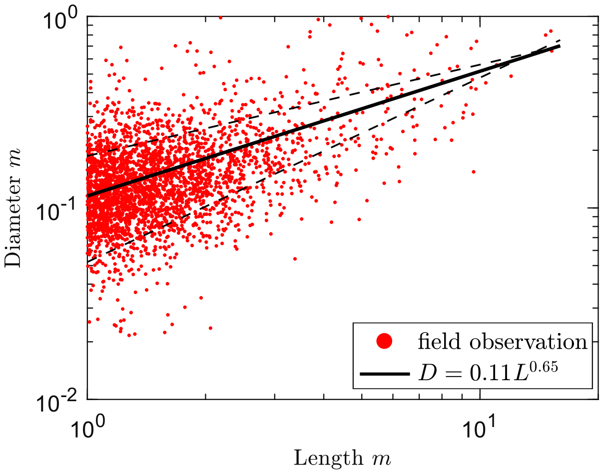

Figure II.24: The relation between wood length and wood diameter on the Ain River, based on videography data. The black solid line is a power regression, representing diameter as a function of length and the dashed lines represent the range that 75% of data are located at this range. Note that a truncation length of 1 m is applied on data.

II.3.3.2 Wood discharge at flood scale during the rising and falling limbs

After calculating the wood volume, as mentioned above, it is possible to correlate flow hydrograph and wood discharge chronicles. Figure II.25 shows the flood hydrograph (black line) and wood discharge on the Isère River for two floods. Gray zones indicate the night period during which no detection is possible. On this figure, similarly as Fig. II.21, the wood discharge is measured by different time intervals. The 0.07 m uncertainty due to the length detection on videos is added to the 10% operator bias uncertainty and is presented by errorbars.

Before these two floods, on Fig. II.25, no significant flood occurs for 1.5 year on the Isère River, since June 2016, when a flood with a return period of 1.5 years occurred. On January 3, 2018, a large flood occurred with a 6.5-year return period (I-JAN18$_1$), resulting in the carrying of 149 m^3 of wood (Fig. II.25, dark blue points). After 2.5 weeks on January 21, another flood with a 1.5 year return period (I-JAN18$_2$) brought up 57 m^3 of the wood downstream (Fig. II.25, light blue points). It is important to remind that monitoring is during daylight hours and all the numbers mentioned are related to the discharge of the wood during the day. Table II.5 shows wood volume in different floods in brie.

As it is observed on Fig. II.25, there is a big difference on wood discharge between rising and falling limbs of one flood hydrograph. In both cases, the transported wood during the rising limbs of the hydrograph are at least one order of magnitude higher than during the falling limbs. Additionally, between two floods close to each other (I-JAN18$_1$ and I-JAN18$_2$), on the second flood rising limb, a much smaller amount of wood is carried away compared to the first one (Table II.5). This difference is normally related

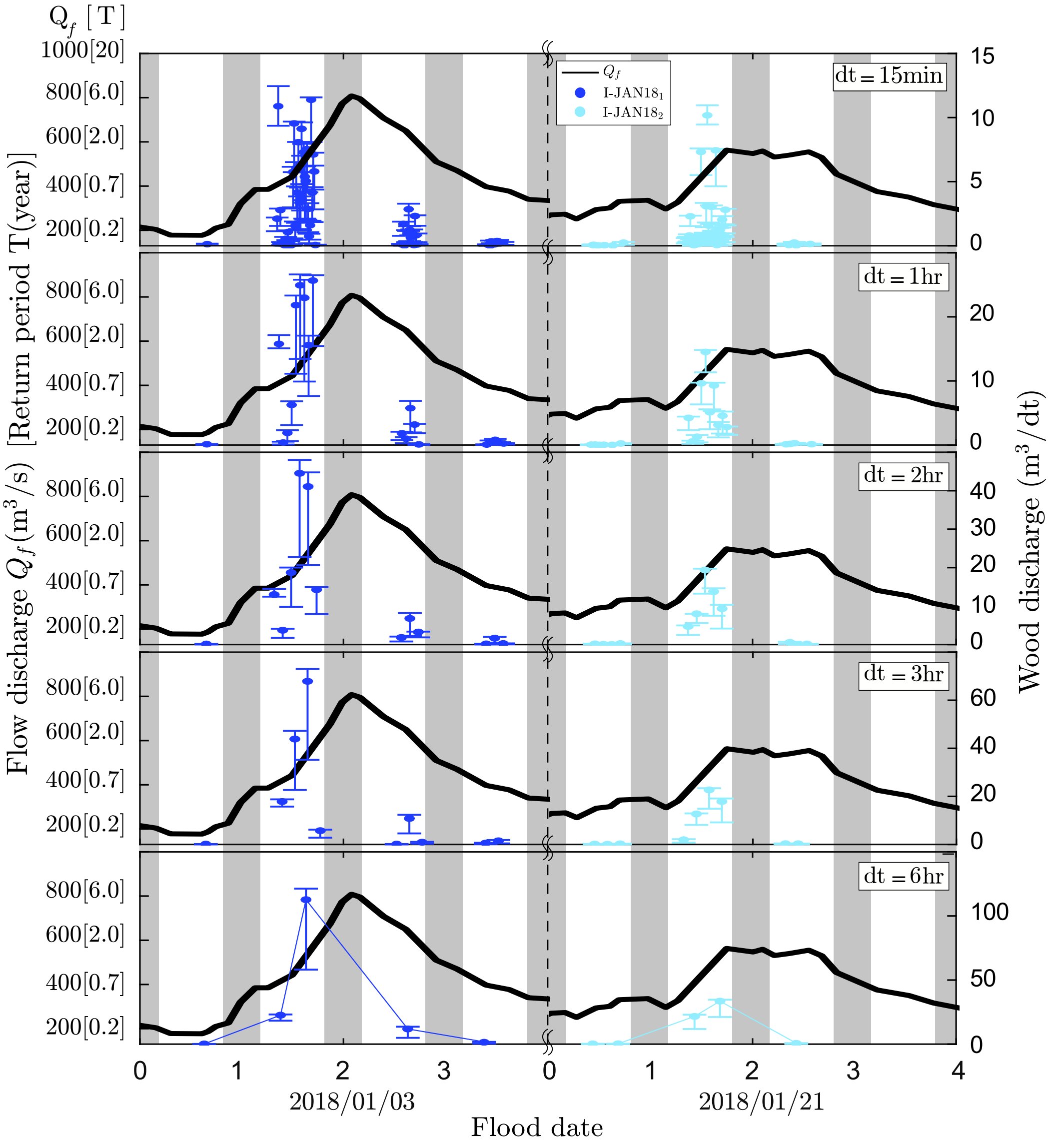

Figure II.25: Evolution of the flow discharge Q_f(m^3/s) (black line) and wood discharge (Q_w m^3/Δt) on the Isère River(dark and light blue points) for different time intervals: from 15min (top) to 6hr (bottom). Errorbars represent the 0.07 m uncertainty due to the length detection on videos and 10% operator bias. Gray zones indicate the night period during which detection is not possible. Values inside brackets on the left vertical axis indicate the return period associated to a peak flow discharge equal to Q_f

to the hysteresis effect (MacVicar & Piégay, 2012).

Comparison between Fig. II.21 and II.25 shows that wood discharge and fluxes follow the same trend. By increasing wood fluxes, wood discharge increases and vice versa. Moreover, like Fig. II.21, on Fig. II.25 larger time interval shows well the global variation of the wood discharge compared to the flood discharge, while small time intervals can present the fluctuations due to the mobilization of separate wood fluxes during one flood. After measuring wood discharge, it is possible to analyze the relation between wood discharge and other parameters such as flood discharge, wood fluxes etc. which is discussed in the next section.

II.4 Discussion

In the wood fluxes study, some quantities are more tedious or difficult to measure. In the hydrological analysis, measuring these complex parameters by easy access parameters is a practical way. Quantifying directly wood discharge in riverine environments is laborious and sometimes dangerous especially during flood events. Additionally, monitoring the wood discharge, as presented here, is associated with some complexities and uncertainties due to detection issues, operator bias, image processing and measuring wood volume. There are also some simple measuring parameters associated with wood, such as the number of the woods, flow discharge and the inter-flood time distance. In the following, the correlation between these simple measurements and wood discharge are discussed.

II.4.1 Correlation between flow and wood discharges

Flood magnitude is an influential parameter on wood transport and storage, as observed when flow discharge Q_f and wood discharge Q_w are compared. In Fig. II.25, in all cases, the maximum discharge of the wood Q_w occurs before the maximum flow discharge Q_f. To illustrates this, Fig. II.26 shows the wood discharge Q_w, normalized with the maximum Q_w in each flood, as a function of the flow discharge normalized by bankfull discharge on the Isère and Ain Rivers for the floods with more than a 1 year return period. The filled and hollow markers represent flow during the rising and falling limbs, respectively. Moreover, the 3 stage model proposed by MacVicar & Piégay (2012) is presented by solid black lines on this figure.

Like what has been observed on the Ain River by MacVicar & Piégay (2012), we observed here that the maximum wood discharge is related to the bankfull discharge. The three stage rating carve for wood discharge is recognizable in Fig. II.26. The difference between this observation and (MacVicar & Piégay, 2012) model is that on the second stage, after wood discharge reaches its maximum value (*i.e.* at bankfull discharge on both rivers), a linear negative trend is detected. To explain this relation between wood and flow discharges, we also take benefit from the conceptual model of Fig. II.27 which is inspired from (Wohl *et al.*, 2018; MacVicar & Piégay, 2012).

Based on Fig. II.26, the first stage of the wood recruitment starts almost from $\frac{Q_f}{Q_{bf}} = 0.5$ and ends at bankfull discharge $\frac{Q_f}{Q_{bf}} \cong 1$. Increasing water level causes the volume

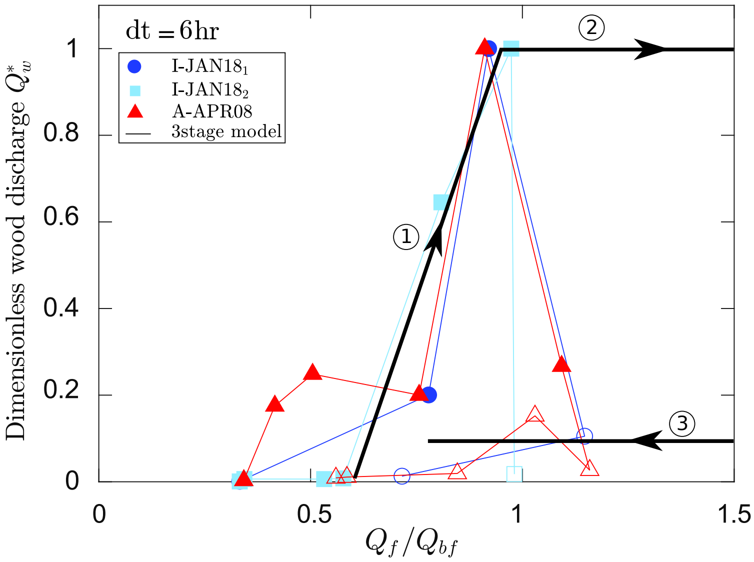

Figure II.26: Wood discharge normalized by maximum wood discharge on the same event as a function of the flow discharge normalized by bankfull discharge on the Isère (dark and light blue markers) and the Ain (red markers) Rivers for the floods with more than 1 year return period. Filled and hollow markers represent data during the rising and falling limbs of the hydrograph respectively.

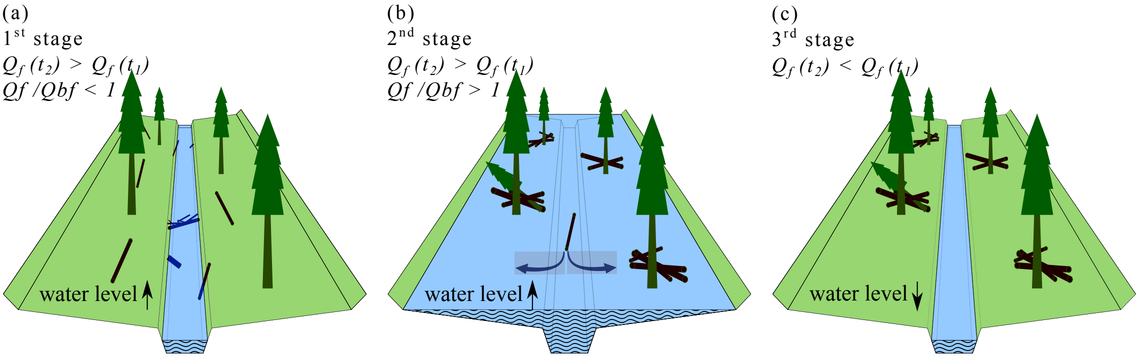

Figure II.27: Conceptual model for the correlation between flow discharge and wood discharge during (a) first stage (b) second stage and (c) third stage of wood motion in a flood event, inspired from (Wohl *et al.*, 2018; MacVicar & Piégay, 2012).

of floating wood increase and river banks are progressively inundated. As it is shown in Fig. II.27(a) at this stage, the majority of the wood results from the mobilization of storage within river (Wohl *et al.*, 2018; MacVicar & Piégay, 2012). Field observations in Fig. II.26 show a nonmonotonic relation between flow and wood discharge, with a maximum point on the bankfull discharge, which is the same on both rivers and for different discharges. This maximum point at Q_{bf} is followed by a second stage with a negative slope for the discharges higher than Q_{bf}. One reason for this decrease in wood discharge at this stage could be related to the floodplain obstacles as discussed by Wohl *et al.* (2018) and schematically presented in Fig. II.27(b). As it is seen in this figure, at this stage, as water levels go on increasing, wood can deposit in some places and not be re-mobilized. Therefore, the negative trend on the second stage in Fig. II.26 can be the result of overbank flow in flood plain. The slope of this stage seems to be a function of the maximum discharge, reminding that our observations are limited to 3 years return periods, beyond that there is no information. Finally, at the third stage of the wood rating curve, wood discharge has negligible values and a small slope decrease. This stage is normally located on the falling limb of flood hydrograph, represented schematically on Fig. II.27. During this stage, when water level decreases, most of the wood pieces within the channel are washed away and the wood pieces in the flood plain get stuck at floodplain obstacles, *e.g.* standing trees in (Fig. II.27(c)). Therefore, the wood discharge decreases significantly at this stage. However, more information would be obtained by monitoring floods with a return period higher than 3 years.

II.4.2 Correlation between flood peak discharge, inter-flood time and total volume of wood

Comparison between the floods on Fig. II.25 and the same figures on the Ain River in (MacVicar & Piégay, 2012) shows that there is a direct relation between the time since last flood and the total volume of the mobilized wood, which means that by increasing time between two successive floods, the volume of transported wood increases. Figure II.28 shows the concurrent effect of time since the last flood and flood magnitude on the volume of mobilized wood. On the Ain River for two floods A-NOV07 and A-DEC07 with almost the same discharge, A-NOV07 with 140 days time since the last flood, recruit 2.5 times more wood than A-DEC07 with two weeks since the previous flood. This can be seen also on the Isère River between I-JAN18$_1$ after 1.5 years and I-JAN18$_2$ after two weeks since the last flood. The total volume of the wood on I-JAN18$_1$ was 3 times more than I-JAN18$_2$. However, on this last case, in addition to the time distance from the last flood, there is the effect of difference in flood discharge. This effect becomes more clear by comparing A-NOV07 and A-APR08 with the same time since the last flood (almost 140 days) but different peak discharges so that Q_{max} A-APR08 was around 2 times bigger than A-NOV07. Therefore, both the time between two floods and flood magnitude play a role on wood mobilization. But to have more clear vision of the effect of these two parameters, more statistics are needed.

Regarding the total volume of wood that is mobilized during a flood, it is observed that for the biggest floods on both rivers (I-JAN18$_1$, A-APR08) almost the same volume

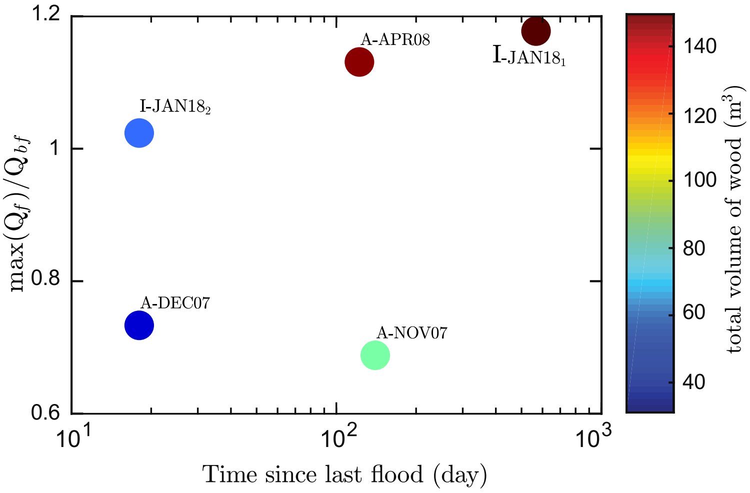

Figure II.28: Total wood volume based on time since the last flood (day) and maximum flood magnitude.

is carried away to the river (Fig. II.28). Assuming woods density between 600 to 900 kg/m^3 (Ruiz-Villanueva *et al.*, 2014*c*), at leading order the same mass of the wood was carried away to the river which has been limited to the order of 10^5 kg. This is consistent with the observations of Seo *et al.* (2008) who reported that at the leading order, the annual export of large wood from the catchment for the basins more that 1000 km^2 area is the same and of the order of 10^5 kg.

II.4.3 Correlation between wood discharge and wood fluxes

Finding the relation between wood fluxes and discharge would be a useful tool to estimate wood discharge. For calculating wood discharge Q_w, a time interval must be chosen so as to provide a realistic view of the wood discharge changes during the flood period. Very short intervals show separate and random observations, while very long time intervals provides only an overview of the whole flood without addressing the details. So the best time interval is the shortest time, for values greater than that the relationship between wood fluxes and wood discharge become independent of time. Figure II.29(a) shows the effect of different time intervals on the relation between wood discharge and wood fluxes. To prepared this figure, first a time interval is chosen. Using this time interval both wood discharge and flux are measured all along the flood for two floods on the Isère River and three floods on the Ain. In the next step, by plotting wood discharge as a function of fluxes, a power regression in the form of $Q_w = a.F^b$, where a, b are constants, is applied on the data. Finally the coefficient of determination R^2 of the power regression is measured and is plotted on Fig. II.29(a) as a function of corresponding time intervals. This process is repeated for different time intervals on the Isère and Ain Rivers and the results are shown in Fig. II.29(a).

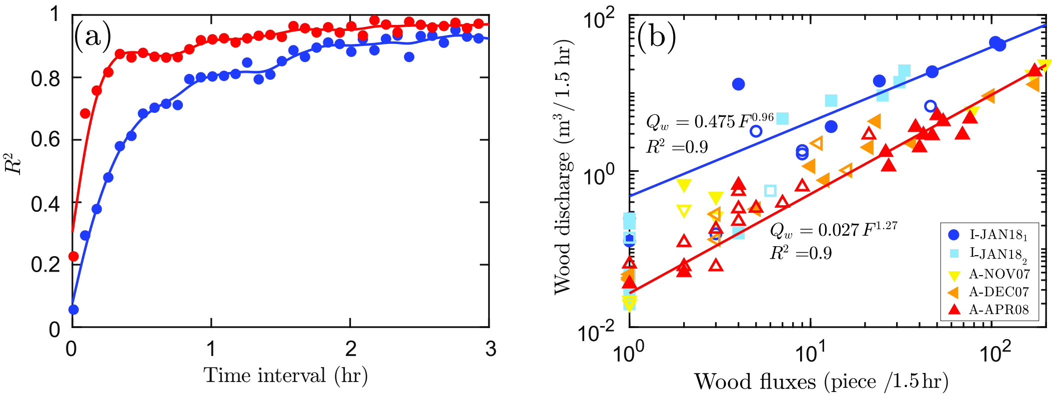

Figure II.29: Wood fluxes (a) Dependency of the coefficient of determination to length of time intervals on the Isère(blue) and Ain(red) Rivers, (b) Wood discharge Q_w as a function of the wood fluxes for both floods on the Isère River (dark and light blue) and three floods on the Ain River (yellow, orange, red) coupled with power regression line for each river.

Based on Fig. II.29(a), on both rivers, by increasing the length of the time interval, R^2 increases. Based on this graph 1.5 hr is a time interval after which R^2 becomes stable and does not change. Fig. II.29(b) shows wood discharge as a function of wood fluxes for 1.5 hr intervals on the Isère (dark and light blue) and the Ain (yellow, orange, red) Rivers. Based on this figure, there is a power law between the fluxes and the discharge of the wood. The relation between wood fluxes and discharge on the same river is unique for different floods, but varies from one river to another. Filled and empty markers represent data during the rising and falling limb of the hydrograph. The positive point of the relation between the fluxes and the discharge of the wood is that it is independent of rising or falling limb of flood hydrograph as is shown in Fig. II.29(b). This relation can provide an estimation of the wood discharge, with a good approximation. It should be noted that more discharges on the Isère River, would be due to the fact that there was an overestimation on the wood length detection on the Isère River, as most of the wood pieces on the Isère River are detected far from the camera while on the Ain River almost all of the wood pieces are detected near the camera.

II.5 Conclusion

This chapter was devoted to the characterization of wood characteristics and transport on field-sites, in rivers. The technique that we made our first choice was the so-called “streamside video monitoring”, which uses images from a fixed camera, located along the river (in this study, on one bank, with no loss of generality).

The different procedures to obtain friendly images – fisheye distortion removing, orthorectification, correlation pixels/field location, etc. – and the manual algorithm to make use of them were assessed and described, along with the corresponding measurement uncertainties. A field campaign, using this technique with a camera located along the Isère River, showed its ability to provide wood fluxes, wood lengths and, with way to appropriate assumptions, wood discharge. Measurement accuracy depends on the camera resolution, but also on its installation (position, inclination, . . .), and good practice of streamside video monitoring will be discussed with more details in the overall conclusions (chapter IV).

The results provided by the video monitoring are valuable to analyze the functioning of the wood-river system. For example, they provide correlations of the wood and river discharges, or of the wood discharge with the different stages of a flood. The results of present study on the Isère River are quite similar with previous ones (MacVicar & Piégay, 2012) on the Ain River, giving confidence to their generalization and gathering five flood events. On both rivers, the maximum wood discharge occurs for the bankfull discharge. In addition, higher wood discharges occur during the rising limb of a hydrograph than during its falling limb. Moreover, results indicate that wood flux, as the easiest detectable parameter on the videos is an appropriate parameter to estimate wood volume at leading order. However, it is important to select an optimum time interval to measure the wood fluxes.

Chapter III

Motion of an individual piece of wood in river

The previous chapter was devoted to the quantifying the amount of wood such as wood fluxes and wood discharge. With a risk assessment point of view, it is however needed to study the motion of single pieces of wood. Therefore, present chapter is more related to the management aspects of driftwood to address the behavior of the wood at local scale to see at a certain point, where does the wood go on the surface, what is the velocity of the wood and how is the interaction of wood and an obstacle. To address these issues, first we represent our observations at the station regarding transverse distribution of the wood and the velocity of the wood at the river surface. Then, theoretical models to reproduce the motion of the wood pieces at the free surface are investigated. Finally the model validity is tested using a well controlled experiments.

Here, chapter III is organized as follow: Section III.1 is dedicated to the field observations of the wood transverse distribution and velocities and the questions about the field observations. Section III.2.1 presents the general equation of motion and a theoretical analysis (on the validity of the tracer model), followed in Section III.2.2 by the experimental setup. Section III.2.3 and III.2.4 present our experimental results in a one-dimensional acceleration flow and in a two-dimensional flow past a cylinder followed finally by the experimental analysis on impact processes in Section III.2.4.4.

III.1 Wood dynamics at the local scale in the field

In chapter II, the video monitoring technique proves its ability to detect the location of a piece of wood in metric coordinates after some post processing procedures. In this section in order to study the dynamics of one single piece of wood on the field, the transverse distribution of number of wood and the longitudinal velocity of wood is characterized on the Ain and the Isère Rivers from the camera located on the river bank.

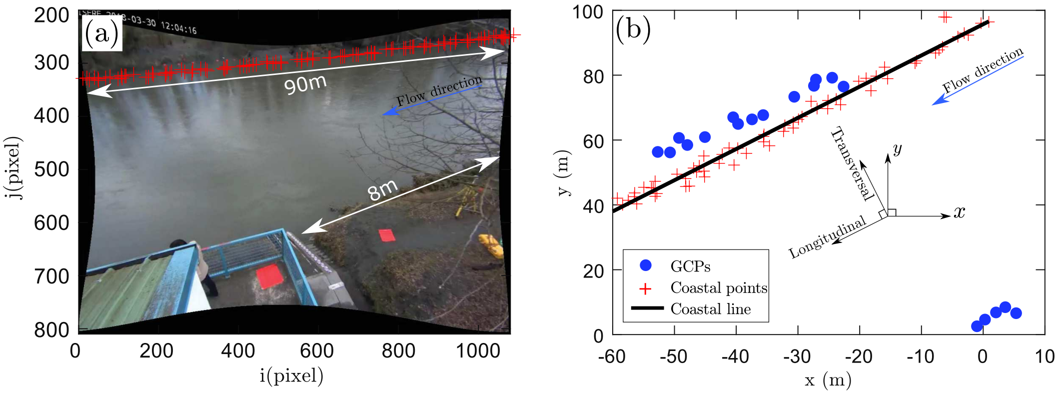

Figure III.1: Local coordinates (a) coastal points detected on a video frame (red markers) and (b) coastal line fitted on coastal points and the local longitudinal and transverse coordinates on the Isère River.

III.1.1 Measurement sites and monitoring technique

To characterize the transverse distribution of pieces of wood and measure the longitudinal velocity of pieces of wood, first, the transverse and longitudinal directions have to be identified. To identify these directions on the Isère River, the coastal line of the river on the right bank is used. As it is shown in Fig. III.1(a), 90 m of this line is detectable on the videos while less than 10 m of river bank is detectable on the left bank. So detecting river direction based on longer coastal line would present a better estimation about the river direction. To detect the coastal line, first, the procedure detailed in chapter II is undergone. The fisheye distortion is removed from the video frames as mentioned in the section II.2.3, p.28. Then the right bank is detected visually using the screen cursor as shown in Fig. III.1(a) by red markers. Afterwards, the coordinates of the points are converted from i, j in pixel to X, Y in metric coordinates using the orthorectification process, mentioned in section II.2.4, p.30, as shown in Fig. III.1(b) by red markers. Finally a straight line is fitted on these coastal points using a least square method. It should be noted that the camera is located on a meander and there is a curvature on the river bank, but the diameter of the meander is large enough (1.5km) to assume the coastal line as a straight line. The local longitudinal and transverse directions are compared with global X, Y directions in the Fig. III.1(b). These flow directions are also presented by a blue arrow on both figures.

On average, each piece of wood was detected 15 times during 15s. Therefore, the longitudinal and transverse positions of the wood and its velocity are the average of these parameters all along the FOV. In the following the transverse distribution of the number and longitudinal velocity of wood pieces are presented. The distributions are measured for the different flood events considered in chapter II: I-JAN18$_1$, I-JAN18$_2$ on the Isère River and A-NOV07, A-DEC07, A-APR08 on the Ain River(see table II.2 p. 20 for more information).

III.1.2 transverse distribution of the number of wood

One of the applications of video monitoring in rivers is the possibility to measure the wood dynamics at the local scale. It is important when it comes to design instream hydraulic structures such as retention structures or bridge piers. In the following the transverse distribution of the number of wood is presented in two cases: the so-called"total distribution" and the distribution as a function of flood discharge.

III.1.2.1 Total distribution

Figure III.2 shows the transverse distribution of wood obtained across the Isère and the Ain Rivers. The horizontal axis represents the distance of the objects from the left bank. This axis is divided in 10 m intervals and the vertical axis shows the number of detected pieces of wood pass in each interval. The side position of the camera is shown on top of each graph. Additionally, to be able to compare transverse distribution with river bathymetry, the river bathymetry is presented on bottom of each figure. Each color in this figure represents one flood.

Figure III.2 includes uncertainties on both vertical and horizontal axes. The uncertainty due to the operator bias based on Fig. II.7, p.27 is 10% on vertical axis. To measure the uncertainty on horizontal axis (distance from the bank), Eq. (II.1) p.35 can be used. Based on this equation, the uncertainty of detecting the location of one object is a function of the number of blurry pixels which are estimated to 3 pixels in our case, of the number of frames where the same piece of wood is detected which on average are 15 frames and of the pixel size. Note that the prefactor 2, in Eq. (II.1) due to the uncertainty on both ends of a wood piece is not applicable here. Therefore, the uncertainty on transverse position of wood is 0.75 times the pixel size. Based on Fig. II.18(c), p. 38 the pixel size on the Isère River varies from 0 to 0.7 m and on the Ain River varies from 0 to 0.5m. As a result, the maximum uncertainty on the position of wood is $0.75 \times 0.7 \cong 0.5$m on the Isère River and is $0.75 \times 0.5 \cong 0.4$m on the Ain. These amount of uncertainty is negligible compare to the river width and is not visible on the figure. Thus, one can conclude that the transverse position of the wood pieces can be estimated with a good accuracy.

Based on Fig. III.2, the transverse distribution of wood number is nonuniform, with a clear decrease on both sides of the peak. The skewness of the wood transverse distribution is different between Ain and Isère Rivers so that most of the wood pieces pass close to the middle of the river on the Isère River, while on the Ain River, a large proportion of the woods pass close to the right bank, near the camera. This skewness is hardly affected by the discharge, in different flood events. Moreover, in the Isère river, far from the camera, no wood is detected. As discussed previously on Fig. II.18 p. 38 this can be due to the pixel size. Far from the camera, at this zone, the size of each pixel is around 0.5m. Therefore, the objects with diameter less than pixel size are not detectable at this region. Based on the fact that most of the woods on the Isère River are much further from camera than the Ain River and getting away from the camera, pixel size increases and smaller objects are not detectable, a fairly underestimation of

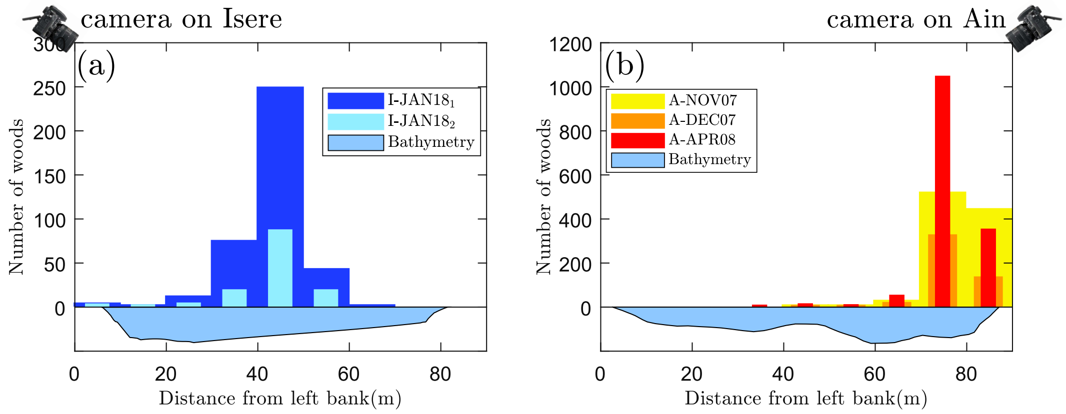

Figure III.2: transverse distribution of the number of woods (a) on the Isère River and (b) on the Ain Rivers during the whole events duration.

the wood number can be expected on the Isère River.

III.1.2.2 transverse distribution as a function of flood discharge

To see clearly the effect of flood discharge on the transverse distribution of the number of woods, Fig.III.3 shows the latter for the largest monitored flood discharge on the Isère River I-JAN18$_1$ (blue bars) and the Ain River A-APR08 (red bars). This transverse distribution is presented both in fraction of wood (Fig.III.3, left vertical axis) and in number of pieces of wood (Fig.III.3, right vertical axis) passing from a cross-section. In the previous chapter it is seen that the bankfull discharge Q_{bf} is a key discharge on wood mobilization. Therefore, here, the flood discharge is categorized based on Q_{bf}.

In Fig.III.3 it is seen that on the Isère River, before $0.5Q_{bf}$ the number of pieces of wood is negligible. One possible explanation can be that the threshold for wood mobilization on the Isère River is slightly higher than $0.5Q_{bf}$ while on the Ain River it is slightly less than $0.5Q_{bf}$. By increasing the flood discharge, it is seen that at the leading order, the position of the maximum wood fluxes is independent of the flood discharge and this position is almost the same for different discharges. However, there is a slight movement toward the camera *i.e.* the outer bank of the meander on both cases which is negligible at leading order. But to have a more obvious idea about this small movement, monitoring larger floods is needed.

III.1.3 Velocity distribution

MacVicar & Piégay (2012) showed that the floating pieces of wood at the surface of the Ain River have the same velocity as the flow surface velocity (see Fig. I.7, p. 15). The video monitoring technique gives access to the wood velocity. Therefore, to generalize this field observation, here, the same measurement is done on the Isère River.

The flow surface velocity fields in longitudinal direction on this river have been

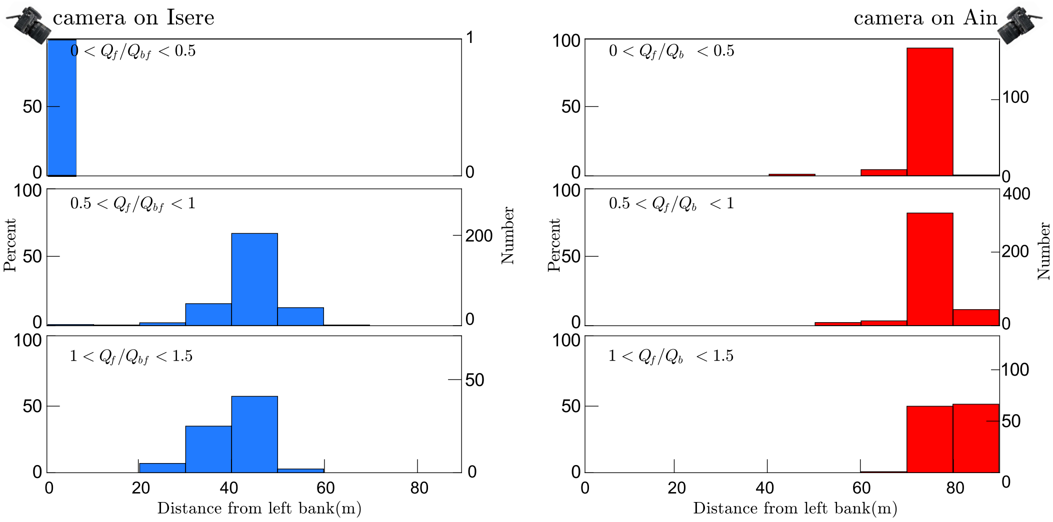

Figure III.3: Transverse distribution of the number of pieces of wood for the largest flood discharge on the Isère River I-JAN18$_1$ (blue bars) and the Ain River A-APR08 (red bars). Left vertical axis presents the fraction of wood and right vertical axis shows number of pieces of wood passing from a cross-section.

measured by Large-Scale Particle Image Velocimetry (LSPIV) by a private company (TENEVIA Co.) for three different flow discharges (Table II.3). Figure III.4 shows these velocity fields for Q_f=678, 500 and 350 m^3/s. The first measurement (Q_f=678 m^3/s) has been done at the same time with the first monitored flood on the Isère River I-JAN18$_1$ in 05/01/2018, the second measurement (Q_f=500 m^3/s) has been coinciding with the second monitored flood on the Isère River I-JAN18$_2$ in 23/01/2018, and the third measurement (Q_f=350 m^3/s) has been done in 24/04/2018. On this figure, the horizontal axis represents the distance from the left bank and the vertical axis is the velocity of the flow and pieces of wood. The corresponding flow discharge is on top left of each graph. The flow longitudinal velocity is presented by the vertical arrows and the longitudinal velocity of each piece of wood is shown by the blue scatters. Note that for each flow discharge the pieces of wood were selected that pass the river at the same flow discharge plus or minus 50m^3/s.

The uncertainty on velocity measurement is presented below the figure. Given that $v = \frac{\Delta l}{\Delta t}$, where Δl is the total distance traveled by the piece of wood during the time Δt, the uncertainty due to the variations of Δl, Δt is $\delta v = \frac{\Delta l \delta t + \Delta t \delta l}{\Delta t^2}$, where δt is the uncertainty on time intervals and δl is the uncertainty on detecting the position of wood on the first and last frames. On the field, the videos are recorded regularly, so it is assumed that δt is negligible, therefore, $\delta v = \frac{\delta l}{\Delta t}$. Assuming that at each time step there is 3 pixels uncertainty on detecting the position of wood (based on Fig. II.16, p. 36) and this uncertainty is applied at the start and end of FOV, totally there is 6 pixels uncertainty on position detection. The pixel size varied between 0 to 0.7 m on the

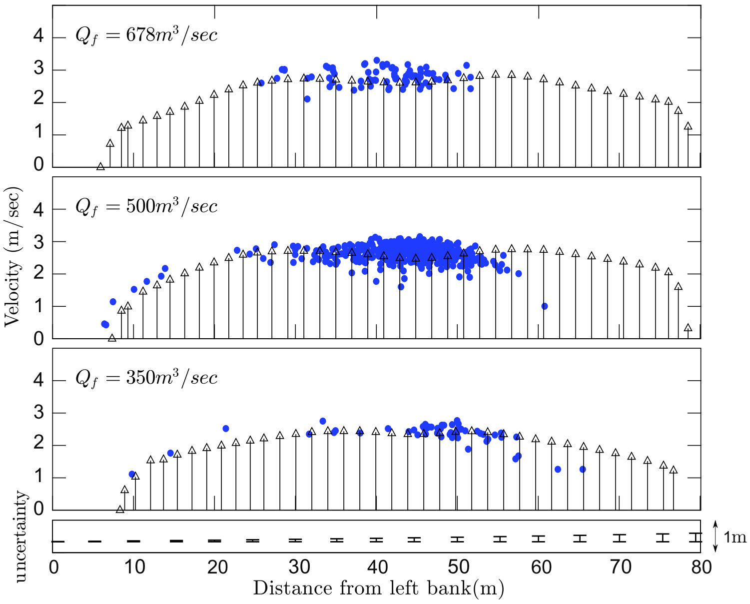

Figure III.4: Comparison between LSPIV data (from TENEVIA Co.) and wood longitudinal velocities. Flow velocity is known based on the LSPIV measurements for three different discharges (350, 500 and 678 m^3/s). Wood longitudinal velocity is measured for all object at the same range of discharge $\pm 50 m^3/s$. By comparing flow and wood velocities, it can be seen that wood has almost the same velocity as flow surface velocity.

Isère River (Fig. II.17(b), p. 37), thus δl varies between 0 to 4.2m. As typically each piece of wood was detected during 15 seconds, $\Delta t = 15s$. Therefore, the uncertainty on the velocity of wood due to the detection errors varies from 0 near the camera to $\delta v = \frac{\delta l}{\Delta t} = \frac{4.2}{15}$ =0.3m/s far from the camera as presented below the Fig. III.4.

Based on Fig. III.4, the velocity of the wood pieces across the section matches correctly with the river surface velocity fields. The velocity gradients of both wood and flow are visible near the left bank of the channel for $Q_w = 350$ and 500 m^3/s. This graph, and a similar graph presented for the Ain River (Fig. I.7, p. 15), both show that wood pieces have the same velocity as the flow surface velocity. There is a slight dispersion on wood velocities that can be due to the vorticity in river. However, from 60 m on transverse section the wood velocity shows much lower values than the flow velocity. It can be due to the higher uncertainty far from the camera or due to the river bathymetry. On the Isère River, the left bank slope (90%) is much steeper than and the right bank slopes (8%). Therefore, by increasing water level, the shallowness effect on the right bank of the river is sensed on larger transverse distance than the left bank. This low side slope on the right bank can result in passing less pieces of wood on the right bank, which is in agreement with Fig. III.2(a).

III.1.4 Discussion

In this section it is observed that in the field, at leading order, the transverse distribution of wood is independent of flow velocity. In addition, on two different rivers, *i.e.* the Isère River (Fig. III.4) and the Ain River (MacVicar & Piégay, 2012) (Fig. I.7, p. 15), wood pieces have the same velocity as the flow surface velocity. This latter result suggest that the wood motion would be known from the flow surface motion. Predicting such motion with reasonable accuracy by numerical computations would be much easier than field measurements. Hence it is necessary to confirm how the wood and flow behaviors are connected. This is done in the next section where theoretical models with numerical solving and well controlled laboratory experiments are presented.

III.2 Interaction between the flow and the pieces of wood

As mentioned in chapter I, to model the trajectory of a piece of wood, two approaches can be implemented: (i)a kinematic approach by assuming the piece of wood as a trace which follows passively flow streamlines, and (ii)a dynamic approach based on Newton's second law and by applying forces exerted by the fluid on the wood. Interestingly the same trajectories in a meandering flow provided in a square Groyne flume were accurately modeled by both kinematic (Ruiz-Villanueva *et al.*, 2014*a*) and dynamic (Persi *et al.*, 2018*a*,*b*) approaches. As it is difficult to compute the whole dynamics of wood, especially in the field where different additional forces such as waves, eddies and wind affect it, estimating the validity of the kinematic approach would significantly simplify the analyses and related computational costs. Thus, in this section, we are going to characterize the dynamics of a piece of wood in a river theoretically and experimentally. A paper has been submitted to the Physical Review Fluids Journal **(H. Ghaffarian, D. Lopez, E. Mignot, N. Riviere, and H. Piegay. "Dynamics of floating objects at high particulate Reynolds numbers")** reproduces the main part of present section.

III.2.1 Theoretical model for floating wood at the river surface

III.2.1.1 Advection equation for a floating object

We present hereafter the theoretical equation describing the advection of a floating object by a flow. Object motion is described in the general case of a nonuniform and unsteady flow by the Basset-Boussinesq-Oseen (BBO) equation for a point object. The complete form of this equation is available both for low particulate Reynolds numbers (Maxey & Riley, 1983) and for large Re_p (Magnaudet & Eames, 2000).

In this study, we focus on the large Re_p case, considering objects floating at a free surface and affecting by the flow surface velocity U_0, reproducing the motion of a piece of wood on the river surface. The condition of buoyancy balance implies that there is no net vertical force on the object and therefore, no vertical motion, and yields an important result that the mass of displaced fluid is equal to the mass of the object. This feature is found similarly in the case of a neutrally buoyant fully immersed particle. Additionally, we focus on the case where there is no lift force, which can occur for instance in a potential flow that has no vorticity and considering objects that are symmetric with respect to the flow. Under these conditions, the advection equation reads

$$m(1+C_A)\frac{d\mathbf{v}}{dt} = m(1+C_A)\frac{D\mathbf{u}}{Dt} + \frac{1}{2}\rho_f C_D S|\mathbf{u}-\mathbf{v}|\left(\mathbf{u}-\mathbf{v}\right), \tag{III.1}$$

where $m = m_p = m_f$ is the mass of the floating object at the free surface (thus that of the displaced fluid), $\mathbf{v}$ and $\mathbf{u}$ the object and fluid velocities, ρ_f the fluid density, C_A and C_D the added mass and drag coefficients, and S the submerged frontal area of the object; $\frac{D}{Dt} = \frac{\partial}{\partial t} + \mathbf{u}.\nabla$ is the convective derivative. Note that Eq. (III.1) is valid for a point object, considering the object size to be much smaller than the typical flow length scale L_0. Since we consider floating objects similar to wood in rivers, their size is much greater than the capillary length, so that capillary effects can be neglected (Singh & Joseph, 2005).

This equation can be written in a dimensionless form using the flow quantities U_0 and L_0 as reference velocity and length scales respectively, so that the reference time scale is L_0/U_0. Denoting nondimensional quantities with *, Eq. (III.1) results in

$$\frac{d\mathbf{v}^\star}{dt^\star} = \frac{D\mathbf{u}^\star}{Dt^\star} + \frac{1}{\lambda^\star}|\mathbf{u}^\star-\mathbf{v}^\star|\left(\mathbf{u}^\star-\mathbf{v}^\star\right), \tag{III.2}$$

where

$$\lambda^\star = \frac{\lambda}{L_0} = \left(\frac{2(1+C_A)}{C_D}\frac{V_f}{S}\right)\frac{1}{L_0}, \tag{III.3}$$

V_f being the displaced fluid volume (or equivalently the object submerged volume). In Eq. (III.2), the left hand side is the object dimensionless acceleration, and the right hand side the dimensionless fluid forces.

The first term on the right hand side of Eq. (III.2), namely $\frac{D\mathbf{u}^\star}{Dt^\star}$, referred to as the undisturbed flow force, is due to viscous stresses and pressure gradients existing within the base flow (Corrsin & Lumley, 1956). It is interesting to note that in the present problem of floating objects, the prefactor of the dimensionless undisturbed flow force is exactly 1, as it is the case for fully immersed neutrally buoyant particles.

The second term on the right hand side of Eq. (III.2) is the dimensionless drag force, scaled by $1/\lambda^\star$, where $\lambda^\star$ is a ratio between a length scale λ based on the object characteristics and the flow length scale L_0. This expression of the drag force is always valid, considering that the drag coefficient is a function of the Re_p as shown in Fig. III.5. On this figure, the drag coefficient C_D is presented as a function of Re_p for a spherical object as the most basic geometry among the literature, and for disk and cylindrical geometries that are used in our study. Note that C_A can also vary with Re_p but with a much weaker sensitivity, so that the influence of the $1+C_A$ term in Eq. (III.3) does not play a significant role at leading order.

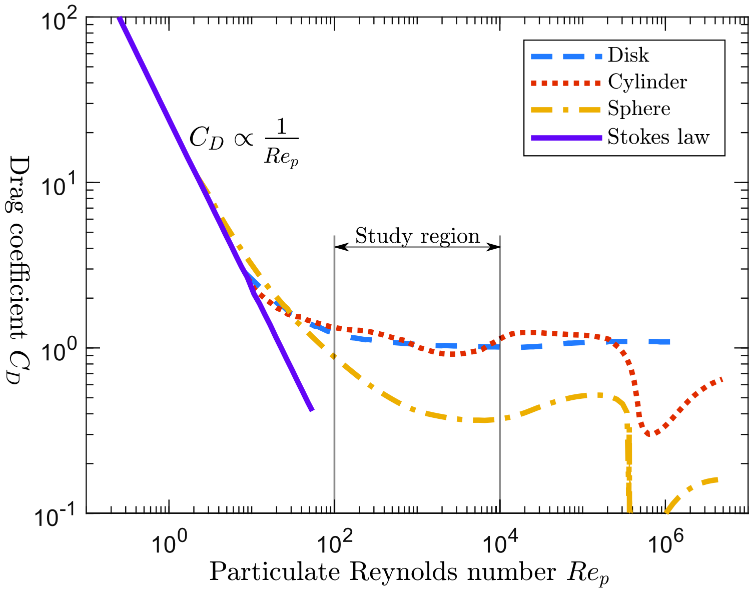

Figure III.5: Drag coefficient C_D as a function of Re_p (Hoerner, 1965)

III.2.1.2 Analogy between $\lambda^\star$ at large Re_p and Stokes number at low Re_p

To describe the link between Stokes number St and $\lambda^\star$, we can write the nondimensional drag force expression based on Eq. (III.2) as;

$$F_D^\star = \frac{1}{\lambda^\star}|\mathbf{u}^\star - \mathbf{v}^\star|\left(\mathbf{u}^\star - \mathbf{v}^\star\right), \tag{III.4}$$

This expression is valid for all values of Re_p, but can be simplified at low Re_p, since in that case the drag coefficient is inversely proportional to Re_p (Fig. III.5, Stokes law). Table III.1 summarizes the expressions of C_D, $\lambda^\star$ and $F_D^\star$ in the small and high Re_p limits for a disk as the simplest geometry on this case due to its symmetry on the surface. In that case, $Re_p = |\mathbf{v} - \mathbf{u}|D/\nu$, where D is the diameter of the disk and ν is water kinematic viscosity, and $V_f/S \propto D$, so that the low Re_p expressions result in the well-known Stokes drag, (Maxey & Riley, 1983; Bergougnoux *et al.*, 2014) with

$$St \propto \frac{(1 + C_A)D^2}{\nu}\frac{U_0}{L_0} = \frac{T_p}{T_0}, \tag{III.5}$$

where T_p is the object viscous response time and $T_0 = L_0/U_0$ the flow time scale.

As a results, at low Re_p the drag force is linear with the relative velocity and scaled by the inverse of a time-scale ratio known as the Stokes number, and at large Re_p the drag force is quadratic and scaled by the inverse of a length-scale ratio noted $\lambda^\star$.

At large Re_p however (typically $Re_p > 10^2$), the specificity is that the drag coefficient C_D is almost independent of the Re_p(Hoerner, 1965; Gonçalves *et al.*, 2015) as shown in Fig. III.5. In that case $\lambda^\star$ is a fixed ratio between an object-based scale λ and the

Table III.1: Drag force expressions in the low and large Re_p limits.

	$Re_p \ll 1$	$Re_p \gg 1$
$C_D \propto$	$\dfrac{1}{Re_p} = \dfrac{\nu}{D\lvert\mathbf{u}-\mathbf{v}\rvert}$	Cst
$\lambda^\star =$	$St\lvert\mathbf{u}^\star-\mathbf{v}^\star\rvert$	Cst
$F_D^\star =$	$\dfrac{1}{St}\left(\mathbf{u}^\star-\mathbf{v}^\star\right)$	$\dfrac{1}{\lambda^\star}\lvert\mathbf{u}^\star-\mathbf{v}^\star\rvert\left(\mathbf{u}^\star-\mathbf{v}^\star\right)$

flow length scale L_0. One can thus provide an interpretation for $\lambda^\star$ by analogy with the Stokes number, considering λ as the object characteristic response distance, scaling the distance traveled by the object while adapting to the flow. Moreover, since C_D and C_A are both of order 1 for such objects when $Re_p \gg 1$ (Batchelor & Batchelor, 1967; Bush & Eames, 1998), we get from Eq. (III.3) that λ should be proportional to the ratio between the object submerged volume V_f and submerged frontal area S. As a result, λ is expected to scale as the length of the object in the direction of the flow, noted L_x in the following.

III.2.1.3 Asymptotic analysis on $\lambda^\star$

The scaling of the dimensionless drag force by $\lambda^\star$ can provide some insights on a floating object dynamics in the $\lambda^\star \ll 1$ and $\lambda^\star \gg 1$ asymptotic regimes. The case where $\lambda^\star \ll 1$ results in $\mathbf{v}^\star \approx \mathbf{u}^\star$ almost immediately, as the object drag force and therefore, acceleration cannot tend to infinity. On the other hand, when $\lambda^\star \gg 1$ the drag force becomes negligible compared to the undisturbed flow force. Since Eq. (III.2) is valid only for point objects for which, object dimensions are much smaller than the flow dimension L_0, this case actually corresponds to $C_D \ll 1$. Due to the pre-factor 1 before the undisturbed flow force term, the resulting equation is $d\mathbf{v}^\star/dt^\star = D\mathbf{u}^\star/Dt^\star$. This yields an interesting result which is that for an object with $m_p = m_f$ (either floating or neutrally buoyant), if at a given time $\mathbf{v}^\star = \mathbf{u}^\star$, then for any subsequent time $\mathbf{v}^\star = \mathbf{u}^\star$. Note However,that $\lambda^\star \gg 1$ implies that the object acceleration will occur on extremely long distances compared to the flow scale.

This asymptotic analysis suggests therefore, as soon as $\mathbf{v}^\star = \mathbf{u}^\star$ the point object model predicts a tracer behavior regardless of $\lambda^\star$ (or equivalently the Stokes number at low Re_p). This is consistent with the field observations in Figs. I.7, p. 15 and III.4 where wood has the same velocity as flow. We thus address two questions in this section to validate this analysis. First, is λ a suitable length scale for the acceleration of a piece of wood in river as a large Reynolds number floating object under flow? and, if so, is it proportional to the object streamwise length L_x? Second, if initially $\mathbf{v}^\star = \mathbf{u}^\star$, will the object be a tracer regardless of $\lambda^\star$, *i.e.* will $\mathbf{v}^\star$ be equal to $\mathbf{u}^\star$ at all times? To address these questions, we designed two sets of experiments described in the next section.

III.2.2 Experimental facilities and measuring devices

In the previous section, we introduced a coefficient in the nondimensional drag force named as $\lambda^\star$ that scales the acceleration length of a floating object. We perform two sets of experiments in an open flume with different floating objects: (i) object acceleration from rest in a uniform flow and (ii) object motion in a nonuniform flow, considering a flow passing around a cylinder to check the validity of the statements that are mentioned in the previous section. In this section the experimental facilities and measuring devices are presented.

III.2.2.1 Flume

The experiments are carried out in a straight, rectangular, 6 m long, 0.8 m wide, glass walled flume that was designed and built during the first year of the PhD project. Fig. III.6 shows the schematic design of the experimental setup and the different parts described as follow.

A centrifugal pump (1) immersed in an underground sump provides the discharge in an upstream tank. The flow discharge is measured with an electromagnetic flow-meter (2) (Promag 50, from Endress-Hauser) with an uncertainty of 0.05 L/s. In order to homogenize the flow, water enter to the upstream tank through a perforated pipe (3), at the bottom of the upstream tank in Fig. III.6. A PVC plate (4) is located upside the perforated pipe to prevent vorticity mixing at the top. The water enters to the top of the entrance tank through a layer of chicken wire (5). Then to tranquilize, straighten and homogenize the flow, perforated plates (6), a honeycomb (7) and, finally, a buffer made of several layers of chicken wire (8), located in the upstream converging part of the flume (9), made of a PVC plate. The channel entrance corresponds to the end of this converging part. The 6 m channel consists of three glass made, 2 m reaches which are attached to each other. At the end of the channel, a crest weir (10) adjustable from 0 to 50 cm controls the water depth. The top of this weir is made of a thin metallic blade to minimize the backwater effect and to prevent from clogging. The channel slope is adjustable by changing the height of a vertical bar (11) located at the middle of the channel.

III.2.2.2 Flow

As mentioned in the previous section the flow passes through different steps to be tranquil, straight and homogeneous. In this study, the range of discharge is 16 to 19 L/s and of water depth is 105 to 115 mm, corresponding to hydraulic diameter based Reynolds numbers in the range 65000 to 75000, and Froude number around 0.1. The flow is steady, turbulent and sub-critical. Water depths are measured using a point-gauge with an uncertainty of about 1 mm.

In addition Table III.2 shows the typical range of flow surface velocity U_0 m/s, particulate Reynolds and Froude numbers Re_p, Fr_p and flow Reynolds and Froude numbers Re_f, Fr_f in some similar studies. Note that Re_p, Fr_p are measured based on object

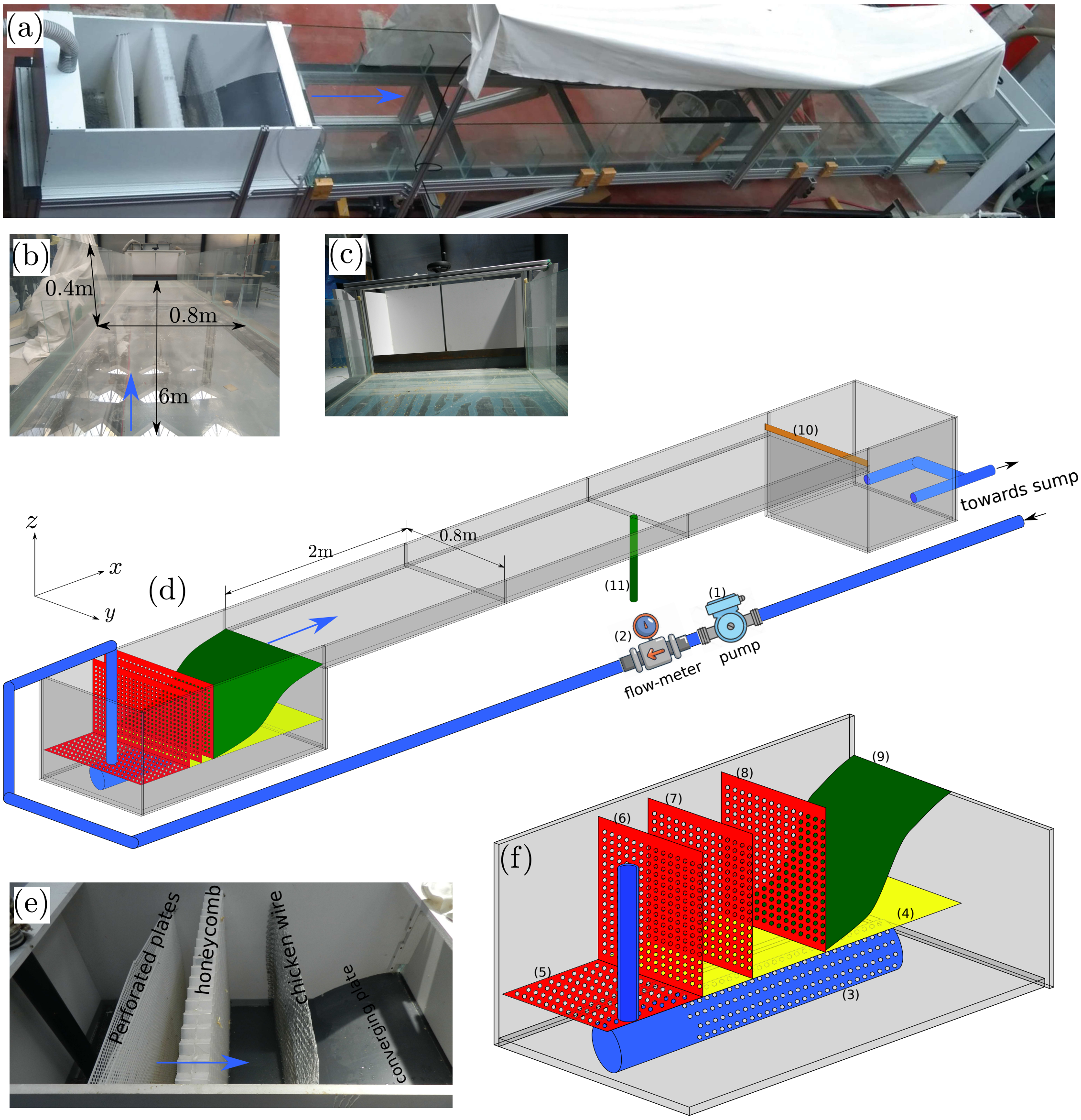

Figure III.6: Schematic view of the experimental set-up (not at scale). (a) photograph, (b) details of the section, (c) downstream adjustable sharp crest weir, (d) general sketch and details of the tranquilizer devises: (e) photo and (f) sketch.

Table III.2: Typical Froude and Reynolds numbers in the similar studies

U_0 m/s	Fr_p	Re_p	Fr_f	Re_f		Reference
1.60	0.98	4E+05	0.28	5E+06	field	Haga *et al.* (2002)
0.50∼0.80	0.50∼0.81	5E+04∼8E+04	0.13∼0.20	1E+06∼8E+05	field	Ruiz-Villanueva *et al.* (2016)
0.03∼0.37	0.04∼0.48	2E+03∼2E+04	0.02∼0.24	6E+03∼9E+04	lab	Beschta (1983)
0.21∼0.38	0.59∼1.06	3E+03∼5E+03	0.31∼0.44	3E+04∼9E+03	lab	Cherry & Beschta (1989)
0.20∼0.28	0.25∼0.35	1E+04∼2E+04	0.13∼0.15	1E+04∼4E+05	lab	Beebe (2000)
1.44∼2.24	0.98∼1.53	3E+05∼5E+05	0.35∼0.54	2E+06∼4E+06	lab	C.V. *et al.* (2005); Alonso *et al.* (2009)
0.09	0.18∼0.25	1E+03∼2E+03	0.04	5E+04	lab	Young & Davies (1991)
0.44	0.71∼1.00	2E+04∼9E+03	0.29	1E+05	lab	Braudrick *et al.* (1997)
0.45	0.74∼0.91	1E+04∼2E+04	0.38	7E+04	lab	Braudrick & Grant (2000, 2001)
0.66	0.67∼1.22	2E+04∼7E+04	0.35	2E+05	lab	Bocchiola *et al.* (2006)
0.76	1.25∼1.54	2E+04∼3E+04	0.51	2E+05	lab	Wilcox & Wohl (2006)
0.07	0.16	1E+03	0.05	2E+04	lab	P.W. *et al.* (2001)
0.21	0.49	4E+03	0.08	2E+05	lab	Wallerstein *et al.* (2002)

diameter and Re_f, Fr_f are measured based on flow hydraulic diameter. As it is seen in this table, the flow Reynolds number in the experiments is in the range of 10^4 to 10^5 and Froude number of flow is typically around 0.1 to 0.3. On the field the Froude number is at the same order but Reynolds number is one order of magnitude larger than the experiments.

To test the homogeneity of the velocity three tests were implemented: (i) micro-propeller velocity measurement to check the 3D velocity profiles, (ii) Surface particle image velocimetry (SPIV) to check the surface velocity fields at the field of view (FOV) and (iii) Particle tracking velocimetry (PTV) to check the reproducibility of the same flow characteristics in different tests.

III.2.2.2.1 Developed flow

The aim of measuring flow 3D velocity fields is to check the flow development after upstream convergence along the channel to find the best position for installing the camera. Propeller flow meters use the mechanical energy of the fluid to rotate a rotor in the flow stream. Blades on the rotor are angled to transform energy from the flow stream into rotational energy. The rotor shaft spins on bearings. When the fluid moves faster, the rotor spins proportionally faster and the propeller flow meter measures the velocity of fluid in the flow. Propeller meters are accurate and relatively inexpensive and can be economical even when only needed for a short time. Micro-propeller is made to sense the small Reynolds number flows at which the propeller does not operate well.

Figure III.7 shows the results of measurements by micro-propeller on longitudinal (Fig. III.7(a)) and on transverse (Fig. III.7(b)) sections. In section (a), the measurements are performed at three different depths, and 17 different longitudinal sections, resulting in totally 51 measured points. In section (b), the measurement are performed at four different depths, and 7 different transverse sections, resulting in 28 measured points. The measurement locations are presented by black dotes on each section. At each point first the micro-propeller was fixed at a stable point. Then the flow velocity is recorded during 10s and the average velocity on this time is recorded. This process was repeated 10 times at each point and the final velocity at each point is the average of all 10 measurements.

Based on Fig. III.7(a), at the channel entrance where $0 < X < 20\%$, the surface velocity is affected by the entrance convergence and a positive acceleration is visible at the surface. The surface velocity is stabilized at the middle of the channel between 20 to 70%. Approaching the outlet location, due to the presence of the weir, the surface velocity first decelerates at $70 < X < 95\%$ and then accelerates rapidly at $95 < X < 100\%$. Based on this figure the longitudinal section that flow is well developed is between 20 to 70%. Therefore, this section would be the best longitudinal section for the experiments. Between this section at the middle of the channel the section (b) is measured in transverse direction. Based on Fig. III.7(b) at this section, near the walls the flow is affected by the friction of the walls, while between 20 to 80% the flow is uniform.

As a consequence our field of view (FOV) is from 50 to 60% of the longitudinal section (between 3 to 3.6m) and from 20 to 80% of the transverse section (between 0.15 to 0.65m) as it is shown in the Fig. III.8. At this section flow is fully developed. Note that in the first set of experiments, the flow is uniform (without obstacle) and the floats are released at the start of the FOV to record their accelerated movement. The obstacle (orange cylinder) is installed only for second experiment: "motion in a nonuniform flow" and the floats are released at the start of the channel 3 m upstream of the FOV.

III.2.2.2.2 Homogeneity of velocity fields

After finding the best longitudinal and transverse position for data recording, in continue, to control the homogeneity of surface velocity fields on x-y plain the SPIV technique is implemented. Surface particle image velocimetry (SPIV) is a non-intrusive approach to measure velocities at the free surface of a water body. The raw SPIV results are instantaneous water surface velocity fields, spanning flow areas up to hundreds of square meters (Muste *et al.*, 2008).

Small sawdust particles with typically 2 mm length were used as tracers. Figure III.9(a) shows an example of the SPIV measurement. The obstacle is highlighted by a white half circle and the sawdust tracers are visible on this figure. Additionally the surface flow velocity fields are presented in Fig. III.9(b). For preparing this figure 2000 frames were used. It is seen that the flow surface velocity fields are well homogenized and are symmetric around the obstacle. Based on the SPIV measurements U_0 in our measurements is typically 20 cm/s. It should be noted that the capillary effect is visible on Fig. III.9(a) between tracers. Knowing that the capillary length is of the order of 1 mm and the velocity is of the order of 10 cm, this effect is negligible in majority of FOV. Just near the obstacle where the velocity decreases, this effect is visible.

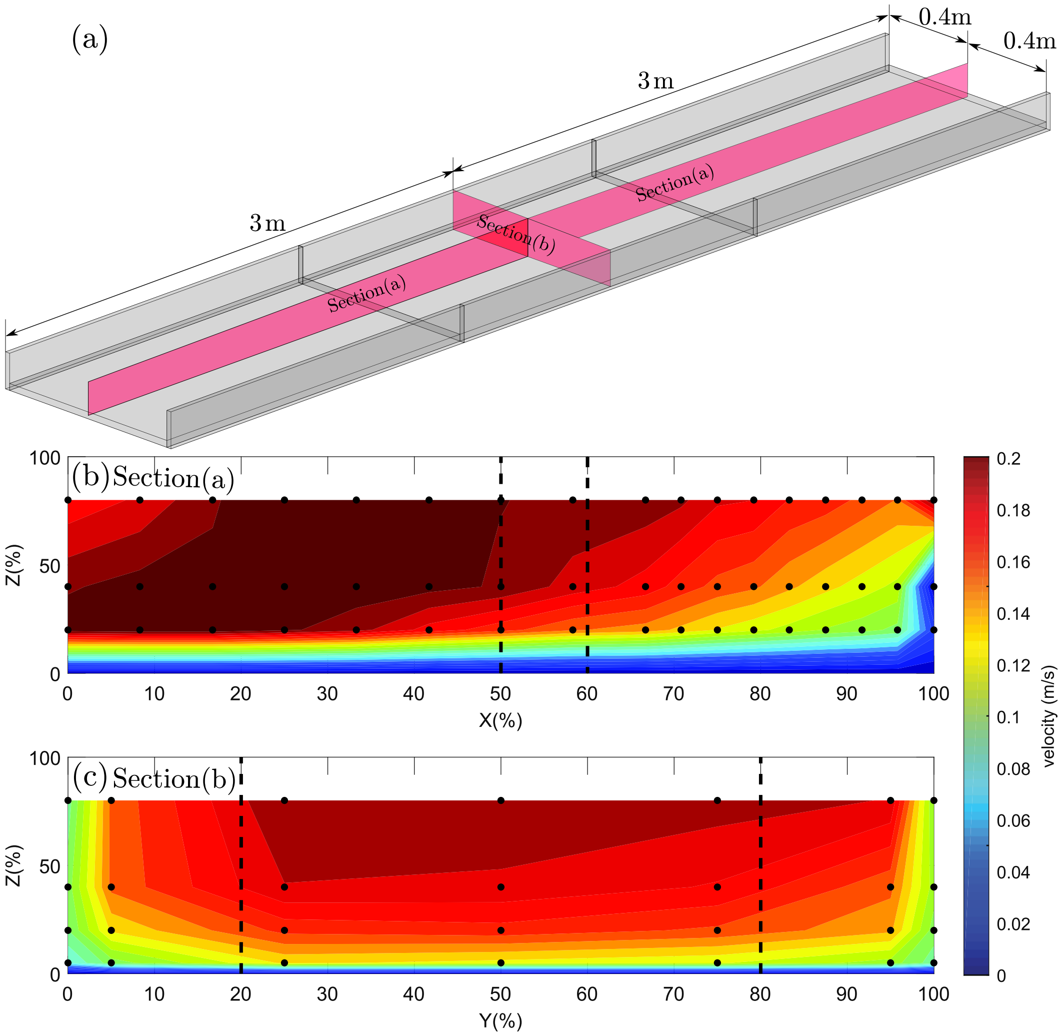

Figure III.7: Flow velocity measurement in 3D flow using micro-propeller. (a) Sketch of the position of the measured sections, (b) section a in streamwise direction and (c) section b in lateral direction. Black dots are the measured points and dashed lines limit the field of view.

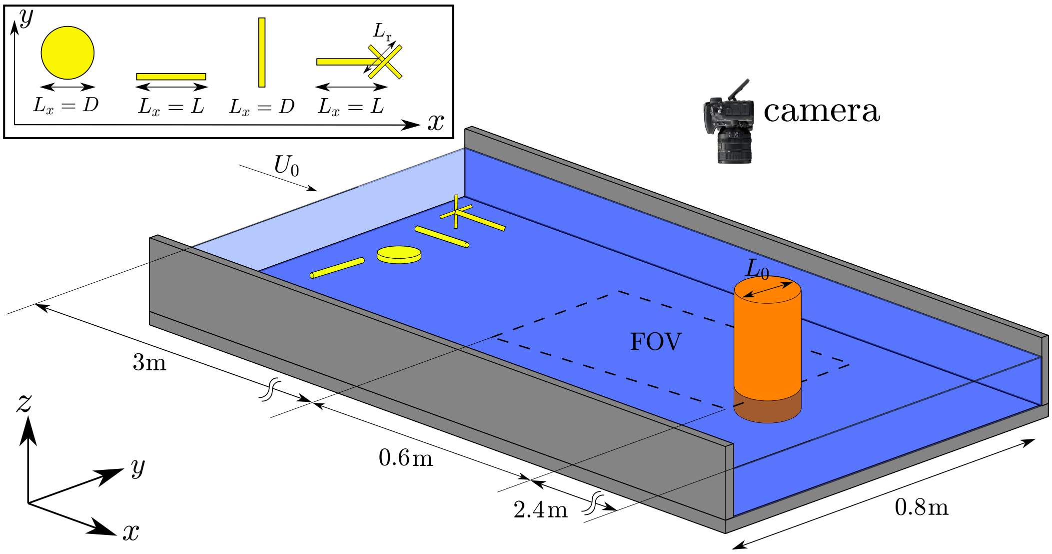

Figure III.8: Schematic view of the experimental setup at the field of view. Note that the obstacle (orange cylinder) is installed only for second experiment: "motion in a nonuniform flow"

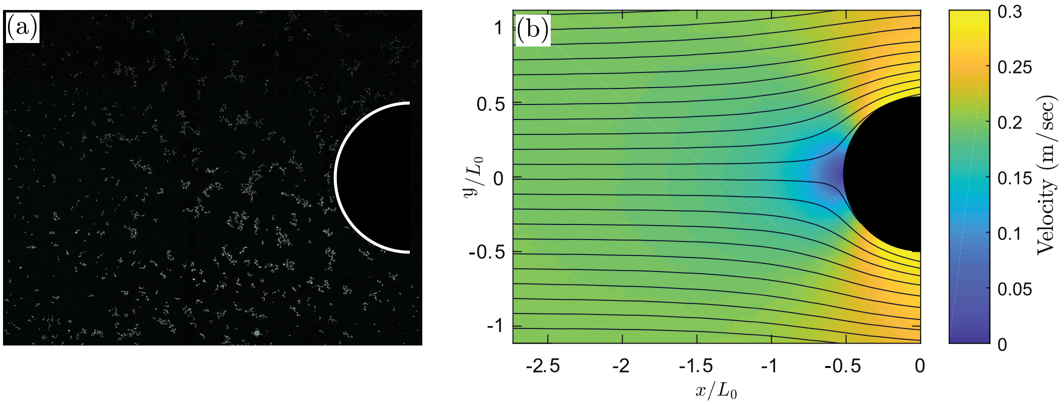

Figure III.9: SPIV technique to control the homogeneity of surface velocity fields. (a) an example of the recorded raw frames and (b) the post treated data based on 2000 frames.

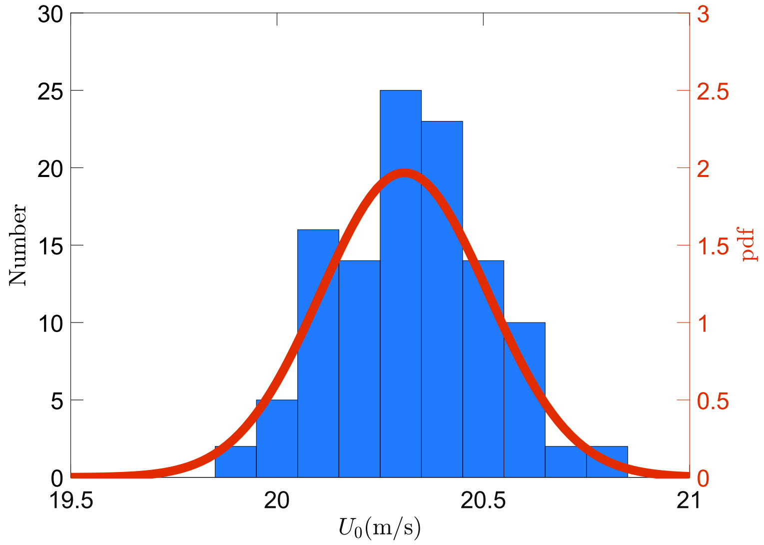

Figure III.10: PTV velocity measurement to control the reproducibility of the flow characteristics with the same experimental configuration.

III.2.2.2.3 Reproducibility of the flow characteristics

After finding the best position of the channel for measurements and checking the homogeneity of flow velocity fields, in the next step the reproducibility of the flow characteristics with the same experimental configuration is controlled by Particle tracking velocimetry (PTV) technique. The aim of this test was to verify if U_0 is constant when measured in different times but without changing the configuration of the instruments such as pomp, valves or weir. PTV is a velocimetry technique to measure velocity of particles that are resident in a fluid (Maas *et al.*, 1993; Malik *et al.*, 1993). As the name suggests, individual particles are tracked, so this technique is a Lagrangian approach. Details of object detection is presented in section III.2.2.4.

Totally 113 tests were done during different times, but with the same experimental configuration. Figure III.10 shows the result of these measurements. The horizontal axis shows the measured velocities, the left vertical axis show the number of tests corresponding to an specific surface velocity and the right vertical axis shows the normal probability distribution function (pdf) of the tests. In probability theory, the normal or Gaussian distribution is a very common continuous probability distribution. A random variable with a Gaussian distribution is said to be normally distributed and is called a normal deviate. As it is seen the dispersion of velocity measurements are normally distributed with the mean value of 20.3 cm/s and standard deviation of 0.2 cm/s. Thus, we can expect that the velocity measurements are reproducible with 1% relative error.

To summarize this section, the middle of the channel is used for FOV because at this section flow is fully developed, homogeneous, symmetric and reproducible. In the next section we talk about the particles that are used in the experiments.

III.2.2.3 Floats

The aim of this work is to study the dynamics of single pieces of wood in a river. The wood geometry on the field contains many complexities. Thus, in order to establish our experimental methodology, the tests were started from the simplest geometries to more complex one.

III.2.2.3.1 Characteristics

Three categories of floating particles with increasing complexity are tested in the experiments: (i) paraffin disks (ii) wooden simple logs and (iii) wooden logs with different types rootwad. Figure III.11 presents all floating objects used in this study.

The first category consists in paraffin disks (relative density $\rho_p/\rho_f = 0.88$) with fixed height ($L_z = 1cm$) and different diameters (Fig. III.11(a)). A first advantage presented by a disk is its isotropy, so that the orientation with respect to the flow does not affect its dynamics. Secondly, a disc with small height will minimize the effect of vertical velocity profile, the particle will be only subjected to the surface velocity of the flow. Finally, the contact angle between paraffin and water is close to 90 degrees which reduces the effect of surface tension on the particle movement as the disks border are vertical at the free surface.

The second category of floating particles are simple cylindrical wooden logs (relative density $\rho_p/\rho_f = 0.64$), without roots (Fig. III.11(b)), which mimic floating wood in rivers. The simple cylindrical wooden logs released both aligned with flow and perpendicular to the flow.

The third and most complex geometry used in these experiments are the logs with roots that are tested in four different configurations: (i)logs with different length of artificial roots (same number) (Fig. III.11(c)), (ii)logs with different number of artificial roots of the same length (Fig. III.11(d)), (iii)logs with a circle at one side as artificial rootwad with different diameters (Fig. III.11(e)) and (iv)three different natural logs with root (Fig. III.11(f)).

To be able to compare different categories of rooted logs, the root frontal area S_{root} is measured and presented in Table III.3. Frontal area of the rooted logs is measured based on the length and diameter of the roots. Only in the case of the natural logs, using a photo of the log frontal area (Fig. III.12), the number of pixels were counted and then based on the size of the pixels the frontal area was measured.

The objects characteristics are given in Table III.3, with D and L as diameter and length of the objects, and Re_p based on the diameter and minimum slip velocities, $Re_p = |\mathbf{v} - \mathbf{u}|D/\nu$, with ν the fluid kinematic viscosity. Additionally, the typical particulate Reynolds and Froude numbers in some similar studies are presented in Table III.2. Most floats are large enough to neglect the capillary effect, as the capillary length is of the order of 1 mm, so only the smallest objects might be affected, but no clear effect was observed. Note in particular that the contact angle with paraffin is close to 90°, so that even for the smallest disks the capillary forces are expected to remain negligible.

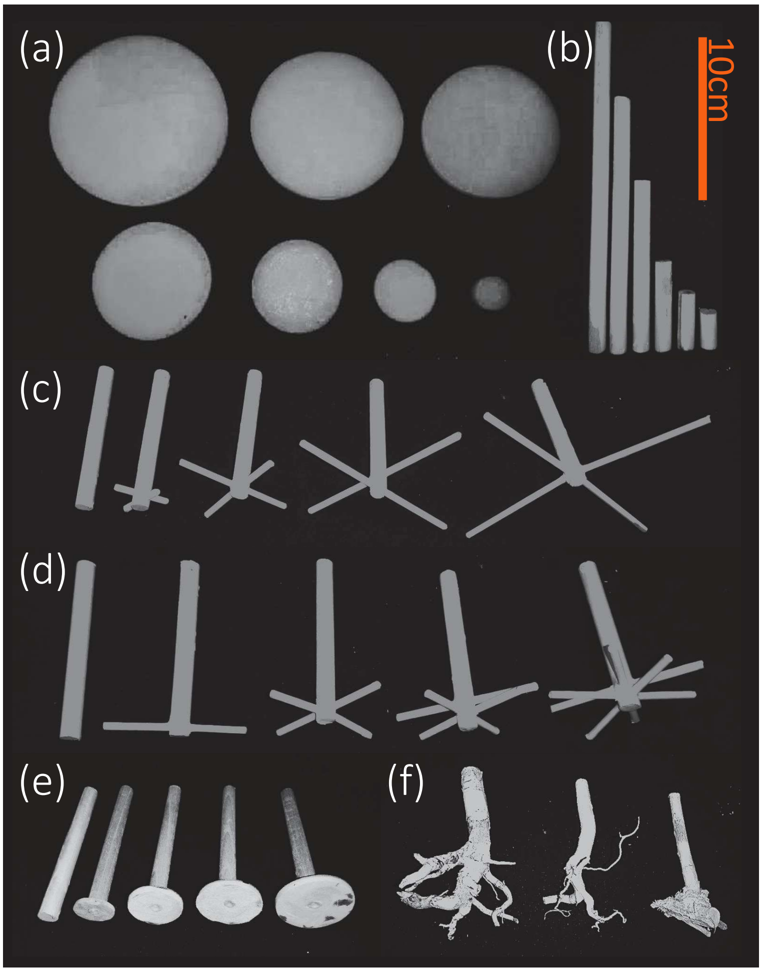

Figure III.11: Floating objects used in the experiments. (a) Paraffin disks with different diameters, (b)wooden logs with different lengths, (c) logs with different root lengths, (d) logs with different root numbers, (e) circle ended logs, (f) natural rooted logs

Figure III.12: Measuring frontal area of natural logs. Image size is 12Mpixel.

Table III.3: Characteristics of the floating objects used in the experiments

	D(cm)	L(cm)	Root				Re_p	ρ_p/ρ_f
			number	length L_r	diameter	$S_{root}(cm^2)$		
Disks(paraffin)	2 to 10	1	-	-	-	-	400 to 10^4	0.88
logs(wood)	1	1 to 20	-	-	-	-	200 to 10^4	0.64
logs with root(wood)							700 to 10^4	0.64
Varied root number	1	10	0 to 4	7.5	-	0.8 to 11.3		
Varied root length	1	10	2	0 to 15	-	0.8 to 11.9		
Varied circle diameter	1	10	-	-	0 to 4	0.8 to 11.3		
Natural logs	1 to 2	10 to 12	-	-	-	10 to 23		

Figure III.13: Raw materials used for the preparation of the floating objects.

III.2.2.3.2 Preparation

Except the natural logs, all floating objects are prepared in the laboratory. To prepare the paraffin disks, the candle wax was melt into the fiberglass molds as it is seen on the top of the Fig III.13. For preparing the logs two size of wooden dowel rods were used, the 1 cm diameter was used for the trunk and the 4 mm one was used as the roots. For the simple logs, the 1 cm log was cut in different lengths. For the rooted logs, first the 1 cm log was cut in 10 cm length as the trunk. Then by piercing the end of the trunk, the 4 mm stick passes through the hole and was attached by wood glue to the trunk as the root.

III.2.2.3.3 Releasing the objects

For releasing the objects into the flow different methods were implemented. For example: (i) dropping down the objects by a conveyor causes some vertical waves. (ii) Putting the object between two vertical blades and releasing object by increasing the distance between the blades. With this method if the blades do not open at the same time an additional transverse motion is imposed to the object. (iii) Fitting the object by a thin

Figure III.14: JAI GO-5000M camera with LM25HC lens used to record data.

rope to a fixed point and releasing the object by burning the rope. Firstly, this method was time consuming and secondly when the object attached to the rope, it starts to oscillate due to the waves around the object. Therefore, we decided to release the objects by hand. Releasing the objects by hand is much faster than the other methods, so we could have many iterations to have a good statistics. However like the second method, sometimes in addition to the streamwise motion objects have some lateral movement. These objects could be removed easily in the post processing.

It should be noted that the control on the object is lost as soon as it starts moving. Sufficiently big logs (longer than 3 cm) keep their initial orientation throughout their trajectory; it is not the case for smaller objects whose orientation is random due to experimental noise.

III.2.2.4 Object detection process

III.2.2.4.1 Data recording

The object trajectories are recorded using a high spatial resolution camera JAI GO-5000M with up to 62 Hz frame rate at full 5-megapixel resolution (2560 × 2048). A LM25HC lens with 1 inch main sensor size and 25 mm focal length is mounted on the camera. This lens provides manual adjustment of focal length, iris and focus. Figure III.14 shows both camera and the lens. The camera is located above the flume, perpendicular to the flow, 3.3 m downstream from the channel entrance, with a 60cm ×50cm field of view (FOV) as shown in Fig. III.8.

The data are recorded on a PC DELL PRECISION 3630 P400 with 32GB additional RAM to be able to record longer duration of videos. Pixel binning is a clocking scheme used to combine the charge collected by several adjacent CCD pixels, and is designed to reduce noise and improve the signal-to-noise ratio and frame rate of digital cameras. On both i, j directions, pixel binning of 2 is used, so the image resolution is 1280×1024. In the first set of experiments, as our interest is the accelerated motion of the object, the frame rate of 60 Hz is used to be able to monitor the motion of the floats accurately at the first seconds of the motion. In the second set of experiments, the main objective is to

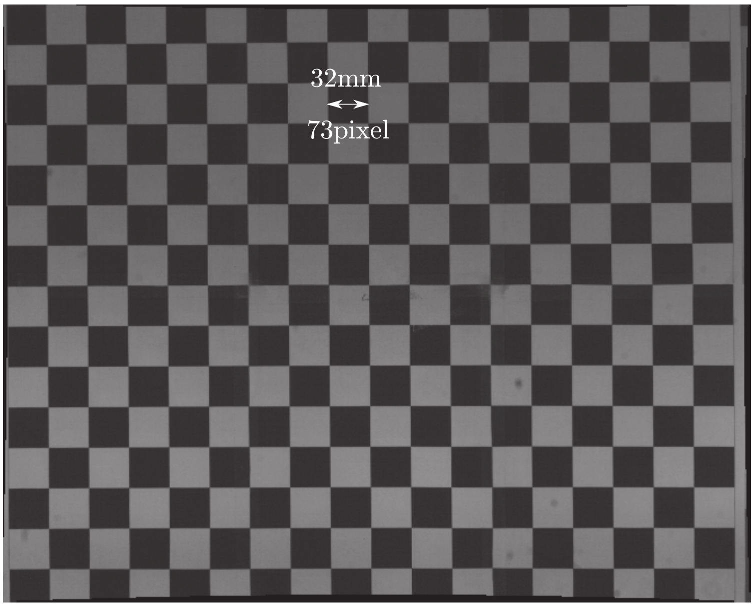

Figure III.15: Fisheye correction and measuring pixel size.

track the float and detect if objects hit the obstacle or not, therefore, to be able to have more iterations in longer videos, the frame rate of 30 Hz is used. TIFF monochrome 8 bit/pixel size of each 1280 × 1024pixel image is 1.31 MB. With 32Gb Ram, it is possible to record around 25,000 frames. Therefore, the duration of each test in the first set of experiments is around 7 min and in the second set of experiments is around 14 min. During this time the objects one by one released into the flow and their motion was recorded. After recording the motion of the floats, the next step is to correct the distortions on the image.

III.2.2.4.2 Correcting fisheye lens distortion and measuring pixel size.

As mentioned in the previous chapter fisheye lens distortion causes panoramic or hemispherical image. The process of correcting this distortion is described in the section II.2.3, p.28. Figure III.15 shows the field of view after correcting fisheye lens distortion. Based on this figure, given that the focal length of lens is large (25 mm) the fisheye lens distortion is small. As camera is located perpendicular to the FOV, after correcting fisheye distortion, the lines on the chessboard becomes perfectly straight and therefore, the orthorectification process is not needed.

As it is seen in Fig. III.15 each square on the chessboard is 32 mm. On this figure, the size of each square is around 73 pixels. Therefore, each pixel corresponds to 0.44 mm.

III.2.2.4.3 Object detection

After being sure that the distortions on the images are corrected, in the following due to

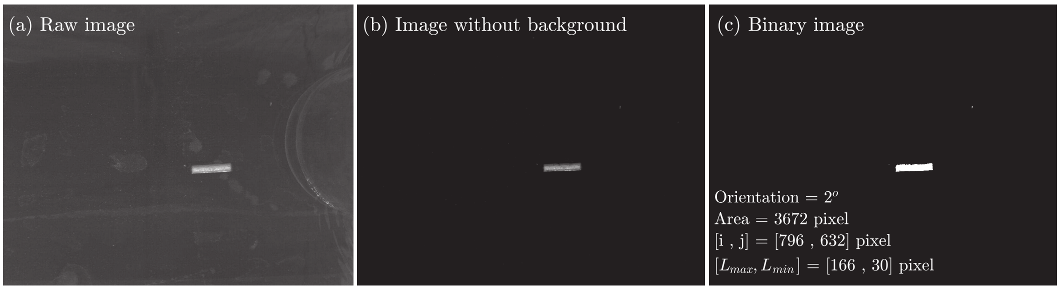

Figure III.16: Detecting an object in a frame using the command “regionprops” in Matlab R2017a®. (a) Raw image. (b) Image without background. (c) Binary image

the large amount of frames (25,000 frame at each test and hundreds of tests) a process has to be established to detect the objects automatically. The time evolution of the object position is determined using a standard image detection algorithm using Matlab R2017a®. Here the process to detect an object on a frame is described.

Each frame contains an object in a fixed background. Figure III.16(a) shows a raw image. In this image the wooden log is at the middle of the frame, the obstacle is at the right hand side of the image and the bottom of the channel is visible in dark gray. Except the wooden log, the rest of the image are identical in all frames. Therefore, the first step is to extract this background from the image, like Fig. III.16(b). To do so, the only step is to record one frame without any floating object and subtract it from the rest of the frames with floating object. Note that as illumination conditions were constant enough, an average of all images background was not needed. The next step is to convert the image without background to a binary image. The binary image is a matrix contain only 0 as black and 1 as white colors. To prepare the binary image, first a threshold has to be introduced. Then, on the frame the values less than this threshold are considered as zero and the values more than that will be one. The threshold is a value between 0 and 1. It has to be large enough to remove the unwanted areas throughout the image and small enough to not remove the floating object. The binary image is shown in Fig. III.16(c). On this figure, the threshold is equal to 0.3.

After preparing the binary image the command “regionprops” in Matlab R2017a® measures a set of properties for each connected component (object) in the binary image. The properties provided by this command is presented in the Fig. III.16(c). As it is seen on this figure, the command “regionprops” detects some properties of the detected region: (i) the area of the region as the actual number of pixels in the region, returned as a scalar. (ii) The center of mass of the region (presented in i, j), returned as a 1-by-2 vector. The first element of this vector is the horizontal coordinate (or i-coordinate) of the center of mass and the second element is its vertical coordinate (or j-coordinate). (iii) The maximum and minimum length (in pixels) of the major and minor axis of the ellipse that has the same normalized second central moments as the region, returned as a scalar. (iv) The orientation of the region as the angle between the horizontal axis and the major axis of the ellipse that has the same second-moments as the region, returned

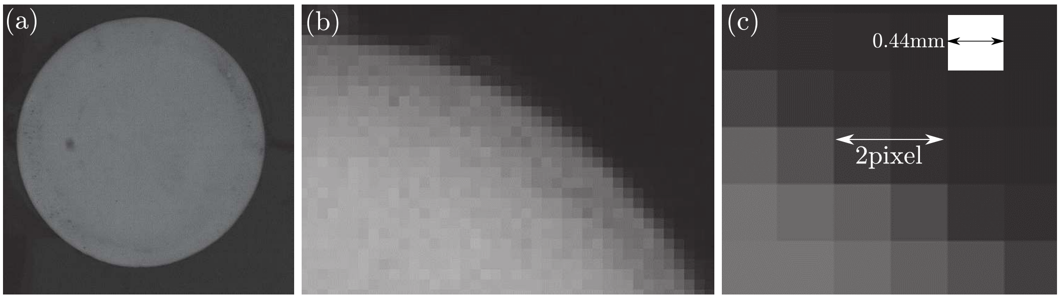

Figure III.17: Uncertainty due to the lack of clarity in pixels

as a scalar. The value is in degrees, ranging from -90 degrees to 90 degrees. Moreover the extreme points of the object is detected by this command which are not presented here. In many cases, the command “regionprops” detects more than one object in one frame. But after extracting the background and applying the threshold unless the interested region all other whit regions will be too small. For example, in Fig. III.16(c), apart from the floating object which is visible on this figure, three other regions are detected by the “regionprops” with areas around 10 pixels which are not visible. Therefore, only the largest region is recorded and the rest will be removed. This process is repeated on consecutive frames to extract the object trajectory along the FOV.

III.2.2.4.4 Uncertainties

As it is seen in Fig. III.17 the uncertainty due to the lack of clarity in pixels is about 2 pixels which is equal to 0.88 mm and is of the order of 1 mm. Assuming that the object movement during the time Δt is equal to Δl the uncertainty due to the object detection on velocity is equal to $\delta v = \frac{\Delta t \delta l + \Delta l \delta t}{\Delta t^2}$, where δt and δl are the uncertainties on time and position. Assuming that the $\delta t = 0$ due to the precision of the camera $\delta v = \frac{\delta l}{\Delta t}$. In the same way the uncertainty due to the lack of clarity in pixels on the acceleration is $\delta a = \frac{\delta v}{\Delta t} = \frac{\delta l}{\Delta t^2}$. Therefore, using the frame rate of 60 Hz increases significantly the uncertainty of acceleration. Knowing that δl=0.88 mm, between each frame δv=53 mm/s and δa=3200 mm/s^2.

Our fitting process is based on the trajectory of the object. Knowing that the object is typically detected in 200 frames and at each frame δl=0.88 mm, the total uncertainty is $0.88/\sqrt{200} \cong 0.06$ mm which is negligible compared to the size of the objects and the object displacement between two consecutive images. Therefore, it is possible to use the trajectory of object to measure λ as it is described in section III.2.3.

III.2.2.4.5 Object trajectory

After detecting the position of an object in a series of the frames, knowing the size of each pixel from section III.2.2.4.2 it is possible to transform the position of the object from pixel to metric coordinates. Figure III.18(a) shows the trajectory of four different objects as a function of time. The errorbars represent the uncertainty in detection due to the

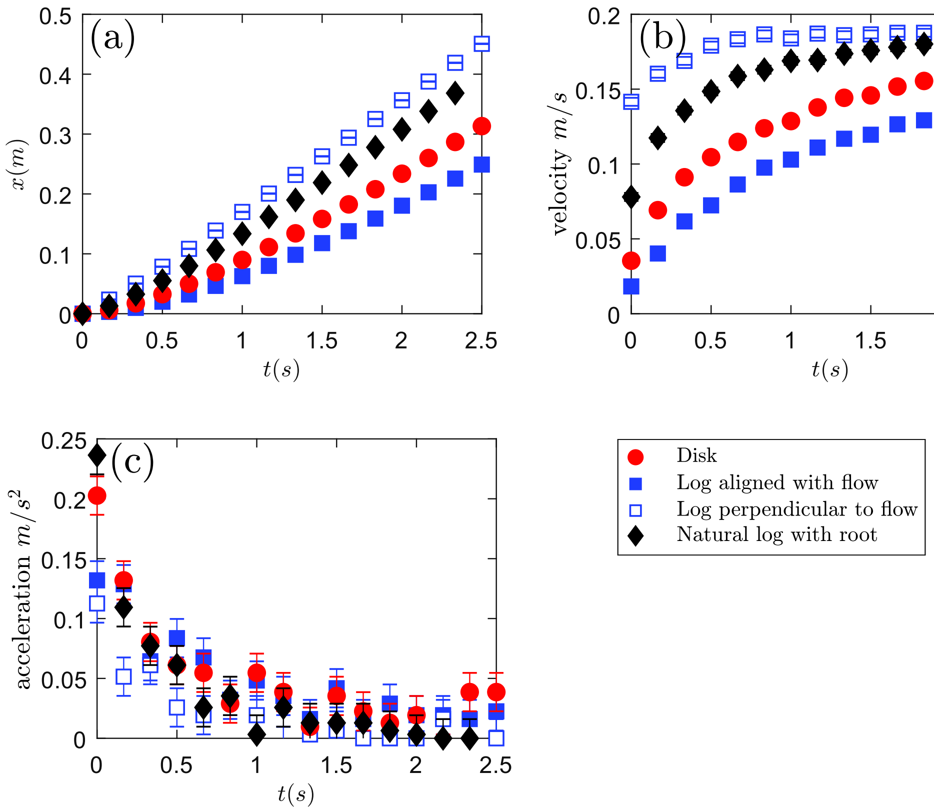

Figure III.18: An example for the results of object detection for four different floats: (a) Trajectory (b) velocity and (c) acceleration.

lack of clarity in pixels. To decrease the sensitivity of acceleration to the time intervals, in order to be able to show the variations of object acceleration, here we decrease Δt 10 times by showing one frame from each 10 frames. If instead of each frame, we measure δv and δa between each 10 frames then δv=5 mm/s and δa=30 mm/s^2. Therefore, in this figure, each scatter point represents one frame from each 10 consecutive frames. The floating objects which are presented here are disk (red circles), log aligned with the flow (filled square) and perpendicular to the flow (hollow square) and natural rooted logs (black lozenges). Note that here only one sample of each geometry is presented. In addition to the trajectory, the velocity and acceleration of the floats are presented in Figs. III.18(b), (c) respectively. It is seen that different objects have different accelerations in the same flow, resulting in different traveling distances during the same time. By releasing the object from the rest, its velocity increases and the acceleration decreases, which means that by releasing the object, the variation of object velocity is much faster at the first moments of the movement.

III.2.3 Object acceleration in uniform flow

III.2.3.1 Experimental principles

In this first experiment, we want to verify if λ is a characteristic response distance, scaling the object acceleration. To address this question, the easiest way is to consider object acceleration from rest in a uniform flow. Assuming a one-dimensional uniform flow of surface velocity U_0, a constant λ value and that at time $t = 0$, the object is at rest at $x = 0$, Eq. (III.2) has the following analytical solution

$$\tilde{x}(\tilde{t}) = \tilde{t} - \ln\left(1 + \tilde{t}\right), \tag{III.6}$$

where $\tilde{x} = \frac{x}{\lambda}$ and $\tilde{t} = \frac{t}{\lambda/U_0}$. Note that here $\tilde{}$ denotes nondimensional variables using in particular λ as a length scale, since there is no characteristic flow length scale in this problem.

Since it was experimentally difficult to get accurately the time at which the object velocity was exactly 0, the initial velocity was measured and used in the fitting equation (which takes therefore, a slightly different expression). Considering the acceleration of a particle initially at rest under a uniform steady flow, Eq.(III.2) simplifies as,

$$\frac{d\mathbf{v}^\star}{dt^\star} = \frac{1}{\lambda^\star}|\mathbf{u}^\star - \mathbf{v}^\star|\left(\mathbf{u}^\star - \mathbf{v}^\star\right). \tag{III.7}$$

Assuming $L_0 = \lambda$ for normalization, the advection equation can be simplified into the following scalar equation in 1D uniform flow,

$$\frac{d\tilde{v}}{d\tilde{t}} = (1 - \tilde{v})^2, \tag{III.8}$$

where $\tilde{v}$ is the streamwise particle velocity normalized by the surface flow velocity U_0. This equation can be integrated analytically so that the nondimensional velocity $\tilde{v}$ and position $\tilde{x}$ read

$$\tilde{v}(\tilde{t}) = 1 - \frac{1 - \tilde{v_0}}{1 + (1 - \tilde{v_0})\,\tilde{t}}, \quad \tilde{x}(\tilde{t}) = \tilde{t} - \ln\left[1 + (1 - \tilde{v_0})\,\tilde{t}\right] \tag{III.9}$$

considering that $\tilde{v}(\tilde{t} = 0) = \tilde{v_0}$ and $\tilde{x}(\tilde{t} = 0) = 0$.

The acceleration measurements are performed on each floating object, and repeated 25 times in order to get a correct averaging. The objects are released in the middle of the channel, 3 m downstream the channel entrance, *i.e.* at the upstream limit of the FOV, in order to record their 1D acceleration from rest. After recording the object acceleration, Eq. (III.9) is fitted on the trajectory with a least-square method using only λ as a calibration parameter.

III.2.3.2 Model validation

In a first step the model of Eq. (III.9) is validated against our experiments in Fig. III.19. This figure shows the normalized object velocity $\tilde{v} = v/U_0$, as a function of

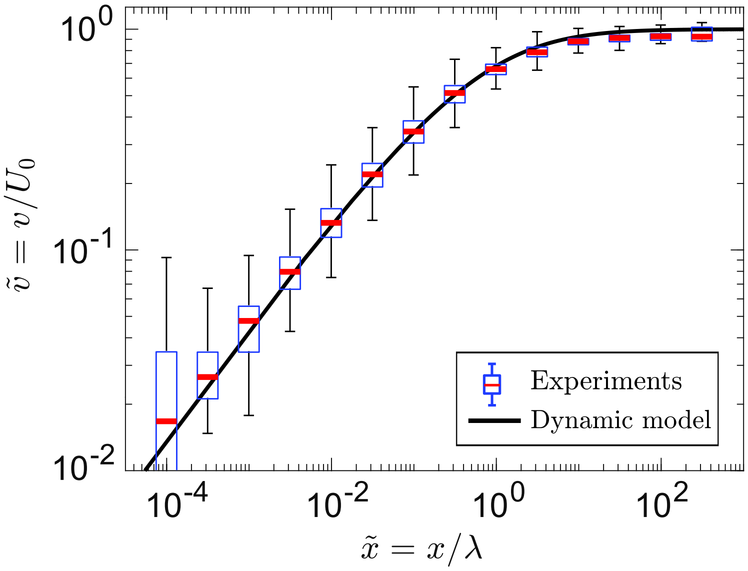

Figure III.19: Comparison of the dimensionless velocity as a function of the object dimensionless position for all experimental data together (boxplots) and the solution of dynamic model from Eq. (III.9) (black line).

the object dimensionless position $\tilde{x} = x/\lambda$ for all objects with different geometries and sizes. The boxplots represent the median (red lines), interquartile range (blue boxes) and minimum and maximum values (black whiskers) of experimental trajectories. The analytical solution of Eq. (III.9) is shown in black line. From Fig. III.19, we readily see that the model matches very well with the experiments, allowing us to conclude that λ can be considered as a length scale of the object acceleration. As an indication, λ is the distance needed to accelerate and reach about 70% of the surface velocity.

III.2.3.3 Effect of the geometry on λ values

Based on the scaling analysis of section III.2.1, λ is expected to scale as the streamwise body length of the floating object L_x. This is analyzed in Fig. **??**, which shows λ normalized by L_x as a function of the object aspect ratio L/D, for floating disks (red boxplots), logs aligned with the flow (filled blue boxplots) and perpendicular to the flow (hollow blue boxplots). Boxes and whiskers show the interquartile and extreme ranges for each set of objects.

This figure confirms that for all objects, regardless of shape, size or orientation, λ scales as L_x the streamwise body length, as expected from Eq. (III.3). The exact proportionality coefficient ranges from 2 to 4 for two orders of magnitude in aspect ratio. Strikingly, the scaling is almost identical for logs aligned and perpendicular to the flow. The slight variations of λ/L_x among different objects can be due to changes in C_D and C_A, but at leading order these variations are negligible for $L/D > 0.3$. For disks,

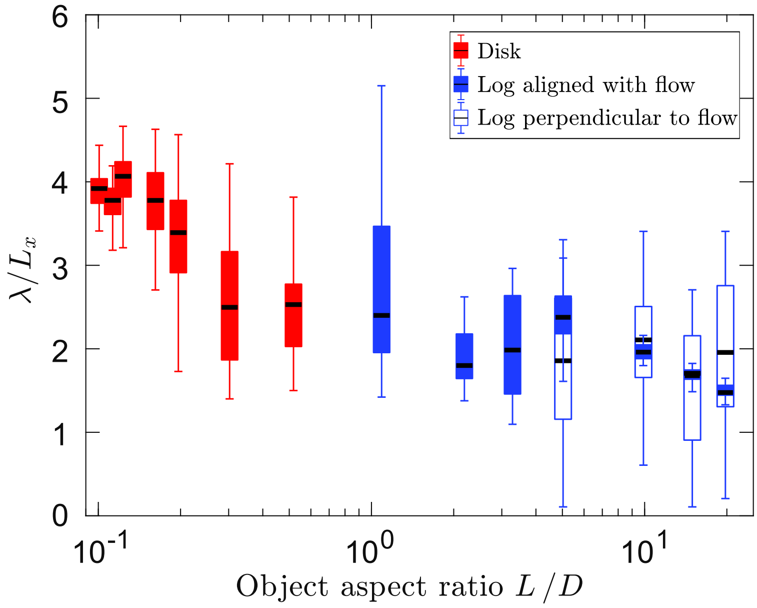

Figure III.20: Evolution of λ normalized by the object streamwise body length L_x as a function of object aspect ratio for floating disks (red boxplots), logs released aligned with the flow (filled blue boxplots) and logs released perpendicular to the flow (hollow blue boxplots)

however, in the range $0.15 < L/D < 0.3$, λ/L_x increases with decreasing aspect ratio, *i.e.* as the disks become flatter. This can be due to increased friction drag rather than pressure drag, changing therefore, significantly the drag coefficient. Note that since the orientation of short logs is random, only one symbol is plotted in the range $1 < L/D < 3$.

The presence of roots is another geometric parameter that is expected to affect λ. To check this effect, four different patterns of root are tested in Fig. III.21 which shows the effect of dimensionless root frontal area on λ normalized by the response distance of the same log without roots λ_{trunk} as a function of the ratio between frontal area of rooted logs and the frontal area of the same log without root S_{root}/S_{trunk}. The four different root patterns are: artificial logs with different root lengths (blue), with different number of roots (red), with a circle at one side of log instead of roots (cyan) and also three different natural logs (yellow) (Fig. III.11). Rooted logs can be released aligned with the flow in two different situations, roots are located at upstream side or downstream side of the trunk. To check the effect of root position, in one case (logs with different root numbers), the log is released in both situations denoted by hollow and filled red boxplots for upstream and downstream side roots.

Based on Fig. III.21, by increasing object frontal area, λ/λ_{trunk} decreases, but different root patterns with the same frontal area, resulted in the same λ/λ_{trunk}. One can conclude that at leading order, the only effective parameter on λ/λ_{trunk} is object frontal area S_{root}/S_{trunk}, not the root pattern. In addition, comparison between the

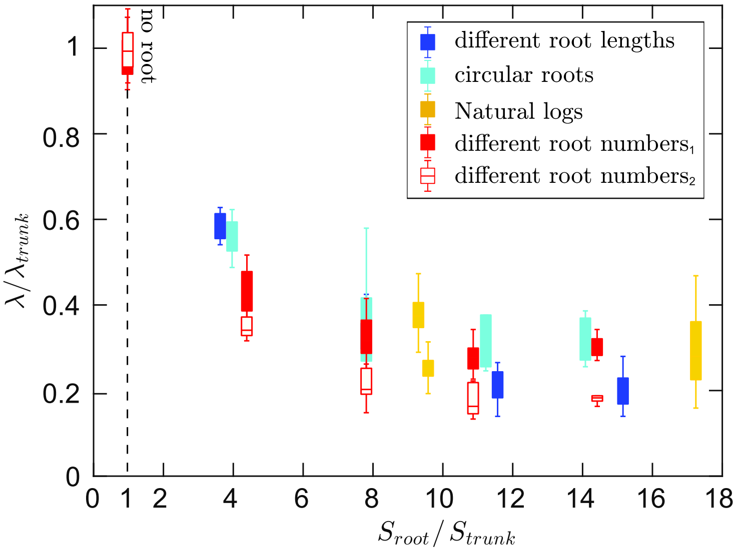

Figure III.21: Effect of root on λ normalized by rootless trunk λ_{trunk} as a function of rooted log frontal area normalized by trunk frontal area S_{root}/S_{trunk} for logs with different root patterns. Indexes 1, 2 for different number of roots (filled and hollow red boxplots) show two different positions of roots, on downstream side (1) and upstream side (2) of the log, indicates that the different position of roots does not affect λ.

different positions of roots, downstream or upstream of trunk (filled and hollow red boxplots), show that the location of root has no effect on object motion. Based on this figure, at the leading order, the frontal area plays a role on variations of λ. At the second order, the root pattern causes dispersion on data. In addition, there is a global dispersion on these data due to the sensitivity of λ to flow variations which is increased by increasing root size.

III.2.3.4 Effect of relative water depth

In order to verify whether the assumption that the particle is only affected by the flow surface velocity U_0 is correct, two sets of experiments are done: in the first set (red boxplots) we used the same object in different water depths, resulting in different shallownesses (Shallowness = disk submerged length / water depth). In the second set of experiments (blue boxplots), objects with different heights are recruited in flow (with the same depth and velocity). Figure III.22 shows the results of these experiments. As discussed earlier λ is normalized by L_x which here is the disk diameter.

According to this figure, as long as shallowness is less than 0.5, λ/L_x is approximately constant. Based on this preliminary test, we observe that as long as the immersed dimension of the object is less than half the flow depth, the object motion is affected only by the surface velocity and not the vertical velocity profile. Consequently 2D surface

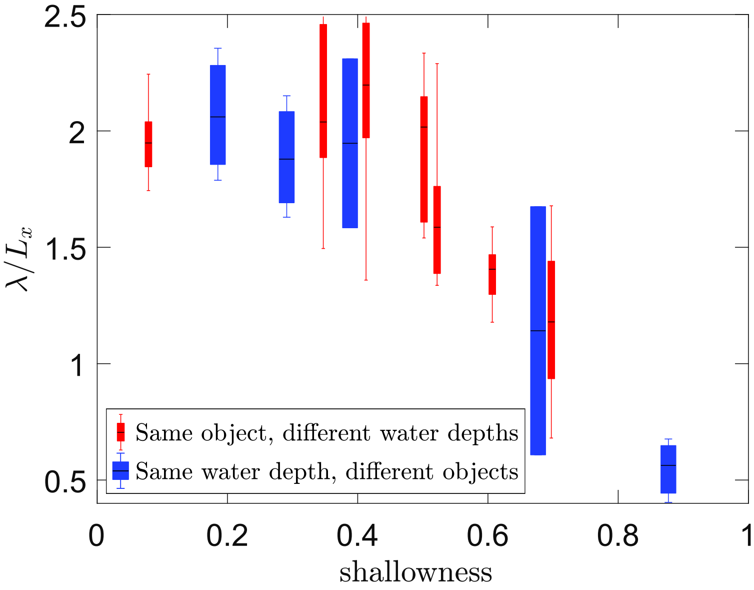

Figure III.22: Object characteristic response distance λ normalized by disk diameter as a function of the flow shallowness

BBO model is validate as long as *shallowness* < 0.5. This condition is largely satisfied in all experiments, so that the objects motion is only driven by the two-dimensional surface flow.

III.2.3.5 Effect of particulate Reynolds numbers on λ

Based on Eq. (III.3), λ is linked to Re_p by C_D. Given that in the range of Re_p (between 10^2 to 10^4) that is studied here, C_D is constant, therefore, it is expected that in this range of Re_p, variation of Re_p does not affect λ and as a consequence λ/L_x remains constant. The glass wall channel has the limitation in flow velocity and water depth, therefore, to validate this statement a set of experiments was done in a concrete channel with 1×1m cross-section and 12 m length as it is shown in Fig. III.23 and a set of larger woods with diameter from 2 to 10 cm and with aspect ratio of 10 were used. But the high variations of the flow and presence of significant vorticity in the flow did not allow us to conclude, and this could be done in a future work.

III.2.3.6 Conclusion

In summary, the acceleration experiments show that λ is indeed a characteristic response distance scaling the object response to the flow. For floating objects at large Re_p for which the drag and added mass coefficients are expected to be constant and of order 1, if the object is only affected by the surface velocity fields, this response distance is typically 2 to 4 times the streamwise body length for symmetric objects in streamwise

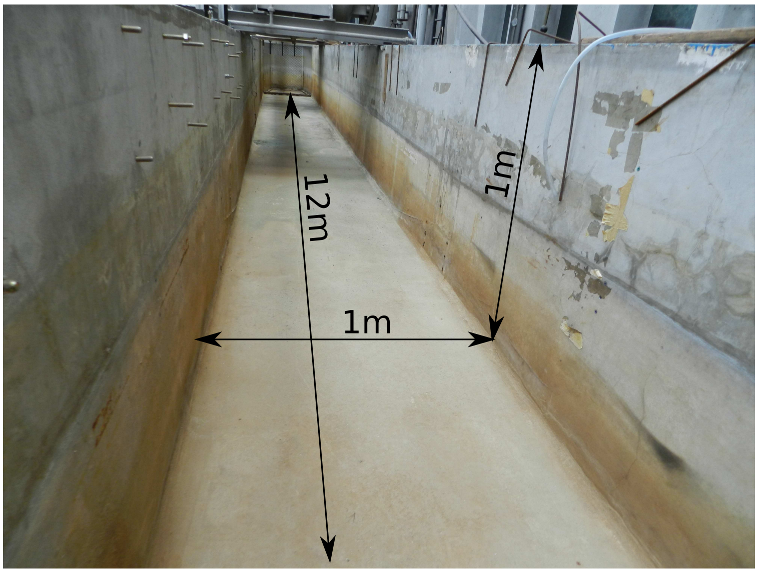

Figure III.23: The concrete channel used for experiments at large Reynolds number.

direction and is a function of object frontal area for rooted logs, providing a useful tool for estimating this distance with purely geometric information. In the next Section, we turn to a nonuniform flow to test the validity of the kinematic and dynamic approaches in a spatially varying flow, for modeling the motion of a piece of wood in front of an obstacle.

III.2.4 Object motion in presence of an obstacle

In previous section, it is seen that λ is a length scale that properly scales the acceleration length of the object in 1D uniform flow. The more complex case of this section is the motion of disks, simple and rooted logs within a 2D nonuniform flow around a cylinder. This aims at reproducing the motion and the impact process of a wood facing with an obstacle.

III.2.4.1 Experimental principles

III.2.4.1.1 Irrotational flow

We consider now an object initially at the flow velocity $\mathbf{v}^\star(t^\star = 0) = \mathbf{u}^\star$ in a nonuniform flow around a cylinder. This flow is particularly interesting as it can be correctly modeled – apart from the wake – by a 2D potential flow model. In mathematics, potential flow around a circular cylinder is a classical solution for the flow of an inviscid, incompressible fluid around a cylinder that is transverse to the flow. The flow has no vorticity and thus the velocity field is irrotational and can be modelled as a potential flow. Flow surface velocity was measured by SPIV (Fig. III.24(a)) and the results were compared to the theoretical expression of the potential flow around a cylinder (Fig. III.24(b)) in terms

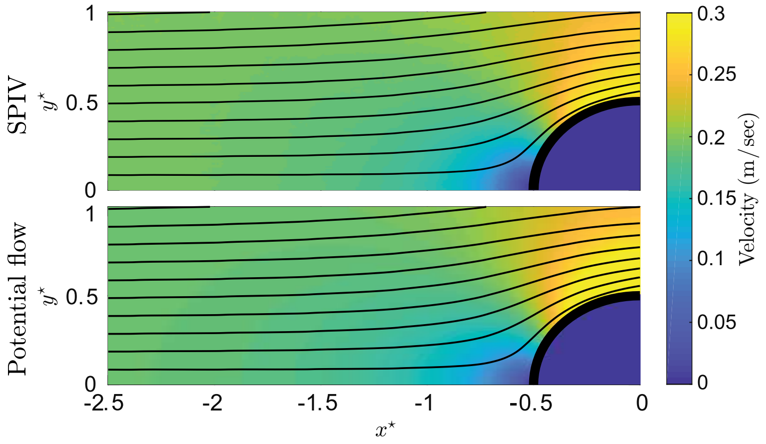

Figure III.24: Verification of the validity of irrotational flow by comparing the experimental SPIV velocity fields with the numerical potential flow velocity fields.

of streamlines. To measure the discrepancies between two methods, first, the norm of velocity is measured, at each point of Figs. III.24(a), (b). Then the relative error is measured by subtracting potential flow velocity norms from SPIV velocity norms divided by SPIV velocity norms at each point. Results show discrepancies of about 6% in general, and up to 12% close to the obstacle. Under this condition, the flow can be considered as irrotational and Eq. (III.2) can be used to model the advection of floating disks that are symmetric with respect to the flow.

III.2.4.1.2 Characteristic lengths of the floats

In this set of experiments, the disks, with seven different diameters (2 to 10 cm), the four largest logs without roots (5 to 20 cm) and the logs with different number or length of roots are used as floating objects (Table III.3). The typical λ for such objects is 4 to 40 cm for disks, 12 to 30 cm for simple logs and 4 to 20 cm for rooted logs.

As mentioned in section III.2.1, $\lambda^\star$ is defined as the ratio between object characteristic response distance λ and flow length scale. Here the obstacle diameter L_0 is used as the flow length scale. The study of the effect of $\lambda^\star$ on motion of an object when $\mathbf{v}^\star = \mathbf{u}^\star$ is performed only in the case of disks, with three different obstacles (fixed on the channel bed) with $L_0 = 4$, 10, 20 cm, resulting in 21 different $\lambda^\star = \lambda/L_0$ values from 0.24 to 10.2. In the two other cases (logs with and without root) only the obstacle with $L_0 = 20$ cm is used, and $\lambda^\star$ is varied from 0.6 to 1.5 for simple logs and from 0.2 to 1 for rooted logs.

III.2.4.1.3 Experimental conditions

Figure III.25 shows the schematic view of the experiment. The "obstacle" is an emergent cylinder of diameter L_0 is located at 3.6 m downstream of the channel entrance, *i.e.* at the downstream limit of the FOV. The length of the FOV (60 cm) is chosen so that

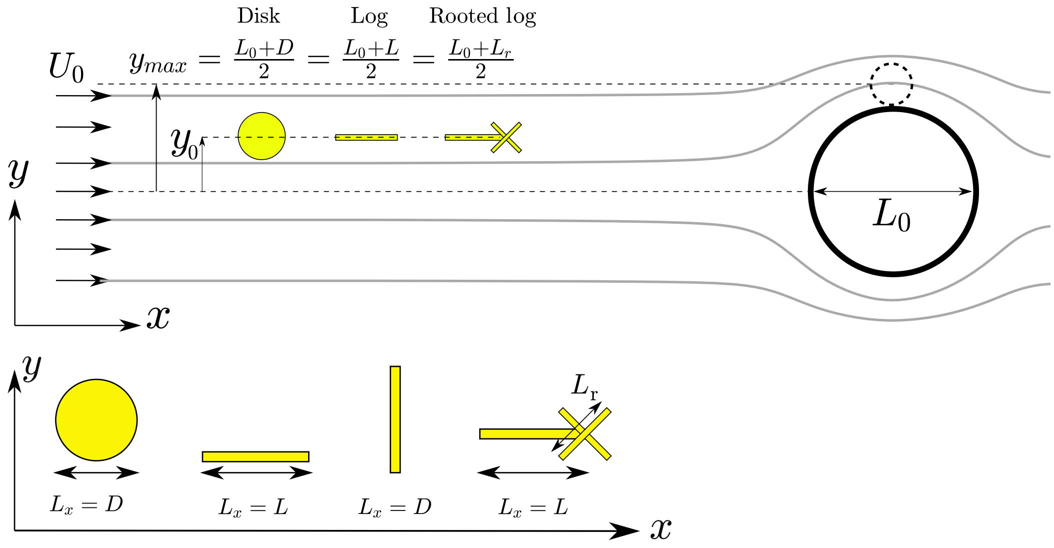

Figure III.25: Schematic view and parameters for the advection experiment in a flow around a cylinder.

at its beginning, the flow is not affected by the obstacle (negligible backwater and side effects).

To satisfy the initial condition $\mathbf{v}^\star = \mathbf{u}^\star$ at the entrance of the FOV, objects are released 3 meters upstream of the obstacle, so that at the entrance of the field of view $\mathrm{v} > 0.95U_0$. The initial lateral position y_0 is varied between the central axis of the obstacle $y_0 = 0$ and a maximum distance $y_0 = y_{\max}$, where $y_{\max}$ choose as the distance above which even an object with straight trajectory does not hit the obstacle. As it is seen in Fig. III.25, considering y_{max} as the ultimate lateral distance from the obstacle center line for impact for an object with a straight trajectory, if y_0 is less than y_{max} (equal to the obstacle radius plus half of object transverse dimension), this object will hit the obstacle. Therefore, y_{max} is chosen here to be equal to the sum of the disk and obstacle radii $y_{\max} = (L_0 + D)/2$ for disks, sum of the object half length and obstacle radius $y_{\max} = (L_0 + L)/2$ for logs without root, and sum of the object half root length and obstacle radius $y_{\max} = (L_0 + L_r)/2$ for rooted logs. The definition of the parameters is presented schematically in Fig. III.25. Since the objects are released far upstream, the trajectories are very sensitive to flow perturbations and to the release conditions and exhibit a small variability. To overcome this problem, the sampling for each configuration is repeated on average 100 times to get converged statistics.

In addition to the experiments, disk trajectories are modeled using Eq. (III.2), solved numerically using a Runge-Kutta 4th/5th order scheme (ode45 in Matlab®). The computations reproduce the experimental trajectories, starting from the experimentally-known initial position of the object and its nondimensional response distance $\lambda^\star$ measured in section III.2.3, and using either the theoretical potential flow or the experimen-

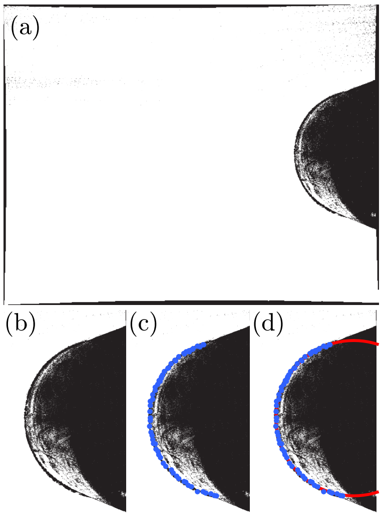

Figure III.26: Detecting the position of the obstacle on video frames.

tally measured flow.

III.2.4.1.4 Impact detection

To detect if an object hits the obstacle or not, in addition to detecting the object, the obstacle also has to be detected. Detecting the obstacle required 3 steps as presented in Fig. III.26. In a SPIV measurement test, the tracers spread throughout the frame unless in the region of the obstacle. Each frame of SPIV measurements contains many tracers that are clearly detectable. So in the first step, in order to be able to detect the obstacle boundaries, all frames in a set of SPIV measurement are added together. The result is a white plain with a black circle on one side as shown in Fig. III.26(a). In the second step, by zooming on the obstacle (Fig. III.26(b)) the boundary of the obstacle are recorded using the screen cursor as shown in Fig. III.26(c). 60 points are used as manual detection of the obstacle. Finally in the third step, a circle is fitted on scattered points as shown in Fig. III.26(d).

Having the dimension of the object and the boundary of the obstacle it is possible to roughly estimate if an object hits the obstacle or not. To be able to detect the impact more precisely, we tried to use the evolution of the object acceleration. This process is presented in Fig. III.27. Figs. III.27(a), (b) present two examples of the largest and smallest disks that both hit the obstacle. The obstacle is the large white circle on right side of each figure and the red and blue scatters show the trajectory of object. Additionally the object is presented with 10 frames intervals and the borders of the object is highlighted in yellow.

Knowing the center of area of object and obstacle at each frame, it is possible to estimate the distance between object and obstacle centers as shown in Fig. III.27(c) for largest (red) and smallest (blue) object. As it is seen on this figure, the distance

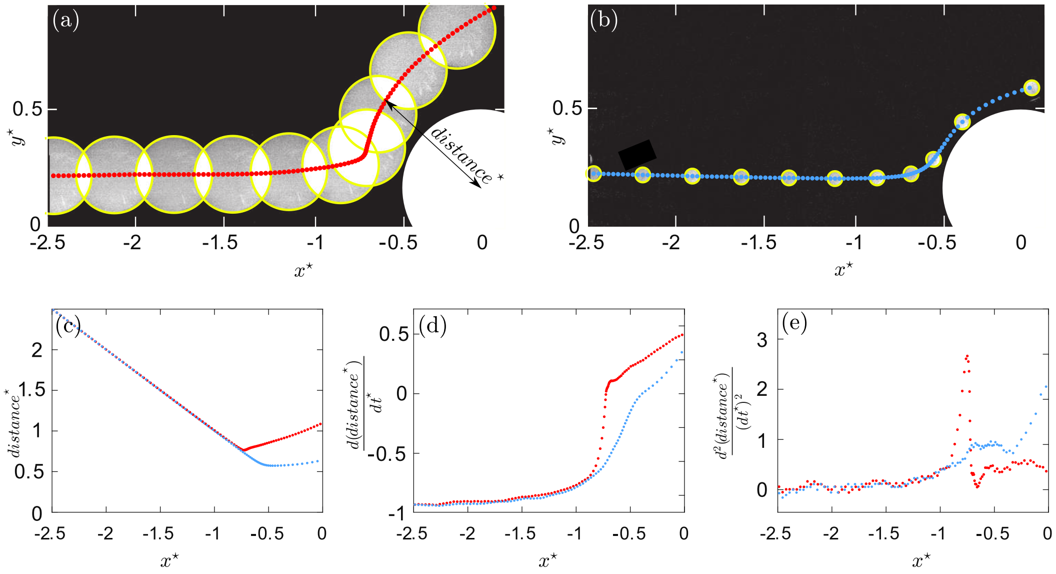

Figure III.27: Detecting the impact of an objects to the obstacle. Trajectory example for (a) one largest and (b) one smallest disk. Dimensionless distance (c), velocity ($\frac{d(distance^\star)}{dt^\star}$) and (e) acceleration ($\frac{d^2(distance^\star)}{(dt^\star)^2}$) (f) between object and obstacle centers.

between object and obstacle decreases until object gets close to the obstacle. Then there is two possibility, the object rotates around the obstacle (blue) or moves away from the obstacle after a severe impact (red).

Exactly at the impact position, the sign of the distance velocity ($\frac{d(distance^\star)}{dt^\star}$) changes from negative to positive values as shown in Fig. III.27(d). Based on the severity of the collision, this sign change can be smooth (blue) or sharp (red). The sharp sign change in velocity, results in a large oscillation in the distance acceleration ($\frac{d^2(distance^\star)}{(dt^\star)^2}$) which is shown in Fig. III.27(e). This large oscillation is due to the momentum transfer at the impact position. As it is seen on Fig. III.27(e) the position of impact is clearly detectable for the largest disks (red) while for the smallest one, due to the much smaller momentum transfer, the impact is not clearly visible. Similar to the small object on this figure, if the largest disk just touch the obstacle side at larger lateral positions the evolution of distance velocity is same as the blue scatters on this figure. Therefore, in this experimental configuration and using the video frames, only the severe impacts are detectable automatically. Thus, while in many cases the distance acceleration works well as a criterion for impact, it is not possible to detect all impacts by this criterion. In these cases, the impact is detected manually and based on user detection. However, the distance is a useful criterion to select only the objects that are close enough to the obstacle. Note that even with manual detection in some cases it is not possible to detect the impact with 100% confidence.

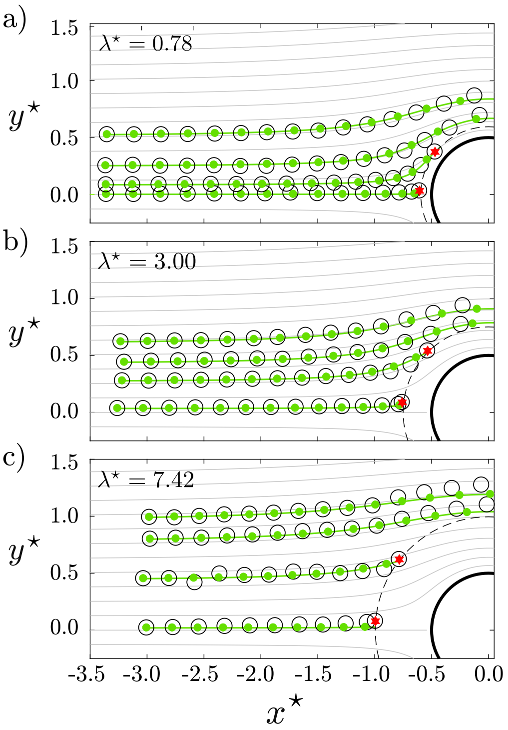

Figure III.28: Comparison between individual experimental trajectories and numerical model based on the potential flow for $\lambda^\star = 0.78$, 3 and 7.42. The experimental trajectories are represented as black hollow circles, and the dynamic modeled (Eq. (III.2)) ones as green points and solid lines. Note that the symbols are not at scale, and the dashed line around the obstacle represents the limit for impact. Red stars show impacts, and gray lines are flow streamlines.

III.2.4.2 Dynamic vs kinematic approaches (in case of disks)

In the following section, the disk motions are modeled by both dynamic and kinematic approaches and the results are compared to the experimental trajectories in order to show the validity of each approach to model high particulate Reynolds objects.

In the first part of this section, the individual trajectories are presented to show a comparison between real experimental trajectories and the numerically computed ones. But as it is not possible to show all trajectories one by one, in the second section, the statistics related to the transverse position of impact is presented for all trajectories together.

III.2.4.2.1 Individual trajectories

We first show some individual trajectories, with and without impact of the disks on the obstacle. Fig. III.28 compares the experimental trajectories (black hollow circles)

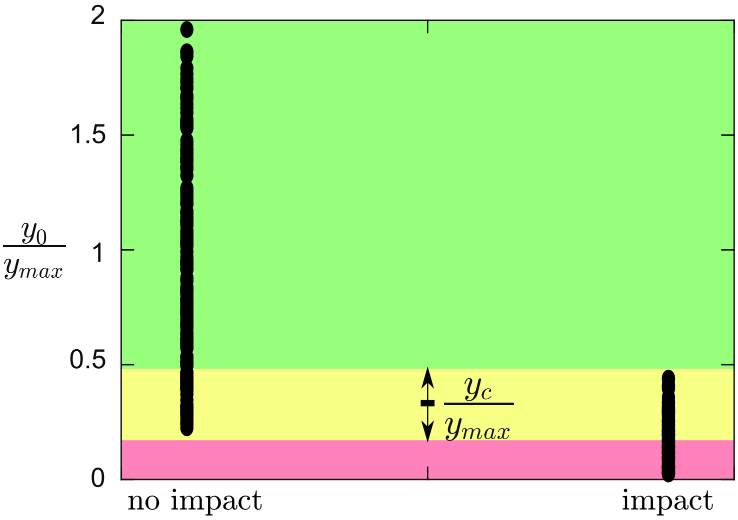

Figure III.29: Statistics of the impact of one configuration ($\lambda^{\star}$=0.4). Green color depicts 100% no impact region, red color depicts 100% impact region and yellow color depicts the region with some impacts due to the experimental dispersions.

with the numerical models (green points and solid line) for three values of $\lambda^{\star}$, showing a good agreement between real trajectories and the predictions of the BBO model of Eq. (III.2). In addition, the model accurately predicts impact occurrences and its location (red stars). Note that the green and black circles only represent the center of mass of floats, and do not depict at scale the floating disks. In particular, for the highest value of $\lambda^{\star}$ in Fig. III.28(c) the disk diameter is comparable to that of the obstacle, which might question the validity of Eq. (III.2). However, the numerical predictions still show satisfying results, with small deviations observed as the floats pass the cylinder. One can note a slight time lag between experimental and numerical trajectories, due to uncontrolled variations of the surface velocity in the experiments (of less than 2%).

III.2.4.2.2 Statistics on $y_c/y_{max} = f(\lambda^{\star})$

As mentioned in section III.2.4.1.2 , each configuration (corresponding to one $\lambda^{\star}$ value) was repeated on average 100 times, leading to a total of more than 2000 available trajectories only for disks. Figure III.29 shows all iterations for one configuration where, λ=8 cm, L_0=20 cm and therefore, $\lambda^{\star}$=0.4. In this figure, the vertical axis shows the initial transverse position of the object, and on the horizontal axis, if the object hits the obstacle or not. As it is seen near the centerline of the obstacle (the red region) all objects hit the obstacle and far from the centerline (the green region) all objects pass the obstacle. In the experimental measurements due to the flow variations and experimental dispersions there is a region that some objects hit the obstacle and the others do not hit it (the yellow region). We use this region, in order to have a global measure of the

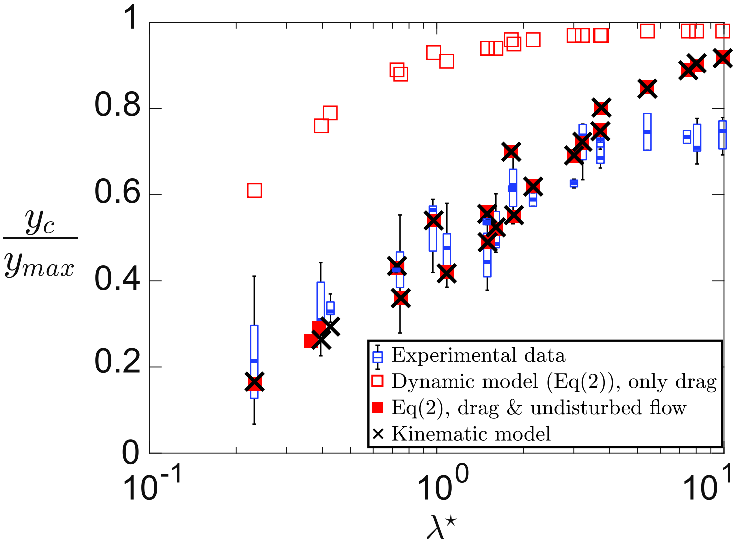

Figure III.30: Critical lateral position for impact y_c normalized by $y_{\max}$ as a function of $\lambda^\star$: experiments (blue boxplots), dynamic model of Eq. (III.2) based on the potential flow using the drag force only (empty red squares) and both forces (filled red squares), and kinematic (*i.e.* tracer) model (black crosses).

model validity. For each configuration a critical value of the initial lateral position y_c is defined, so that if $y_0 < y_c$ impact occurs and if $y_0 > y_c$ the disk passes the obstacle without impact.

To be able to compare all 21 configurations together Fig. III.30 shows this critical distance y_c normalized by $y_{\max} = (L_0 + D)/2$ as a function of the normalized characteristic response distance $\lambda^\star$. As mentioned in Fig. III.29 due to the experimental variability, for one given $\lambda^\star$ there is a range of y_0 where some objects hit the obstacle and others do not, so y_c is taken to be the median value of these cases, and the extent of this range is described by the blue boxplots. In this figure, in addition to the experiments, two numerical results are shown, one by considering only the drag force in the BBO equation – so only the second term of the right-hand side of Eq. (III.2) (empty red squares) – and one considering the full expression of Eq. (III.2) (filled red squares). Finally, the prediction using the kinematic model ($\mathbf{v}^\star = \mathbf{u}^\star$ all along), corresponding to a tracer, is represented in black crosses. Note that this prediction can be obtained analytically from the potential flow streamlines equations.

While considering only the drag force is not satisfying, the complete model of Eq. (III.2) with both undisturbed flow force and drag force predicts the critical lateral position for impact quite accurately. Additionally, the kinematic model provides also very satisfying predictions. The increase in $y_c/y_{\max}$ with $\lambda^\star$ is thus not related to an increasing inertia of the floating object. Actually, when considering a disk, increasing $\lambda^\star$ can only be achieved by increasing its diameter (see Fig. III.20) or decreasing the obstacle diameter, resulting in an increase of $y_c/y_{\max}$ due only to geometry. Moreover, the fact that in Fig. III.20, λ/L_x is not a bijective function of object geometry, causes dispersion on numerical models in this figure. These results confirm the analysis performed in section III.2.1 that if initially the floating object is at the flow velocity ($\mathbf{v}^\star = \mathbf{u}^\star$) it behaves as a tracer regardless of its non-dimensional response distance $\lambda^\star$. Note that for large values of $\lambda^\star$, a deviation is observed between the experimental data and the models. This is again due to the fact that for these large values, the object size is larger than the flow scale L_0, and the assumption of point object is clearly broken.

The numerical simulations were also carried out using the experimentally measured velocity field, resulting in very similar results to those shown in Fig. III.30 (about 7% difference in average).

Moreover, the assumption of irrotational flow was tested by adding the lift force due to vorticity (Magnaudet & Eames, 2000) in these numerical simulations. To check if the irrotational flow assumption is correct, we model floating disk trajectories by two models, first, using Eq. (III.2), and second, adding the lift force due to flow vorticity (Eq. (III.10)) to the same equation.

$$F_L \quad = \quad \rho_f C_L V_f \left(\mathbf{u} - \mathbf{v}\right) \times \omega. \tag{III.10}$$

where C_L is lift coefficient due to to flow vorticity and $\omega = \nabla \times \mathbf{u}$ is the flow vorticity. The simulations on the real flow field with and without lift force due to vorticity give identical results (less than 4% difference), confirming the validity of the potential flow assumption and that the effect of the lift force is negligible here. Comparing the two models in Fig. III.31 with 1:1 dashed line, confirms that both models result in the same values.

III.2.4.3 Generalization to the wood like geometry

In the previous section, we show that as soon as a floating disk reaches flow velocity, it can be considered as a tracer. This is validates the theoretical analysis in the section III.2.1. To generalize the validity of this statement for wood logs, in addition to the disks, the trajectory of the logs with different lengths are compared with the flow streamlines. After detecting the lateral initial position of the object $y_0^\star$, the corresponding flow streamline is measured (blue line in Fig. III.32). Then, the transverse difference between object trajectory (red line in Fig. III.32) and the streamline (blue line in Fig. III.32) is measured along the trajectory. This transverse difference is named $d_y^\star$. By applying this process on all trajectories, $d_y^\star$ can be estimated throughout the FOV. Figure III.33 shows the median value of these differences at each point. The white area is the region with no data. Despite the big difference between disks and logs geometries, in both cases, the deviation from corresponding streamline is almost the same. Based on these figures the deviation from streamlines is limited to 4% of L_0 and in a limited region in the range of $-1 < x^\star < 0$ and $0 < y^\star < 0.3$.

However, Fig. III.33, shows that close to the obstacle, the trajectory is modified. The question here is that based on the object initial transverse position $y_0^\star = 0$, what is the

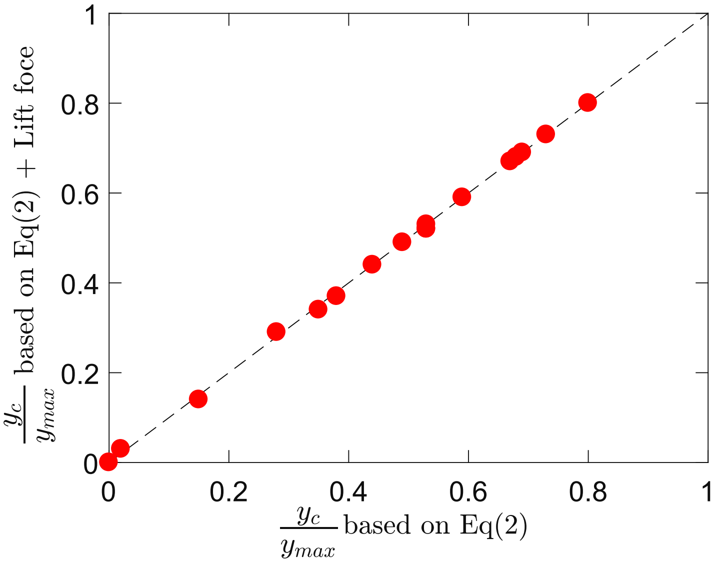

Figure III.31: Comparison the results of numerical model with and without effect of lift force due to flow vorticity.

maximum $d_y^\star$? Figure III.34, shows the $d_y^\star$ for both logs (blue) and disks (red) along the FOV as a function of $x^\star$. In order to show the effect of initial transverse position of a float simultaneously, this figure is separated in four different transverse positions with respect to the obstacle diameter L_0. This graph confirms that the deviation from streamline is almost the same for the two totally different geometries. For objects closest to the centerline $0 < y_0^\star < 0.125$ deviation from streamlines starts from $x^\star \cong -1$. It reaches its maximum value near the starting point of the obstacle on the transverse section $x^\star \simeq -0.6$ and at obstacle transverse centerline ($x^\star = 0$) trajectory again superposed on its initial streamline. By getting away from the centerline in the transverse direction, deviation vector tends to zero.

Based on Figs. III.33 and III.34, the maximum $dy^\star$ is detected at $x^\star = -0.6$.

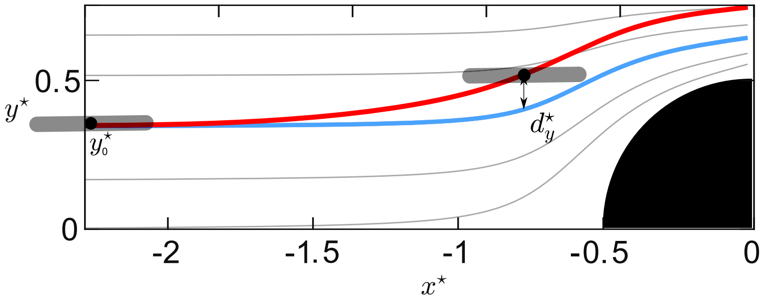

Figure III.32: Schematic view of the transverse difference between object trajectory and corresponding flow streamline.

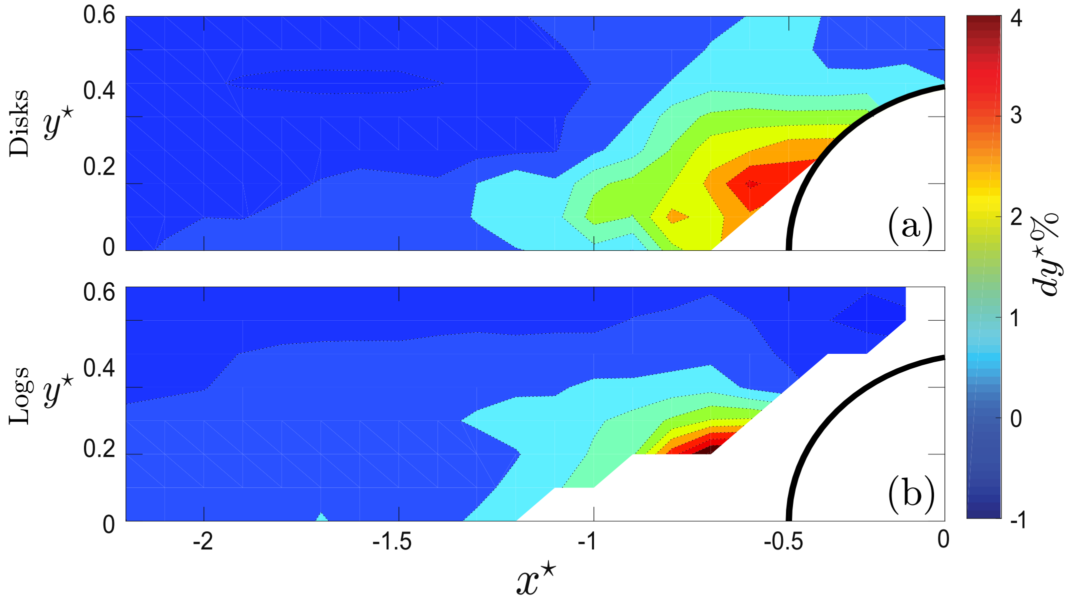

Figure III.33: Difference between trajectory and corresponding initial streamline at the start of FOV for disks (a) and logs (b).

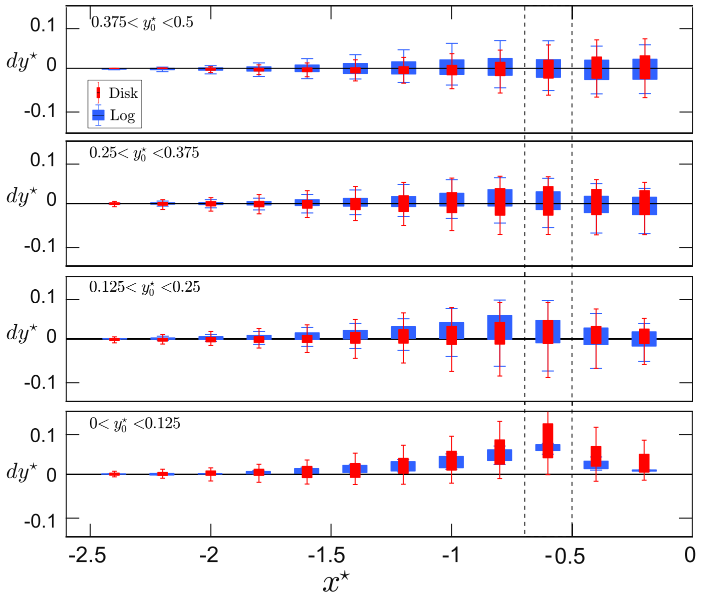

Figure III.34: Variation of $d_y^\star$ for logs (blue) and disks (red) in streamwise direction for different values of the initial transverse shift from the obstacle centerline.

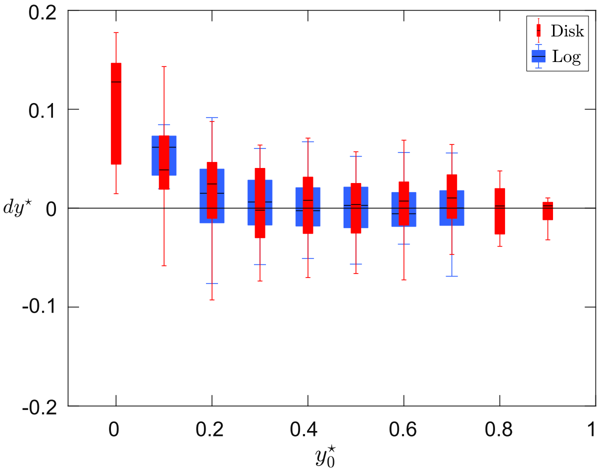

Figure III.35: Variation of $d_y^\star$ for both logs (blue) and disks (red) in lateral direction with the change in initial transverse position.

To demonstrate the effect of the initial transverse position on the deviation from the corresponding streamline in lateral direction, Fig. III.35 shows $dy^\star$ in the range of $-0.7 < x^\star < -0.5$ (presented by dashed line in Fig. III.34) as a function of initial transverse position $y_0^\star$. It is seen that just near the obstacle there is a deviation around 10% of L_0 which decreases to 0 when $y_0^\star > 0.25$.

As a conclusion, if initially object has the same velocity as the flow, the floating object, independent from its geometry *i.e.* disk or log, can be considered as a tracer. Notwithstanding a deviation of 4% just near the obstacle.

III.2.4.4 Impact process

In the previous section we show that independent of object geometry, both logs and disks can be considered as tracers. The question here is, if the object follows the streamlines, what cause this object to hit an obstacle? To address this question here we consider experimentally the impact process for simple and rooted logs, as the most complex geometries in this study.

III.2.4.4.1 Effect of log length scale $\lambda^\star$ and initial orientation

To control the concurrent effect of log length scale and the initial orientation of the log, different logs with random orientations were released within the flow and their lateral position and orientation at the start of the FOV were recorded. Figure III.36 shows an example of sampling for one log configuration with $\lambda^\star = 0.6$. The vertical axis represents the initial position of the log in the lateral direction, normalized by the ultimate distance from center line above which no object hits the obstacle y_{max} (see Fig. III.25). The horizontal axis is the orientation of the log at the start of the FOV. Each scatter point corresponds to one sampling. If object hits the obstacle the marker is a

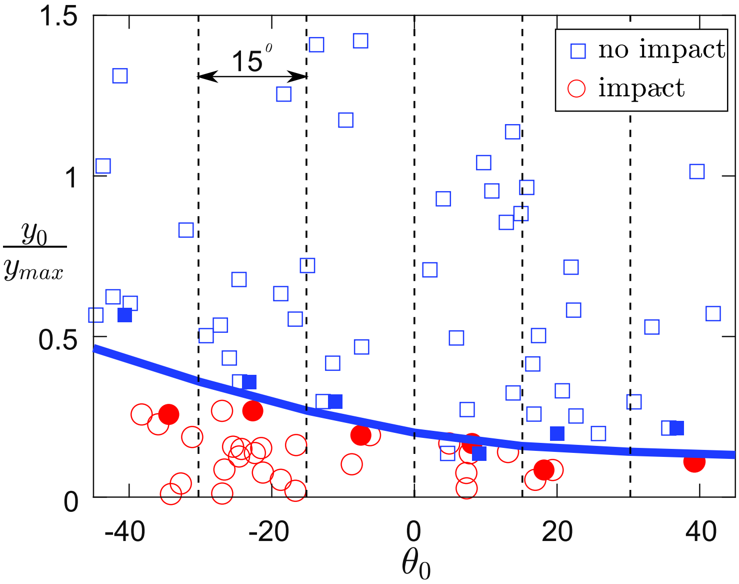

Figure III.36: Statistics for the impact of one configuration of simple logs ($\lambda^{\star}$=0.6, no root). Filled markers are the maximum values of no impacts and minimum values of impacts at each 15^o intervals and the line passes throughout these filled markers separates the impact and no impact regions.

red circle otherwise the marker is a blue square. As it is seen, there is a line below it almost all logs hit the obstacle and above that all the logs pass the obstacle. To be able to separate impact and no impact regions by this line, the horizontal axis is separated in 6 parts with 15^o width. At each section, among all blue scatters, the minimum one and among all red scatters the maximum one is selected. These points are presented with filled markers. A line is fitted among these points to separate two regions. Therefore, the blue line shows the critical value of the initial lateral position y_c, so that if $y_0 \leq y_c$ impact occurs and if $y_0 > y_c$ the log passes the obstacle without impact. Fig. III.37 shows this distance y_c as a function of y_{max} for four different configurations of the simple logs.

As mentioned in section III.2.4.1 y_{max} is the ultimate distance from obstacle center line for impact, independently from the streamlines and only based on the object geometry. As it is seen in Fig. III.37(a), normalizing object transverse position by y_{max}, results in almost the same values of the critical line for impact for different logs. Moreover, the Fig. III.37(a) indicates that the other effective parameter in the impact process of a log, is its initial orientation so that decreasing initial orientation of a log results in increasing impact threshold from $y_c/y_{max} \cong 0.15$ to 0.5. This means that for a simple log, at leading order, the wood length and initial orientation affect the impact process simultaneously.

Figure III.37(b) is an example to show the effect of this initial orientation on the probability of impact, for the same log which follows the same trajectory (black line),

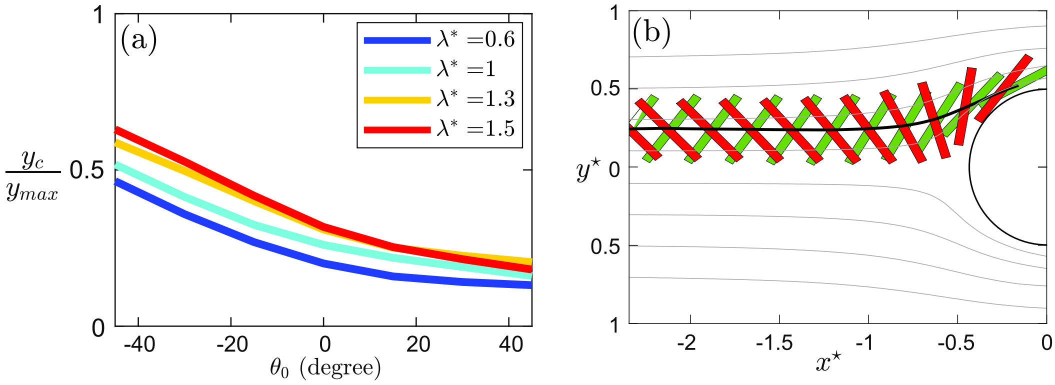

Figure III.37: (a) Critical lateral position for impact y_c normalized by y_{max} as a function of the log initial orientation θ_0 for logs with different $\lambda^\star$. (b) Two experimental examples for the behavior of the same object at the same $y_0^\star$ but with different θ_0.

but with different initial orientations. The object with negative initial orientation (red) is more likely to hit the obstacle, while the object with positive initial orientation (green) can pass the obstacle. Note that all dimensions are at scale.

III.2.4.4.2 Effect of rootwad

Finally, to see the effect of roots in impact process, rooted logs with different lengths and different number of roots (Fig. III.11(c), (d)) are tested. The results are shown in Fig. III.38(a). To check only the effect of roots in this test, all objects are released in the streamwise direction. Like in previous section, y_c is normalized by the ultimate distance from obstacle center line for impact y_{max}, which purely depends on object and obstacle lateral dimensions. Normalizing critical lateral position for impact y_c by y_{max} results in almost the same values for logs with different frontal areas. Here, the smallest S_{root}/S_{trunk} corresponds to the simple log without root. As it is seen, by normalizing y_c by y_{max}, at leading order, there is no difference between logs with or without root. One can conclude that if at one point $\mathbf{v}^\star = \mathbf{u}^\star$ the only effective parameter for impact is the lateral dimension. There is however some scattering, due to the complexity of geometry and small number of tests in this case.

To summarize this part of experiments, three different geometries (disk, simple log and rooted log) were tested. Firstly, it is seen that independently of geometry if $\mathbf{v}^\star = \mathbf{u}^\star$ the object behaves as a tracer. By measuring the ultimate distance from obstacle center line for impact y_{max} based on lateral dimensions of the object and obstacle, and normalizing the initial lateral position of the object by this value, we see that at leading order y_c/y_{max} depends on the geometry. Moreover, the initial orientation for logs can modify the impact threshold.

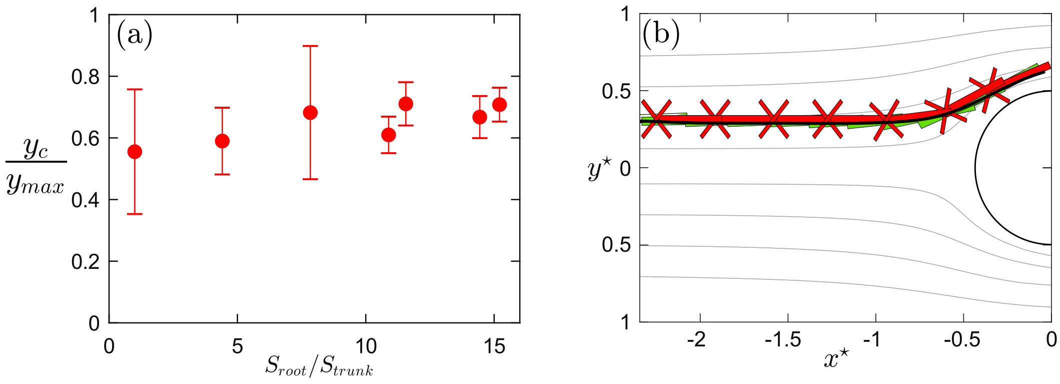

Figure III.38: (a) Critical lateral position for impact y_c normalized by y_{max} as a function of root frontal area for logs with different root patterns. (b) Experimental examples for logs with and without root at the same $y_0^\star$.

III.3 Conclusion

This chapter was dedicated to the dynamics of one single piece of wood. In the first part of the chapter the results of monitoring wood on the field on the Isère and the Ain Rivers were presented and we showed that firstly the transverse distribution of pieces of wood at leading order is independent of flood discharge. In addition it is shown that the floating pieces of wood at the surface have the same velocity as the flow velocity.

This latter result brought the question that to what extent a floating wood in river behaves like a tracer. To address this question, in the second part of this chapter, we considered the dynamics of wood like objects in two cases, first during their acceleration at the surface of a uniform flow, and second their motion in a nonuniform flow past a cylinder.

We first show that the dynamic model Eq. (III.2) fairly reproduces the accelerated motion of floating objects. Moreover, the acceleration experiments showed that λ, defined in Eq. (III.3), is an appropriate scaling for object acceleration from rest in a uniform flow, so that after a distance λ the object reaches about 70% of its terminal velocity. The experiments confirm the theoretical analysis say that at large Re_p when C_D is constant, λ can properly scaled by the streamwise body length L_x. Measurements showed that, regardless of size of disks or logs and orientation of the logs, λ was about 2 to 4 times L_x. This result is valid provided that C_D and C_A are of order one, which is the case for large wood in rivers. And finally in the case of rooted logs, we observed that at leading order λ is a function of root frontal area and at second order of magnitude, pattern or direction affect it.

In a second experiment, we considered floating objects initially transported at the flow velocity and facing an emergent cylinder to explore the effect of obstacle on object motion. The comparison between experiments, dynamic and kinematic models shows that these objects all behave as tracers, regardless of their normalized characteristic response distance $\lambda^\star$, as long as they remain smaller than the flow scale. This result is validate for both disk and log geometries with maximum 4% deviation just near the obstacle. This is an important result for the study of floating (or neutrally buoyant) objects that was anticipated by the asymptotic analysis of section III.2.1. Indeed, as soon as the object reaches the flow velocity, its motion will be accurately predicted by a kinematic model assuming the object is a flow tracer.

To analyze the process of impact for a log facing with an obstacle, three different geometries were tested, floating disks as the simplest case in an experimental work, and floating logs with and without roots. For these tracer objects the analyses showed that the object and obstacle lateral dimension play a key role on impact process so that by normalizing the initial position of the floats by y_{max} as the ultimate distance from obstacle center line for impact of an object with straight trajectory, at leading order all logs, with or without root show the same lateral distance for impact. Moreover, the initial orientation of a log plays role on impact process.

Knowing that (i) in a flow variation ,*e.g.* contraction, expansion or meandering, wood is accelerated in a limited length (ii) in large rivers typically floating wood pieces are passive tracers and (iii) in front of an obstacle at leading order, the geometry of wood and obstacle are the important factors in impact process, would be useful to assess the risks associated with the presence of large pieces of wood in rivers.

Chapter IV

Conclusion and prospects

IV.1 Thesis overview

On this work, we followed two main objectives. First, we studied the relation between wood and flow discharges in order to generalize the relation proposed by MacVicar & Piégay (2012). This was done based on streamside video monitoring on the field. The second major objective was to study the dynamics of one single floating piece of wood in river and its interaction with hydraulic structures across the river. This objective was studied on the field, in an experimental flume and with some numerical models. Additionally, comparing the results from different cameras on different basins, provides some knowledge on key-points such as locating and implementing video monitoring equipment. In the following part, all results are discussed and compared with other similar works to present appropriate recommendations regarding the hazards due to the motion of the wood in river.

IV.1.1 Summary

Present work is dedicated to the hazards associated with the presence of wood in rivers, containing two major results: (i) generalizes the relation between wood and flow discharges (chapter II) and, (ii) assesses the dynamics of a single piece of wood in river and its impact process (chapter III).

IV.1.1.1 Relation between wood and flow discharges

In chapter II, the wood discharges are studied by videography technique on the Isère and Ain Rivers in France. Two floods on the Isère River are monitored using a manual algorithm, and the statistics are presented in metric coordinates by orthorectification process. Additionally, to be able to compare two different catchments, we use the monitoring results of three floods on the Ain River collected from MacVicar & Piégay (2012). The results confirm that the wood discharge reaches its maximum value at bankfull discharge and the wood discharge can be presented by a 3 stage model starting from 0.5 year return period, with a positive trend until bankfull discharge and then a negative trend up to the maximum flood discharge. During the falling limb of the flood hydrograph, the wood discharge is almost negligible and decreases mildly by decreasing flow discharge. Total volume of the wood on this three stage model is significantly affected by time between two floods so that by increasing the time between two floods the total volume of the wood increases. In any case, at the leading order, the wood length distribution and wood transverse distribution are identical at the same river during different floods. We also use wood fluxes as the first and easiest quantity in video monitoring to measuring wood discharge. The results first show that it is important to select an appropriate time interval to measure both wood fluxes and discharge, as they are sensitive to time for time intervals less than 1.5 h. Secondly, at leading order, power law can predict wood discharge from its fluxes. This relation is independent of flood discharge for one river. In addition, comparison between the results of two cameras, provides some knowledge about the camera positioning as well as selecting the best configuration for installing a camera on the field.

IV.1.1.2 Dynamics of single pieces of wood

In chapter III, we considered the dynamics of one single piece of wood on the field, in flume experiments and numerical models.

The field observations show that there is a transverse region on each river for which most of the wood pass. This position is independent of flood discharge but varied from one river to another.

Two experimental cases were studied, first the acceleration of a piece of wood, with and without root, at the surface of a uniform flow, and second, the wood motion in a nonuniform flow around an obstacle. We first show that the dynamic model (Eq. (III.2)) fairly reproduces the accelerated motion of floating objects. Moreover, we identify a characteristic length scale named λ, (Eq. (III.3)) which is an appropriate scaling for accelerating distance of a piece of wood from rest, so that after a distance λ the log reaches about 70% of its terminal velocity. On the field applications, this acceleration length becomes important, when it is comparable with the flow length scale. Additionally, for a floating log, regardless of its size and shape, λ was measured to be about 2 to 4 times the streamwise body length. This result is valid, provided that C_D and C_A are of order one, which is the case for wood motion in river.

In a second experiment, we considered the motion of the wood initially transported almost at the flow velocity and facing an obstacle to explore the interaction with an obstacle. As predicted from the model, we find that as soon as a piece of wood reaches the flow velocity, it behaves as a tracer, regardless of its normalized characteristic response distance $\lambda^\star$, if it remains smaller than the flow scale. In other words, as soon as the wood piece reaches the flow velocity, its motion will be accurately predicted by the kinematic model assuming the object is a flow tracer. This result is confirmed by our field observations. Comparison between wood and flow velocity on the field in both rivers shows that wood has the same velocity as flow. Considering wood piece as a tracer, we identify how the shape (*e.g.* presence of root and root length) and initial orientation of the piece of wood affect the impact process.

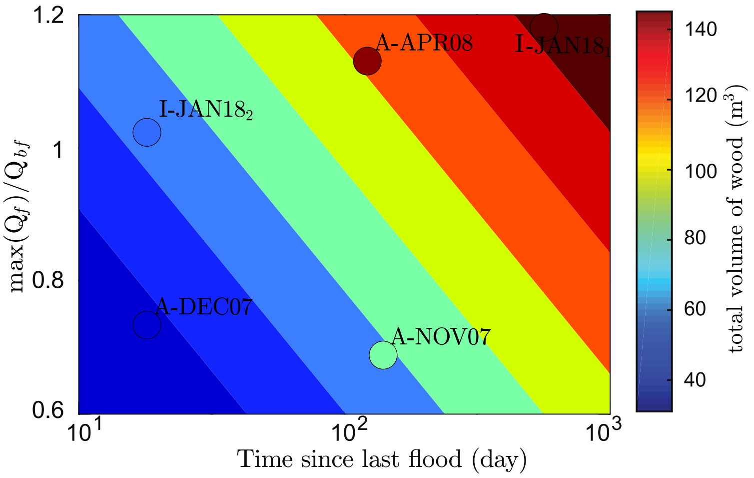

Figure IV.1: Effect of time between two floods and the flood magnitude on total wood volume.

IV.1.2 Discussion

IV.1.2.1 Concurrent effect of inter-flood time and flood magnitude on total wood volume

Here we observed that both time since the previous flood and maximum flood discharge play a role on total volume of the wood. However,using only five floods, it is not possible to find any relation between these three parameters. Figure IV.1 shows a rough estimation of the relation between flood return period, time since the last flood and volume.

The proposed relation on this figure is

$$V = 53.6 \log_{10}(\Delta t) + 110\frac{Q_f}{Q_{bf}} - 113, \tag{IV.1}$$

where V is the total volume of wood and Δt is the time since the last flood in days. For this relation based on five monitored floods $R^2 = 0.93$ and $RMSE = 20$. Table IV.1 shows the comparison between measured volume based on field data and based on Eq. IV.1. As it can be seen Eq. IV.1 can be useful to predict the total wood volume. But, it should be noted that in this equation there are uncertainties about the relation between wood length and volume. Moreover, only five floods is not enough to have an appropriate regression. Therefore, to explore the simultaneous effect of flood magnitude and time between two floods, more floods need to be monitored.

IV.1.2.2 Typical motion of individual pieces of wood in river

The motion of an individual wood in river can be described in three phases: (i) accelerated motion after recruitment (ii) wood motion along the river and (iii) facing with an obstacle. Figure IV.2 shows different phases of motion in a schematic view.

Table IV.1: Total volume estimation based on field observations and using Eq. IV.1

Flood	Volume m^3		Error	
	Field	Eq. IV.1	Absolute m^3	Relative %
I-JAN18$_1$	150	164	14	10
I-JAN18$_2$	58	66	8	14
A-NOV07	81	77	3	4
A-DEC07	31	35	3	11
A-APR08	145	123	22	15

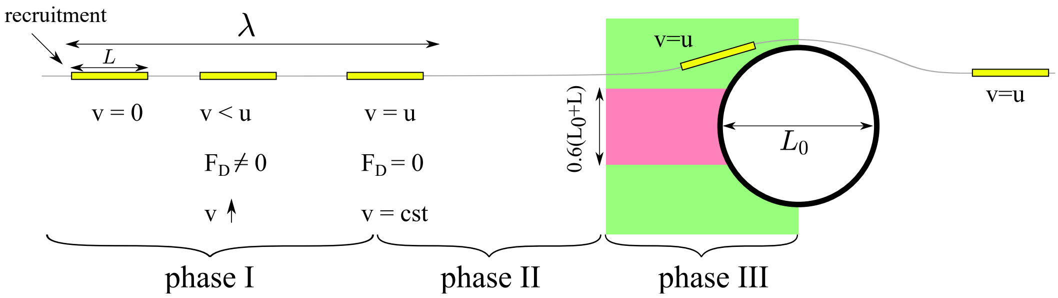

Figure IV.2: Schematic view of the motion of a piece of wood in different phases, recruitment, movement along the river and facing with an obstacle.

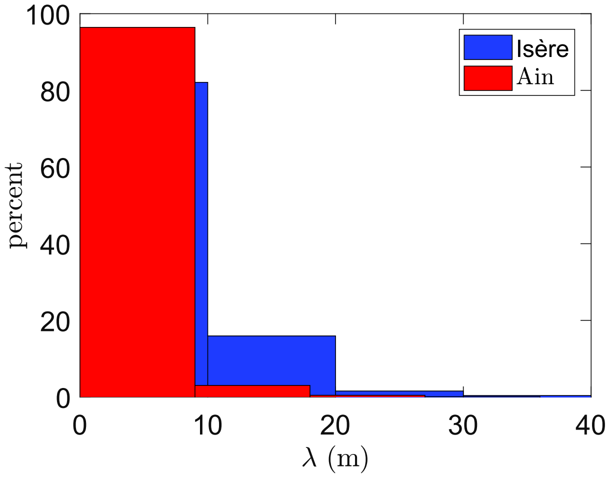

Figure IV.3: Typical distribution of λ on the Isère (blue bars) and Ain(red bars) Rivers base on wood length distribution in Fig. II.22, p. 43.

The first phase of motion normally occurs during wood recruitment in river or along very fast changes in river (*e.g.* river contraction/expansions or meandering in a short distance). Numerical analysis show that this accelerated motion is scaled by an acceleration distance scale λ (Fig. III.19, p. 81). Based on Fig. III.20, p. 82, this acceleration distance is typically about 2 times the wood streamwise length L_x, along which the wood accelerates. In addition, λ can be modified by the presence of roots so that at leading order, λ is decreased by increasing root frontal area and root pattern is a secondary factor. This observation confirms the simplification applied by Braudrick & Grant (2000) assuming a circle at the end of the logs instead of a rootwad. This simplification can be precisely useful in numerical models such as Ruiz-Villanueva *et al.* (2014*a*); Persi *et al.* (2018*a*,*b*).

As soon as wood pieces reach the flow velocity, they enter in to the second phase of motion. Both numerical and experimental analysis show that at this stage, floating wood behaves as a tracer, following the flow streamlines. To see the behavior of the wood on the field, it is necessary to compare wood and river length scales. Figure IV.3 shows the distribution of λ on the Isère River (blue bars) and Ain(red bars) based on wood length distribution of Fig. II.22, p. 43. According to Fig. III.20, p. 82, λ is assumed to be 2 times the wood length. Based on Fig. IV.2, on both rivers, λ is of the order of 10 m. On the other hand, on both rivers, the diameter of the meander at the station (as the river length scale L_0) is around 1.5 km. Therefore, the acceleration length λ compare to the river length scale L_0 is in the order of 1%. Therefore, it is expected that when in a large river (Gurnell *et al.*, 2002) a piece of wood is detected at the surface, typically it behaves like a tracer. This is in agreement with our observation so that wood has the same velocity as flow surface velocity on the Isère River Fig. III.4, p. 60 and the Ain River Fig. I.7, p. 15.

The third phase of motion presented in Fig. IV.2 is when a piece of wood approaches an instream hydraulic structure such as bridge pier or a trapping structure. The experiments show that facing with a bridge pier with same orders of length scales ($\lambda =$ O(10m), $L_0 =$ O(10m)), the wood pieces are following the streamline. However, just near the obstacle there is up to 4% of L_0 deviation from streamlines. Assuming for example a 5 m diameter bridge pier, this deviation is limited to 20 cm. Therefore, in the third phase of motion, near an obstacle, the wood is a tracer and its center of mass follows the river streamlines.

Assuming that near an obstacle the center of mass of the wood follows the streamlines results in an important consequence: for a tracer object, dynamics of the object does not play a role in impact process but its geometric conditions such as initial orientation or its shape are the governing factors in impact process. The experimental results on Fig. III.37, p. 98 show the same thing. For a floating wood when the center of mass follows the streamline its shape and orientation govern the impact process, and for a rooted log when its trunk follows the flow, larger roots increase the probability of impact. To be able to predict if a piece of wood hit the obstacle or not, in Figs. III.37 , III.38, p. 98 it is seen that the maximum distance from obstacle center line for impact is $y_c \cong 0.6(y_{max})$ which for a simple log is $y_c \cong 0.3(L_0 + L)$ on each side of the obstacle. There fore as it is seen in Fig. IV.2, the range of $0.6(L_0 + L)$ in front of the obstacle is considered as impact region presented in red color and beyond this region presented in green, no impact was detected in our experiments.

It should be noted that these results are related to a 2D surface flow with a flat bottom flume in a well controlled experimental environment. However, when it comes to the flows with many complexities like the Ain River with a bridge pier at the upstream, large sinuosity of the river and complex bathymetry, more studies are needed.

IV.1.3 Critical transverse position in a river (application to hazard assessment)

To design a bridge pier, it is necessary to know the safe transverse location for a pier in term of logjam. Similarly, to collect the wood pieces from the river using wood retention structures, it is necessary to know the transverse position in the river, where most of woods are passing. Based on our observations on the Ain and Isère Rivers, the transverse distribution of wood appears to be barely dependent of the flow discharge. As a result, we can define the critical transverse position as the region where most of the wood pieces will pass. This amount of wood enhances flow resistance and causes congested transport (Braudrick *et al.*, 1997) that is more likely to form logjams at sites of reduced transport capacity such as channel expansions or bends (Wohl, 2013). Therefore, this region is the critical location to construct a bridge pier, but it is suitable for wood trapping structures.

The fact that the position of this critical region in term of wood flow is independent of flood discharge would be important, because, at a certain point, if it is decided to construct a structure, by monitoring the river only during one flood, it is possible to determine the critical location of the river, in terms of the number of passing woods. Figure IV.4(a) is an example showing schematically the wood transverse distribution and the critical region related to wood flow as the position where 75% of the wood pieces

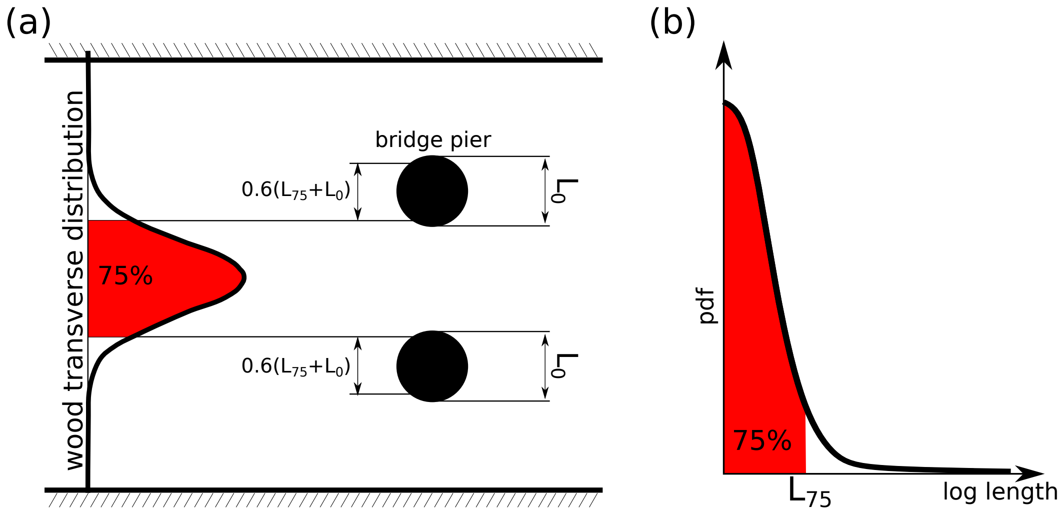

Figure IV.4: Schematic view of the hazard assessment in term of wood pieces for a bridge pier. (a) The transverse distribution of wood pieces in front of bridge piers. (b) Schematic view of length distribution of instream wood pieces.

pass. In the previous section it is seen that the critical distance for impact in front of an obstacle is $0.6(L_0 + L)$. Considering the L_{75} of the wood pieces as a characteristic length for the instream logs, the critical distance for impact will be $0.6(L_0 + L_{75})$. Therefore, for positioning a bridge pier it is important to locate it in a position where typically the instream pieces of wood do not pass in the range of $0.6(L_0 + L_{75})$ in front of the bridge pier. On the other hand, if a bridge pier is constructed at the region where high values of wood fluxes pass, there is high probability of logjam. Figure IV.5, from Google Earth service, is an example showing that in the same bridge, there is no wood on one pier and there is a logjam on the other one. This section is located on the Isère river, 6 km downstream of our study site. Beside other reasons, one reason of this asymmetry on logjam would be the position of piers and the critical region of the river.

The different skewness of the wood transverse distribution between Ain and Isère causes different transverse position of the critical section. The different skewness can be justified by river sinuosity as well as bathymetry. The sinuosity of river at the station is larger on the Ain River (1.5) than the Isère River (1.1). In addition, based on Fig. III.4, p. 60 the side slope and shallowness of river can affect the wood velocity and thus, transverse distribution of the wood.

IV.1.4 Recommendations to implement a streamside camera

The comparison between two different rivers highlights the importance on the camera positioning. Table IV.2 shows the monitoring characteristics of the two stations. Based

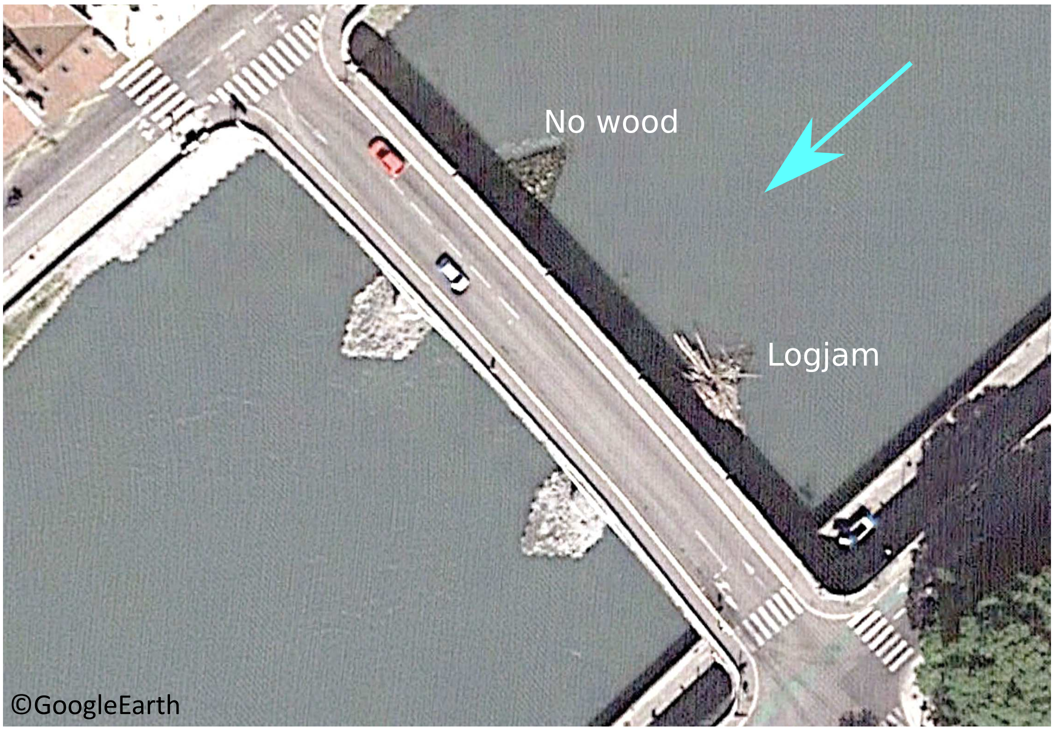

Figure IV.5: An example showing asymmetry on logjam in the same bridge. Figure is taken from Google Earth service.

Table IV.2: Monitoring characteristics of the two stations

	Elevation above	pixel size where most of the woods are detected		river	frame rate	Resolution	Focal length	View angle
	bankfull level	x-direction	y-direction	sinuosity	Hz	Pixel	mm	degree
Isère	8 m	0.02 to 0.04 m		1.1	5	600×800	3 to 9	30 to 84
Ain	9.8 m	0.1 to 0.12 m	0.3 to 0.4 m	1.5	5	600×800	2.8 - 8.5	33.3 to 92.3

on this table, the camera characteristics such as frame rate, resolution or focal length are almost the same on both rivers. The two significant differences between the two sites are river sinuosity and the distance at which most of the woods are detected (40 to 50 m from camera on the Isère River and 0 to 20 m from camera on the Ain River in Fig. III.2(a), (b), p. 58).

Two sites show different transverse wood distribution. So the position of the camera should be determined based on the information required in river. If the precision of statistics on wood is important, for example to estimate wood delivered at the outlet of a given river, the best position would be close to the main flow axis, such as the outer bend in rivers with large sinuosity. If the hazards due to wood at a specific point is the main concern, the position of camera has to be at that specific point or if there is not the required infrastructures such as internet connectivity or suitable position for installing the camera a position similar to the interested point in term of geomorphological complexity like bathymetry and sinuosity has to be selected.

Here for example comparison between Figs. III.2(a),(b), p. 58 shows that the number of detected wood in the Ain River is much higher than the Isère River, but also the pieces are smaller on the Ain River. Lassettre *et al.* (2008) observe bank retreat on the Ain River during recent decades, so that during the period 1991 to 2000; the Ain River provided a nearly greater wood volume than ten years before. This could also be due to the cross-sectional variation of pixel size (see Fig. II.18, p. 38) resulting in a bias of operator and more uncertainty in the observed parameters such as number, length or velocity far from the camera. On the Ain River maximum of wood fluxes are focused in front of the camera, which is the ideal situation to catch the wood flux (resolution here is around 5 cm/pixel). In the case of the Isère River, wood peak is located in the middle of the section (resolution here is 30 to 40 cm/pixel). Therefore, the pixel size and as a consequence the accuracy of detection on the Isère River is 5 to 10 times less than the Ain.

To describe the effect of pixel size variation, we consider a region that on both rivers the pixel size is 20 cm. Based on Fig. II.18(c), (d), p. 38 this region is around 25 to 30 m from the Isère camera and 35 to 40 m from the Ain camera. At this region the first and third quartile of wood length on the Isère are around 1.5 and 4 m respectively and on the Ain are around 1.5 and 5m. This means that in a region with the same pixel size the typical wood length is even slightly larger on the Ain River than the Isère River. Consequently, if most of the wood pieces are passing from the region with larger pixel size (like the Isère River case) the smaller objects with less diameter are not detectable, so the average length increases while the number of detected woods decreases. By contrast, when the most of wood pieces are detected in a region with small pixel size (like the Ain River case), the small objects are also detectable, so more number of woods are detected but with smaller typical length.

Elevation and transverse position of the camera are affected by river sinuosity. In a river section with sharp curvature, like what we have on the Ain, stream side camera works well. While in the case that river is almost straight and most of the wood pass through the middle of the river, if there is access to a suspended bridge (in order not to disturb the flow) middle of the bridge would be the best position, otherwise, it is recommended that at the same time the elevation of camera and its focal length increase, to decrease the oblique view to the middle of the river as possible.

The upstream infrastructures is another parameter affecting wood motion in two different ways. Firstly, the upstream controlling structures like reservoirs affect flood and wood discharge along the river. Hydrological regime of the Isère River was modified during the middle of the twentieth century by hydroelectric power plants and inter-basin transfers (Vivian, 1994; Peiry & Marnezy, 2000). While the low flows and frequent floods on the Isère River are influenced by hydroelectric infrastructure upstream the station, the floods more than 10 years return periods are much less influenced (Vivian, 1986; Vivian & Pupier, 1996; Marnezy, 1999). Therefore, both floods monitored here on the Isère River are affected by upstream infrastructures and there is a possibility that if there were not these upstream controlling structures the flood magnitude and the amount of wood fluxes varied from what we measured here. Secondly, the presence of instream structures like a bridge pier can also affect the local transverse distribution of the wood by changing the shape of flow surface streamlines. For example on the Ain, upstream the field of view there is a bridge pier that affects the flow surface patterns. If this pier was not located there, the flow structures and consequently wood trajectories would be different from what we observed here.

Frame-rate is another parameter that plays a significant role in the volume of data transformation. Videos with more frame rate, present high temporal resolution. The application of continuous frames is to monitor the wood trajectory and wood velocity components. Our observations indicate that 97% of detection cases, the presence time of the wood in the field of view has been more than 5 s. Assuming 5 Hz frame rate, the wood can be detected 25 times. The problem of small time steps is that for the woods far from the camera, there is not a detectable transformation between each time step. Due to the oblique view of camera and huge variation in size of pixels, it is difficult to suggest the optimum time step. But it is clear that at the same rate of data transmission, by decreasing number of frames for example to 1 Hz, it is possible to increase resolution of images 5 times, which is quit effective to detect objects far from the camera. Therefore, to select the model of camera, it is highly recommended to make balance between resolution and frame rate.

Additionally the oblique view of the camera can be modified potentially by “Tilt–shift photography” technique. Tilt–shift photography technique is the use of camera movements that change the orientation and/or position of the lens with respect to the film or image sensor on cameras. Tilting the camera results in perspective distortion and shifting the lens results in a picture of the entire subject without perspective distortion. However to verify the efficiency of this technique on the field doing some tests are necessary.

IV.2 Prospects

Present work provided some key scientific and technical contributions. In term of scientific contributions, by finding the relation between flood characteristics and wood discharge we tried to improve and develop the present knowledge about the link between flow and wood discharge. Moreover, our studies show that a piece of wood is accelerated in a limited length, which here is scaled by λ and then can be considered as a passive tracer. In term of technical contributions, by comparing the video monitoring technique in two different sites we provide some recommendations that are useful for practitioners for installing new monitoring stations. Several future works are worth considering to enhance the accuracy of measuring wood fluxes by videography technique and extend the application of this study.

IV.2.1 Wood accumulations upstream of obstacles

In this thesis, we studied the amount of wood pieces in a river as well as the dynamics of a single piece of wood. It is seen that firstly most of wood pieces pass from a certain cross-sectional region (Section III.1.2) with the same length distribution (Section II.3.2) and secondly there is a certain region in front of the bridge pier where the probability of impact is higher and influenced by the wood geometry (Section III.2.4.4). In addition, in the field, there is the transition from single wood pieces to multiple wood pieces and to log jams. In this context, some works are quite promising to understand the combined effect of flow, bridge and wood characteristics (Schalko, 2017; Schalko *et al.*, 2019; De Cicco *et al.*, 2015, 2016; Schmocker & Hager, 2010, 2011; Schmocker & Weitbrecht, 2013) which still constitute however a challenging question for future works.

IV.2.2 Wood sensing during night time

The most important limitation of video-monitoring approach is the visibility of wood, due to the lack of clarity, distance from the camera, weather condition, density of wood and so on. For example, in Fig. II.21 (p. 42) and Fig. II.25 (p. 47) which are dealing with, respectively, the evolution of flow discharge with wood fluxes and wood discharge, the gray regions represent the night time, when there was no light to detect the wood. It is possible to minimize the effects of these potential problems by, for example, using night vision cameras, increasing camera resolution or finding the best position for installing the camera; alternatively, some post processing techniques based on in-site information (e.g. predicting wood distribution during night based on flow discharge (II.26 p. 49)) are possible. However, to have a better vision assessment on the capabilities of this approach, more data on more rivers is needed. In any way, there will be a remaining question about the overall assessment of wood fluxes in the field during different flood patterns not available in the thesis (e.g. multi-peak floods) during the time when there is not enough visibility on the river like the gray regions in Figs. II.21 and II.25.

IV.2.3 Evaluating the accuracy of transverse length distribution

In the present work and the similar work by MacVicar & Piégay (2012) the transverse distribution of the wood length is measured by one camera at river side, and the lengths are transformed to the metric coordinates by orthorectification process. However, there is a lack of information about the wood length and frequency on other side of river due to the big size of pixels. As it is seen here, on both cases for distances more than 60 m from the camera no wood is detected. Moreover, by increasing the distance from the camera, the average wood length is increased. This can be due to the fact that far from the camera it is not possible to detect the smaller pieces resulted in increasing the average length of the wood. Therefore, there is uncertainty if it is due to the actual wood distribution or if it is a detection bias.

One suggestion to know to what extent the operator can detect the objects far from the camera is using a scale as a known object, and check its vision on camera from one side to other side of river. Also using two cameras on both sides of the river would be another solution for evaluating the operator bias based on a real flood data.

IV.2.4 Relation between wood length and volume

The direct method to calculate the wood volume is extract the wood length and mean diameter and calculate the volume, considering each piece as a single stem. To find a relation between wood length to volume, we used the same relation based on videography data on the Ain. On the Ain River it is possible to detect diameter using videography technique because, most of the woods passed near the camera and at this position the pixel size is small enough (less than 5 cm) to detect the large woods ($L > 1$ m).

Calculation the wood geometrical parameters based on videography is associated with errors. The first source of error is due to the assumption of the wood as a complete cylinder, while in some cases roots and branches are observed. The second source of error comes from the proportion of image pixel size to detectable width (diameter) of the wood, especially far from the camera, which creates significant error. In general, in the field videos, due to the very small ratio between diameter and length, measuring the diameter of the wood is much more sensitive than its length (MacVicar *et al.*, 2009). Therefore, measuring the relation between wood length and diameter/volume at some retention points like dam reservoirs can enhance the accuracy of volume measurements.

It should be noted that the detectable width of the wood is different from the wood diameter due to the buoyancy of wood. For example Ruiz-Villanueva *et al.* (2014*c*) measured the average buoyancy of the wood pieces on the Rhône/Genissiat, it is then possible to assess potentially the effect of buoyancy on the wood volume.

IV.2.5 Extend the application of the current numerical model by increasing complexity of float and flow

In this work, to show the dynamic model for simulating the motion of floating object we use a simple case of Basset-Boussinesq-Oseen equation without lateral forces. Using this equation it is possible to model the motion of symmetric objects in streamwise direction, and in potential flow. In the field, there are different complexities such as flow vorticity, and asymmetry of the wood due to its initial orientation or its shape. Therefore, in line with the approach developed in this work, it would be interesting to complete the tests on the use of the Basset-Boussinesq-Oseen equation for very large particulate Reynolds numbers, like large wood pieces in a river, and better assess trapping conditions and associated flow obstruction.

IV.2.6 Effect of secondary flows on transverse distribution of the wood

In large rivers the flow is characterized by secondary flows (Nezu *et al.*, 1993; Chauvet *et al.*, 2014). These secondary flow cells have an impact on transverse velocity fields in river. Our field observations (Figs. III.2(a), (b), p. 58) show different transverse distribution of the wood on different morphological conditions. As mentioned along the river, the floating wood pieces behave as tracers. Therefore, the surface flow due to secondary flow is one of the key factors for different transverse distributions of the wood. The effect of secondary cells can be precisely observed in meandering rivers (Blanckaert & De Vriend, 2004) what we saw on the Ain River with more skewness of the wood transverse distribution. Therefore, the 2D surface model can not simulate this condition. In order to be able to predict the transverse distribution of the wood in river, it is necessary to take into account these secondary flows, to see to what extent do these secondary flow cells impact the transverse distribution of floating wood in streams, throughout more complicate experiments or 3D simulations. A preliminary experiment, was designed in summer 2019 during the training master course of A.Delhaise.

Present work will be part of the driftwood hazard and risk assessments, for which accurate wood dynamics quantities are invaluable. The recent workshop closing the ”BoiFIMU” project was behind lively discussions about the solutions that should be favored or combined to decrease driftwood risk. Some of them propose decreasing the hazard by bank maintenance operations, making the banks poorer in wood material, or by building devoted civil engineering structures such as wood traps. Others favor decreasing the vulnerability, modifying for example the shape of the bridge decks or piers, or adopting facilities foldable in case of floods. Present field technique, by providing logs and fluxes characteristics, can contribute in evaluating the efficiency of these different solutions, to correlate fluxes with maintenance operations, etc. Knowledge concerning trajectories and collision probabilities would be useful in the design process of bridges (position, number, shape of piers) and more generally of hydraulic structures.

Bibliography

Abbe, T.B. & Montgomery, D.R. 1996 Large woody debris jams, channel hydraulics and habitat formation in large rivers. *Regulated Rivers: Research & Management* **12** (2-3), 201–221.

Ali, I., Mille, J. & Tougne, L. 2011 Wood detection and tracking in videos of rivers. In *Scandinavian Conference on Image Analysis*, pp. 646–655. Springer, Springer Berlin Heidelberg.

Ali, I., Mille, J. & Tougne, L. 2012 Space–time spectral model for object detection in dynamic textured background. *Pattern Recognition Letters* **33** (13), 1710–1716.

Ali, I., Mille, J. & Tougne, L. 2014 Adding a rigid motion model to foreground detection: application to moving object detection in rivers. *Pattern Analysis and Applications* **17** (3), 567–585.

Ali, I. & Tougne, L. 2009 Unsupervised video analysis for counting of wood in river during floods. In *International Symposium on Visual Computing*, pp. 578–587. Springer, Springer Berlin Heidelberg.

Alonso, C.V., Shields Jr, F. Douglas & Temple, DM. 2009 Dynamics of large wood: a prototype-scale flume experiment. In *Congress of International Association for Hydraulic Research Proceedings*.

Balachandar, S. & Eaton, J.K. 2010 Turbulent dispersed multiphase flow. *Annual Review of Fluid Mechanics* **42**, 111–133.

Batchelor, C.K. & Batchelor, G.K. 1967 *An introduction to fluid dynamics*. Cambridge university press.

Battin, T.J., Kaplan, L.A., Findlay, S., Hopkinson, C.S., Marti, E., Packman, A.I., Newbold, J.D. & Sabater, F. 2008 Biophysical controls on organic carbon fluxes in fluvial networks. *Nature Geoscience* **1** (2), 95.

Beebe, J.T. 2000 Flume studies of the effect of perpendicular log obstructions on flow patterns and bed topography. *The Great Lakes Geographer* **7** (1), 9–25.

Benda, L., Miller, D., Sias, J., Martin, D., Bilby, R., Veldhuisen, C. & Dunne, T. 2003 Wood recruitment processes and wood budgeting. In *American Fisheries Society Symposium*, pp. 49–74. American Fisheries Society.

Benitz, M.A., Carlson, D.W., Seyed-Aghazadeh, B., Modarres-Sadeghi, Y., Lackner, M.A. & Schmidt, D.P. 2016 CFD simulations and experimental measurements of flow past free-surface piercing, finite length cylinders with varying aspect ratios. *Computers & Fluids* **136**, 247–259.

Bergougnoux, L., Bouchet, G., Lopez, D. & Guazzelli, E. 2014 The motion of solid spherical particles falling in a cellular flow field at low Stokes number. *Physics of Fluids* **26** (9), 093302.

Bertoldi, W., Gurnell, A.M. & Welber, M. 2013 Wood recruitment and retention: The fate of eroded trees on a braided river explored using a combination of field and remotely-sensed data sources. *Geomorphology* **180**, 146–155.

Beschta, R.L. 1983 The effects of large organic debris upon channel morphology: a flume study. In *Proceedings of the DB Simons Symposium on erosion and sedimentation*, , vol. 8. Simons, Li Associates: Fort Collins, CO.

Bieri, M., Jenzer, J., Kantoush, S.A. & Boillat, J.L. 2009 Large scale particle image velocimetry applications for complex free surface flows in river and dam engineering. In *33rd IAHR 2009 Congress. Vancouver, Canada.*

Blanckaert, K. & De Vriend, H.J. 2004 Secondary flow in sharp open-channel bends. *Journal of Fluid Mechanics* **498**, 353–380.

Bocchiola, D., Rulli, M.C. & Rosso, R. 2006 Transport of large woody debris in the presence of obstacles. *Geomorphology* **76** (1-2), 166–178.

Bocchiola, D., Rulli, M.C. & Rosso, R. 2008 A flume experiment on the formation of wood jams in rivers. *Water Resources Research* **44** (2), W02408.

Boivin, M. & Buffin-Bélanger, T. 2010 Using a terrestrial LIDAR for monitoring of large woody debris jams in gravel-bed rivers. In *7th Gravel bed Rivers Conference*, pp. 5–10.

Braudrick, C.A. & Grant, G.E. 2000 When do logs move in rivers? *Water Resources Research* **36** (2), 571–583.

Braudrick, C.A. & Grant, G.E. 2001 Transport and deposition of large woody debris in streams: a flume experiment. *Geomorphology* **41** (4), 263–283.

Braudrick, C.A., Grant, G.E., Ishikawa, Y. & Ikeda, H. 1997 Dynamics of wood transport in streams: a flume experiment. *Earth Surface Processes and Landforms* **22** (7), 669–683.

Brooks, A.P. & Brierley, G.J. 2002 Mediated equilibrium: the influence of riparian vegetation and wood on the long-term evolution and behaviour of a near-Pristine river. *Earth Surface Processes and Landforms* **27** (4), 343–367.

Bush, J.W. & Eames, I. 1998 Fluid displacement by high Reynolds number bubble motion in a thin gap. *International Journal of Multiphase Flow* **24** (3), 411–430.

Carbonneau, P. & Piégay, H. 2012 *Fluvial remote sensing for science and management*. John Wiley & Sons, Ltd.

Castro, J.M. & Jackson, P.L. 2001 Bankfull discharge recurrence intervals and regional hydraulic geometry relationships: patterns in the pacific northwest, USA 1. *JAWRA Journal of the American Water Resources Association* **37** (5), 1249–1262.

Chauvet, H., Devauchelle, O., Metivier, F., Lajeunesse, E. & Limare, A. 2014 Recirculation cells in a wide channel. *Physics of Fluids* **26** (1), 016604.

Cherry, J. & Beschta, R.L. 1989 Coarse woody debris and channel morphology: a flume study 1. *JAWRA Journal of the American Water Resources Association* **25** (5), 1031–1036.

Cicco, P.N. De, Paris, E., Ruiz-Villanueva, V., Solari, L. & Stoffel, M. 2018 In-channel wood-related hazards at bridges: A review. *River Research and Applications* **34** (7), 617–628.

Comiti, F., Andreoli, A., Lenzi, M.A. & Mao, L. 2006 Spatial density and characteristics of woody debris in five mountain rivers of the Dolomites (Italian Alps). *Geomorphology* **78** (1-2), 44–63.

Comiti, F., Andreoli, A., Mao, L. & Lenzi, M.A. 2008 Wood storage in three mountain streams of the southern Andes and its hydro-morphological effects. *Earth Surface Processes and Landforms* **33** (2), 244–262.

Corrsin, S.E. & Lumley, J. 1956 On the equation of motion for a particle in turbulent fluid. *Applied Scientific Research* **6** (2), 114–116.

C.V., Alonso, F., Shields J.r. Douglas & D.M., Temple 2005 Experimental study of drag and lift forces on prototype scale models of large wood. In *Impacts of Global Climate Change*, pp. 1–11. ASCE.

De Cicco, P.N., Paris, E. & Solari, L. 2015 Flume experiments on bridge clogging by woody debris: the effect of shape of piers. In *36th IAHR World Congress, The Hague, The Netherlands, Conference Proceedings*.

De Cicco, P.N., Paris, E. & Solari, L. 2016 Wood accumulation at bridges: Laboratory experiments on the effect of pier shape. In *Proceeding of 8th River Flow Congress, Constantinescu, Garcia & Hanes (Eds.)*, pp. 2341–2345.

Dunne, T. & Leopold, L.B. 1978 *Water in environmental planning*, , vol. 44. Macmillan.

Dury, G.H., Hails, J.R. & Robbie, H.B. 1963 Bankfull discharge and the magnitude-frequency series. *Australian Journal of Science* **26**, 123–124.

Everett, R. A & Ruiz, G.M. 1993 Coarse woody debris as a refuge from predation in aquatic communities. *Oecologia* **93** (4), 475–486.

Fausch, K.D. 1993 Experimental analysis of microhabitat selection by juvenile steelhead (Oncorhynchus mykiss) and coho salmon (O. kisutch) in a British Columbia stream. *Canadian Journal of Fisheries and Aquatic Sciences* **50** (6), 1198–1207.

Fausch, K.D., Torgersen, C.E., Baxter, C.V. & Li, H.W. 2002 Landscapes to riverscapes: bridging the gap between research and conservation of stream fishes: a continuous view of the river is needed to understand how processes interacting among scales set the context for stream fishes and their habitat. *Bioscience* **52** (6), 483–498.

Fleece, W.C. 2002 Modeling the delivery of large wood to streams with light detection and ranging (LIDAR) data. *USDA Forest Service Gen. Tech. Rep. PSW-GTR-181* **2**, 71–83.

Fujita, I., Muste, M. & Kruger, A. 1998 Large-scale particle image velocimetry for flow analysis in hydraulic engineering applications. *Journal of hydraulic Research* **36** (3), 397–414.

Golladay, S.W., Battle, J.M. & Palik, B.J. 2007 Large wood debris recruitment on differing riparian landforms along a gulf coastal plain (USA) stream: a comparison of large floods and average flows. *River Research and Applications* **23** (4), 391–405.

Gonçalves, R.T., Franzini, G.R., Rosetti, Guilherme F., Meneghini, J.R. & Fujarra, A.L. 2015 Flow around circular cylinders with very low aspect ratio. *Journal of Fluids and Structures* **54**, 122–141.

Gonor, J., Sedell, J.R. & Benner, P.A. 1988 What we know about large trees in estuaries, in the sea, and on coastal beaches. *From the forest to the sea, a story of fallen trees, Maser, C., Tarrant, RF, Trappe, JM, and Franklin, JF, tech eds. USDA For. Serv. Gen. Tech. Rep. GTR-PNW-229, Pacific Northwest Res. Sta., Portland, OR* pp. 83–112.

Gregory, S., Boyer, K.L., Gurnell, A.M. & others 2003 Ecology and management of wood in world rivers. In *International Conference of Wood in World Rivers (2000: Corvallis, Or.)*, , vol. 23, pp. 663–665. American Fisheries Society.

Gschnitzer, T., Gems, B., Mazzorana, B. & Aufleger, M. 2017 Towards a robust assessment of bridge clogging processes in flood risk management. *Geomorphology* **279**, 128–140.

Gurnell, A.M. 2013 Wood in fluvial systems. *In Treatise on Geomorphology.* pp. 163–188.

Gurnell, A.M., Piegay, H., Swanson, F.J. & Gregory, S.V. 2002 Large wood and fluvial processes. *Freshwater Biology* **47** (4), 601–619.

Gurnell, A., Tockner, K., Edwards, P. & Petts, G. 2005 Effects of deposited wood on biocomplexity of river corridors. *Frontiers in Ecology and the Environment* **3** (7), 377–382.

Haga, H., Kumagai, T., Otsuki, K. & Ogawa, S. 2002 Transport and retention of coarse woody debris in mountain streams: An in situ field experiment of log transport and a field survey of coarse woody debris distribution. *Water Resources Research* **38** (8), 1–1.

Hainbucher, D., Pohlmann, T. & Backhaus, J. 1987 Transport of conservative passive tracers in the North Sea: first results of a circulation and transport model. *Continental Shelf Research* **7** (10), 1161–1179.

Hickin, E.J. 1968 Channel morphology, bankfull stage and bankfull discharge of streams near Sydney. *Australian journal of Science* **30** (7), 274–275.

Hoerner, S.F. 1965 *Fluid-dynamic drag: theoretical, experimental and statistical information.* Hoerner Fluid Dynamics.

Howe, M.S. 1995 On the force and moment on a body in an incompressible fluid, with application to rigid bodies and bubbles at high and low Reynolds numbers. *Quarterly Journal of Mechanics and Applied Mathematics* **48** (3), 401–426.

Jalonen, J. & Järvelä, J. 2013 Impact of tree scale on drag: Experiments in a towing tank. *Int. Assoc. for Hydro-Environ. Eng. and Res., Chengdu, China* pp. 8–13.

Jalonen, J. & Järvelä, J. 2014 Estimation of drag forces caused by natural woody vegetation of different scales. *Journal of Hydrodynamics, Ser. B* **26** (4), 608–623.

Jourdain, C., Belleudy, P., Tal, M. & Malavoi, J.R. 2017 Le rôle de l'hydrologie sur la destruction de la végétation dans le lit d'une rivière à galets aménagée: l'Isère en Combe de Savoie. *Géomorphologie: relief, processus, environnement* **23** (3), 203–217.

Keller, E.A. & Swanson, F.J. 1979 Effects of large organic material on channel form and fluvial processes. *Earth Surface Processes and Landforms* **4** (4), 361–380.

Kramer, N. & Wohl, E. 2014 Estimating fluvial wood discharge using time-lapse photography with varying sampling intervals. *Earth Surface Processes and Landforms* **39** (6), 844–852.

Kramer, N. & Wohl, E. 2017 Rules of the road: A qualitative and quantitative synthesis of large wood transport through drainage networks. *Geomorphology* **279**, 74–97.

LAGASSE, P.F. 2010 *Effects of debris on bridge pier scour*, , vol. 653. Transportation Research Board.

LASSETTRE, NS & KONDOLF, GM 2012 Large woody debris in urban stream channels: redefining the problem. *River research and applications* **28** (9), 1477–1487.

LASSETTRE, N.S., PIÉGAY, H., DUFOUR, S. & ROLLET, A.J. 2008 Decadal changes in distribution and frequency of wood in a free meandering river, the Ain River, France. *Earth Surface Processes and Landforms* **33** (7), 1098–1112.

LE LAY, Y.F. & MOULIN, B. 2007 Les barrages face à la problématique des bois flottants: collecte, traitement et valorisation. *La Houille Blanche* **1** (3), 96–103.

LECKIE, D.G., CLONEY, E., JAY, C. & PARADINE, D. 2005 Automated mapping of stream features with high-resolution multispectral imagery. *Photogrammetric Engineering & Remote Sensing* **71** (2), 145–155.

LEJOT, J., DELACOURT, C., PIÉGAY, H., FOURNIER, T., TRÉMÉLO, M-L. & ALLEMAND, P. 2007 Very high spatial resolution imagery for channel bathymetry and topography from an unmanned mapping controlled platform. *Earth Surface Processes and Landforms* **32** (11), 1705–1725.

LENZI, M.A. 2004 Displacement and transport of marked pebbles, cobbles and boulders during floods in a steep mountain stream. *Hydrological Processes* **18** (10), 1899–1914.

LENZI, M.A., MAO, L. & CAVALLI, M. 2011 Long term monitoring of bedload and debris flows in two small basins of different morphological settings. int. conf. debris-flow hazards mitigation: Mechanics, prediction and assessment. *Proc., Padova, Italy* **1**, 573–581.

LEOPOLD, L.B. 1994 *A View of the River*. Harvard University Press.

LYN, D.A., COOPER, T.J., YI, Y.K., SINHA, R.N. & RAO, A.R. 2003 Debris accumulation at bridge crossings: laboratory and field studies. *National Technical Information Service, Springfield, VA 22161* .

MAAS, H.G., GRÜN, A. & PAPANTONIOU, D. 1993 Particle tracking velocimetry in three-dimensional flows. *Experiments in Fluids* **15**, 133–146.

MACVICAR, B.J., PIÃ©GAY, H., HENDERSON, A., COMITI, F., OBERLIN, C. & PECORARI, E. 2009 Quantifying the temporal dynamics of wood in large rivers: field trials of wood surveying, dating, tracking, and monitoring techniques. *Earth Surface Processes and Landforms* **34** (15), 2031–2046.

MACVICAR, B.J. & PIÉGAY, H. 2012 Implementation and validation of video monitoring for wood budgeting in a wandering piedmont river, the Ain River (France). *Earth Surface Processes and Landforms* **37** (12), 1272–1289.

Magilligan, F.J., Nislow, K.H., Fisher, G.B., Wright, J., Mackey, G. & Laser, M. 2008 The geomorphic function and characteristics of large woody debris in low gradient rivers, coastal Maine, USA. *Geomorphology* **97** (3-4), 467–482.

Magnaudet, J. 1997 The forces acting on bubbles and rigid particles. In *ASME Fluids Engineering Division Summer Meeting, FEDSM*, , vol. 97, pp. 22–26.

Magnaudet, J. & Eames, I. 2000 The motion of high-Reynolds-number bubbles in inhomogeneous flows. *Annual Review of Fluid Mechanics* **32** (1), 659–708.

Malik, N., Dracos, T. & Papantoniou, D. 1993 Particle tracking in three-dimensional turbulent flows-part ii: Particle tracking. *Experiments in Fluids* **15**, 279–294.

Mandø, M. & Rosendahl, L. 2010 On the motion of non-spherical particles at high Reynolds number. *Powder Technology* **202** (1-3), 1–13.

Mandø, M., Yin, C., Sørensen, H. & Rosendahl, L. 2007 On the modelling of motion of non-spherical particles in two-phase flow. In *6th International Conference on Multiphase Flow, ICMF*, pp. 9–13.

Mansui, J., Molcard, A. & Ourmieres, Y. 2015 Modelling the transport and accumulation of floating marine debris in the Mediterranean basin. *Marine Pollution Bulletin* **91** (1), 249–257.

Marcus, A., Legleiter, C., Aspinall, R., Boardman, J. & Crabtree, R. 2003 High spatial resolution hyperspectral mapping of in-stream habitats, depths, and woody debris in mountain streams. *Geomorphology* **55** (1-4), 363–380.

Marcus, A., Marston, R., C., Colvard & Gray, R. 2002 Mapping the spatial and temporal distributions of woody debris in streams of the Greater Yellowstone Ecosystem, USA. *Geomorphology* **44** (3-4), 323–335.

Marnezy, A. 1999 L'Arc et sa vallée: anthropisation et géodynamique d'une rivière Alpine dans son bassin versant. PhD thesis, Grenoble 1.

Maxey, M.R. & Riley, J. 1983 Equation of motion for a small rigid sphere in a nonuniform flow. *Physics of Fluids* **26** (4), 883–889.

May, C.L. & Gresswell, R.E. 2003 Large wood recruitment and redistribution in headwater streams in the southern Oregon Coast Range, USA. *Canadian Journal of Forest Research* **33** (8), 1352–1362.

Meselhe, E.A., Peeva, T. & Muste, M. 2004 Large scale particle image velocimetry for low velocity and shallow water flows. *Journal of Hydraulic Engineering* **130** (9), 937–940.

Meyer, V.R. 2007 Measurement uncertainty. *Journal of Chromatography A* **1158** (1-2), 15–24.

Mikhail, E. & Ackermann, F. 1976 Observations and least squares. *IEP-A Dun-Donnelley, New York* .

Montgomery, D.R., Collins, B.D., Buffington, J.M. & Abbe, T.B. 2003 Geomorphic effects of wood in rivers. In *American Fisheries Society Symposium*, , vol. 37, pp. 21–47.

Moulin, B. & Piegay, H. 2004 Characteristics and temporal variability of large woody debris trapped in a reservoir on the River Rhone: implications for river basin management. *River Research and Applications* **20** (1), 79–97.

Muste, M., Fujita, I. & Hauet, A. 2008 Large-scale particle image velocimetry for measurements in riverine environments. *Water Resources Research* **44** (4).

Naiman, R.J., Bilby, R.E., Schindler, D.E. & Helfield, J.M. 2002 Pacific salmon, nutrients, and the dynamics of freshwater and riparian ecosystems. *Ecosystems* **5** (4), 399–417.

Nanson, G.C., Barbetti, M. & Taylor, G. 1995 River stabilisation due to changing climate and vegetation during the late quaternary in western Tasmania, Australia. *Geomorphology* **13** (1-4), 145–158.

Nezu, I., Tominaga, A. & Nakagawa, H. 1993 Field measurements of secondary currents in straight rivers. *Journal of Hydraulic Engineering* **119** (5), 598–614.

Niklas, K. 1995 Size-dependent allometry of tree height, diameter and trunk-taper. *Annals of Botany* **75** (3), 217–227.

Oswald, E.B. & Wohl, E. 2008 Wood-mediated geomorphic effects of a Jökulhlaup in the Wind River Mountains, Wyoming. *Geomorphology* **100** (3-4), 549–562.

Peiry, J.L. & Marnezy, A. 2000 Les barrages et réservoirs hydroélectriques des Alpes Françaises et leurs impacts sur les cours d'eau. *Les régions françaises face aux extrêmes hydrologiques* pp. 191–209.

Persi, E., Petaccia, G. & Sibilla, S. 2018*a* Large wood transport modelling by a coupled Eulerian–Lagrangian approach. *Nat. Hazards* **91** (1), 59–74.

Persi, E., Petaccia, G., Sibilla, S., Brufau, P. & García-Navarro, P. 2018*b* Calibration of a dynamic Eulerian-Lagrangian model for the computation of wood cylinders transport in shallow water flow. *Journal of Hydroinformatics* **21** (1), 164–179.

Pickett, S.T. & White, P.S. 1985 Natural disturbance and patch dynamics.

Piégay, H., Moulin, B. & Hupp, Cliff R. 2017 Assessment of transfer patterns and origins of in-channel wood in large rivers using repeated field surveys and wood characterisation (the Isère River upstream of Pontcharra, France). *Geomorphology* **279**, 27–43.

Piton, G. & Recking, A. 2015 Design of sediment traps with open check dams. I: Hydraulic and deposition processes. *Journal of Hydraulic Engineering* **142** (2), 04015045.

P.W., Nicholas, V.A., Carlos, J.B., Sean & R.T., Colin 2001 Distorted Froude-scaled flume analysis of large woody debris. *Earth Surface Processes and Landforms* **26** (12), 1265–1283.

R.A., Ted, Schweiger, E.W., Bolgrien, D.W., Ismert, P. & Selle, T. 2004 Bank stabilization, riparian land use and the distribution of large woody debris in a regulated reach of the upper Missouri River, North Dakota, USA. *River Research and Applications* **20** (7), 829–846.

Ravazzolo, D., Mao, L., Garniga, B., Picco, L. & Lenzi, M. 2013 Displacement length and velocity of tagged logs in the Tagliamento River. *Journal of Agricultural Engineering* .

Rickenmann, D. 2012 Alluvial steep channels: Flow resistance, bedload transport prediction, and transition to debris flows. *Gravel-Bed Rivers: Processes, Tools, Environments* pp. 386–397.

Rickenmann, D. & Zimmermann, M. 1993 The 1987 debris flows in Switzerland: documentation and analysis. *Geomorphology* **8** (2-3), 175–189.

Rickli, C., Badoux, A., Rickenmann, D., Steeb, N. & Waldner, P. 2018 Large wood potential, piece characteristics, and flood effects in Swiss mountain streams. *Physical Geography* **39** (6), 542–564.

Ruiz-Villanueva, V., Bladé, E., Sánchez-Juny, M., Marti-Cardona, B., Díez-Herrero, A. & Bodoque, J. 2014*a* Two-dimensional numerical modeling of wood transport. *Journal of Hydroinformatics* **16** (5), 1077–1096.

Ruiz-Villanueva, V, Bodoque, JM, Díez-Herrero, A & Bladé, E 2014*b* Large wood transport as significant influence on flood risk in a mountain village. *Natural hazards* **74** (2), 967–987.

Ruiz-Villanueva, V., Bodoque, J.M., Díez-Herrero, A., Eguibar, M.A. & Pardo-Igúzquiza, E. 2013 Reconstruction of a flash flood with large wood transport and its influence on hazard patterns in an ungauged mountain basin. *Hydrological Processes* **27** (24), 3424–3437.

Ruiz-Villanueva, V., Mazzorana, B., Bladé, E., Bürkli, L., Iribarren-Anacona, P., Mao, L., Nakamura, F., Ravazzolo, D., Rickenmann, D., Sanz-Ramos, M., Stoffel, M. & Wohl, E. 2019 Characterization of wood-laden flows in rivers. *Earth Surface Processes and Landforms* **44** (9), 1694–1709.

Ruiz-Villanueva, V., Stoffel, M., Piégay, H., Gaertner, V. & Perret, F. 2014*c* Wood density assessment to improve understanding of large wood buoyancy in rivers. *River Flow 2014–Schleiss et Al.(Eds)* pp. 2503–2508.

Ruiz-Villanueva, V., Wyżga, B., Zawiejska, J., Hajdukiewicz, M. & Stoffel, M. 2016 Factors controlling large-wood transport in a mountain river. *Geomorphology* **272**, 21–31.

Schalko, Isabella 2017 Large wood accumulation probability at a single bridge pier. In *Proceedings of the 37th IAHR world congress*, pp. 1704–1713. IAHR.

Schalko, Isabella, Lageder, Carmen, Schmocker, Lukas, Weitbrecht, Volker & Boes, Robert M 2019 Laboratory flume experiments on the formation of spanwise large wood accumulations part i: Effect on backwater rise. *Water Resources Research* .

Schmocker, L. & Hager, W.H. 2010 Drift accumulation at river bridges. In *River flow*. Bundesanstalt für Wasserbau Karlsruhe.

Schmocker, L. & Hager, W. 2011 Probability of drift blockage at bridge decks. *Journal of Hydraulic Engineering* **137** (4), 470–479.

Schmocker, L. & Weitbrecht, V. 2013 Driftwood: Risk analysis and engineering measures. *Journal of Hydraulic Engineering* **139** (7), 683–695.

Scott, D.N. & Wohl, E. 2018 Natural and anthropogenic controls on wood loads in river corridors of the Rocky, Cascade, and Olympic Mountains, USA. *Water Resources Research* **54** (10), 7893–7909.

Seo, J.I., Nakamura, F., Nakano, D., Ichiyanagi, H. & Chun, K.W. 2008 Factors controlling the fluvial export of large woody debris, and its contribution to organic carbon budgets at watershed scales. *Water Resources Research* **44** (4).

Serlet, A. 2018 Biomorphodynamics of river bars in channelized, hydropower-regulated rivers. PhD thesis, University of Trento.

Serlet, A.J., Gurnell, A.M., Zolezzi, G., Wharton, G., Belleudy, P. & Jourdain, C. 2018 Biomorphodynamics of alternate bars in a channelized, regulated river: An integrated historical and modelling analysis. *Earth Surface Processes and Landforms* **43** (9), 1739–1756.

Singh, P. & Joseph, D. 2005 Fluid dynamics of floating particles. *Journal of Fluid Mechanics* **530**, 31–80.

Skalak, K. & Pizzuto, J. 2010 The distribution and residence time of suspended sediment stored within the channel margins of a gravel-bed bedrock river. *Earth Surface Processes and Landforms* **35** (4), 435–446.

Toschi, F. & Bodenschatz, E. 2009 Lagrangian properties of particles in turbulence. *Annual Review of Fluid Mechanics* **41** (1), 375–404.

TUROWSKI, J.M., BADOUX, A., BUNTE, K., RICKLI, C., FEDERSPIEL, N. & JOCHNER, M. 2013 The mass distribution of coarse particulate organic matter exported from an Alpine headwater stream. *Earth Surface Dynamics* **1** (1), 1–11.

VIVIAN, H. 1986 Un exemple de régime influencé: hydrologie et hydroélectricité dans les cours d'eau des Alpes du Nord. *Food and agriculture organization of the united nations* .

VIVIAN, H. 1994 L'hydrologie artificialisée de l'Isère en amont de Grenoble. Essai de quantification des impacts des aménagements. *Revue de Géographie Alpine* **82** (2), 97–112.

VIVIAN, H. & PUPIER, N. 1996 Crues et aménagements hydroélectriques. l'exemple des crues de l'Isère et du Drac à Grenoble. *Hommes et terres du Nord* **1** (1), 13–19.

VOTH, G.A. & SOLDATI, A. 2017 Anisotropic particles in turbulence. *Annual Review of Fluid Mechanics* **49**, 249–276.

VÄSTILÄ, K. & JÄRVELÄ, J. 2014 Modeling the flow resistance of woody vegetation using physically based properties of the foliage and stem. *Water Resources Research* **50** (1), 229–245.

WALLERSTEIN, N.P., ALONSO, C.V., BENNETT, S.J. & THORNE, C.R. 2002 Surface wave forces acting on submerged logs. *Journal of hydraulic engineering* **128** (3), 349–353.

WARREN, D. & KRAFT, C. 2008 Dynamics of large wood in an eastern US mountain stream. *Forest Ecology and Management* **256** (4), 808–814.

WEBB, A. & ERSKINE, W.D. 2003 Distribution, recruitment, and geomorphic significance of large woody debris in an alluvial forest stream: Tonghi Creek, southeastern Australia. *Geomorphology* **51** (1-3), 109–126.

WILCOX, A.C. & WOHL, E. 2006 Flow resistance dynamics in step-pool stream channels: 1. Large woody debris and controls on total resistance. *Water Resources Research* **42** (5).

WILLIAMS, G.P. 1978 Bank-full discharge of rivers. *Water Resources Research* **14** (6), 1141–1154.

WOHL, E. 2011 Seeing the forest and the trees: Wood in stream restoration in the Colorado Front Range, United States. *Stream Restoration in Dynamic Fluvial Systems: Scientific Approaches, Analyses, and Tools* **194**, 399–418.

WOHL, E. 2013 Floodplains and wood. *Earth-Science Reviews* **123**, 194–212.

WOHL, E. & AG, SPRINGER INTERNATIONAL PUBLISHING 2018 *Sustaining river ecosystems and water resources*. Springer.

Wohl, E., Bledsoe, B.P., Fausch, K.D., Kramer, N., Bestgen, K.R. & Gooseff, M.N. 2016 Management of large wood in streams: an overview and proposed framework for hazard evaluation. *JAWRA Journal of the American Water Resources Association* **52** (2), 315–335.

Wohl, E., Cenderelli, D.A., Dwire, K.A., Ryan-Burkett, S.E., Young, M.K. & Fausch, K.D. 2010 Large in-stream wood studies: a call for common metrics. *Earth Surface Processes and Landforms* **35** (5), n/a–n/a.

Wohl, E., D.C., Pfeiffer, A., Jackson, K. & Laurel, D.A. 2018 Distribution of large wood within river corridors in relation to flow regime in the semiarid western US. *Water Resources Research* **54** (3), 1890–1904.

Wohl, E., Kramer, N., Ruiz-Villanueva, V., Scott, D.N., Comiti, F., Gurnell, A.M., Piegay, H., Lininger, K.B., Jaeger, K.L., Walters, D.M. & others 2019 The natural wood regime in rivers. *Bioscience* .

Wohl, E. & Scott, D.N. 2017 Wood and sediment storage and dynamics in river corridors. *Earth Surface Processes and Landforms* **42** (1), 5–23.

Yin, C., Rosendahl, L., Kær, S.K. & Sørensen, H. 2003 Modelling the motion of cylindrical particles in a nonuniform flow. *Chemical Engineering Science* **58** (15), 3489–3498.

Young, W.J. & Davies, T.R. 1991 Bedload transport processes in a braided gravel-bed river model. *Earth Surface Processes and Landforms* **16** (6), 499–511.

FOLIO ADMINISTRATIF

THESE DE L'UNIVERSITE DE LYON OPEREE AU SEIN DE L'INSA LYON

NOM :
GHAFFARIAN ROOHPARVAR

DATE de SOUTENANCE : 15/11/2019

Prénoms :
Hossein

TITRE :
Study of driftwood dynamics in rivers for hazard assessment

NATURE :
Doctorat

Numéro d'ordre : 2019LYSEI094

Ecole doctorale :
Mécanique, Énergétique, Génie civil et Acoustique

Spécialité :
Mécanique des fluides

RESUME :

Driftwood is an integral part of river corridors where it plays an important role both in river ecology and morphology. During the last decades, the amount of large wood transported in some of the European rivers has increased, notably due to modifications in the human pressure and management of riparian forest buffers along rivers. This causes an increase of potential hazards for hydraulic structures and urban areas. In this context, the aim of this thesis is to study the driftwood dynamics in rivers in order to provide elements for hazard assessment. This is carried out in two ways: (i) using in-situ streamside videography to measure the amount of wood transported by the river during floods and (ii) analyzing the dynamics of individual pieces of wood both on the field and in a well-controlled experimental environment combined with theoretical models. The present work provides several scientific and technical contributions. First by studying the link between wood discharge and flood characteristics, such as flood magnitude, hydrograph and inter-flood time, we consolidate and extend the present knowledge about the link between flow and wood discharges. Second, our studies show that when a piece of wood is recruited into the river, it is accelerated on a limited distance, which scales as the wood length in the flow direction. Once the wood piece reaches the flow velocity, it behaves as a flow tracer. In terms of technical contributions, by comparing the video monitoring technique in two different sites, we provide some recommendations that are useful for practitioners for installing new monitoring stations. This work will be part of the driftwood hazard and risk assessments, for which accurate wood dynamics quantities are required.

MOTS-CLÉS :

Driftwood, Hazard, Wood fluxes, Wood discharge, Field, Experiments, Advection equation.

Laboratoire (s) de recherche :
LMFA – Laboratoire de Mécanique des Fluides et d'Acoustique. UMR 5509
EVS – Environnement Ville Société. UMR 5600

Directeur de thèse :
Diego LOPEZ, Nicolas RIVIERE, Hervé PIEGAY

Président de jury :

Composition du jury :
Mario Aristide LENZI (Rapporteur), Dieter RICKENMANN (Rapporteur), Laurence BERGOUGNOUX, Laurence DUCHESNE, Jean-Philippe MATAS.